REPORT DOCUMENTATION PAGE

AFRL-SR-BL-TR-01-

$\mathcal{O}\mathcal{O}\,\mathcal{C}\mathcal{O}\,\mathcal{S}$

Public reporting burden for this collection of information is estimated to average 1 hour per response, includi— ces,
gathering and maintaining the data needed, and completing and reviewing the collection of information. Sen this
collection of information, including suggestions for reducing this burden, to Washington Headquarters Servic rson
Davis Highway, Suite 1204, Arlington, VA 22202-4302, and to the Office of Management and Budget, Pape

1. AGENCY USE ONLY *(Leave blank)*	2. REPORT DATE	3. REPO...
		01 Apr to 30 Nov 98 Final

4. TITLE AND SUBTITLE	5. FUNDING NUMBERS
Nonlinear Optoelectronic Integrated Circuits	61102F 2301/AS

6. AUTHOR(S)

Dr. Fetterman

7. PERFORMING ORGANIZATION NAME(S) AND ADDRESS(ES)	8. PERFORMING ORGANIZATION REPORT NUMBER
University of California, Los Angeles 1400 Uberroth Bldg. Box 951406 Los Angeles, CA 90095-1406	

9. SPONSORING/MONITORING AGENCY NAME(S) AND ADDRESS(ES)	10. SPONSORING/MONITORING AGENCY REPORT NUMBER
AFOSR/NE 801 North Randolph Street, Rm 732 Arlington, VA 22203-1977	F49620-96-1-0096

11. SUPPLEMENTARY NOTES

12a. DISTRIBUTION AVAILABILITY STATEMENT	12b. DISTRIBUTION CODE
Unlimited Distribution	

AIR FORCE OFFICE OF SCIENTIFIC RESEARCH (AFOSR)
NOTICE OF TRANSMITTAL DTIC. THIS TECHNICAL REPORT
HAS BEEN REVIEWED AND IS APPROVED FOR PUBLIC RELEASE
LAW AFR 190-12. DISTRIBUTION IS UNLIMITED.

13. ABSTRACT *(Maximum 200 words)*

This program investigated the development of enabling technologies for optoelectronic integration and novel nonlinear concepts using these elements. As part of this effort we used optical mixing techniques to demonstrate optical modulators working above 100 GHz. Phototransistors were fabricated and tested at 60 GHz at high optical powers. Passive devices such as fiber gratings were tested and used as nonlinear transmission elements.

14. SUBJECT TERMS		15. NUMBER OF PAGES
		16. PRICE CODE

17. SECURITY CLASSIFICATION OF REPORT	18. SECURITY CLASSIFICATION OF THIS PAGE	19. SECURITY CLASSIFICATION OF ABSTRACT	20. LIMITATION OF ABSTRACT
UNCLASSIFIED	UNCLASSIFIED	UNCLASSIFIED	UL

20010221 116

Standard Form 298 (Rev. 2-89) (EG)
Prescribed by ANSI Std. 239.18
Designed using Perform Pro, WHS/DIOR, Oct 94

ELECTRICAL ENGINEERING DEPARTMENT
THE HENRY SAMUELI SCHOOL OF ENGINEERING
AND APPLIED SCIENCE
BOX 951594
LOS ANGELES, CALIFORNIA 90095-1594

Jan. 2, 2001

Dr. Howard Schlossberg
Air Force Office of Scientific Research
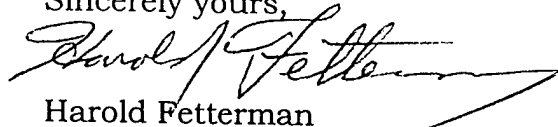801 North Randolph Street, Room 732
Arlington VA 22203-1977

Dear Dr. Schlossberg:

I enclose a copy of the Final Technical report for the grant "Nonlinear Optoelectronic Integrated Systems" # F49620-96 – 1 -0096. The papers, which represented the major part of the report, have been updated to the actual published versions rather than the preprints that were originally included. The grant was a major factor in helping us to make new types of systems. These ranged from Integrated Polymer Modulators at millimeter wave frequencies and optically controlled phased array radars, to optically controlled microwave phase conjugation surfaces.

Other concepts and devices were also explored in this grant including MEMs based non linear arrays, high power phototransistors and ELO optical mixers. Many of the devices conceived during this effort are being actively investigated today and are beginning to be used commercially.

I thank you again for your support and guidance in this program.

Sincerely yours,

Harold Fetterman

20010221 116

Nonlinear Optoelectronic Integrated Systems

F49620-96 – 1 –0096

Harold Fetterman, UCLA

This program investigated the development of enabling technologies for optoelectronic integration and novel nonlinear concepts using these elements. As part of this effort we used optical mixing techniques to demonstrate optical modulators working above 100 GHz. Phototransistors were fabricated and tested at 60 GHz at high optical powers. Passive devices such as fiber gratings were tested and used as nonlinear transmission elements.

Perhaps the most interesting part of this effort involved the use of optically coupled mixers to be used in phase conjugation systems. This concept is now actively being studied for communications networks. In addition serially fed optically controlled radars were conceived and developed. The hardest part of such a system is the receive and this was also demonstrated.

Other concepts which were studied as part of this overall program involved the use of ELO HEMTs for optical detectors and mixers. This work was limited to 140 GHz because of the available devices. Later the actually optical mixing was extended to 211 GHz. This was a record at the time and has just recently been broken by our group.

Finally, other experimental devices which were investigated, as part of our integrated effort, involved the use of Femto second lasers. The bandwidth of the lasers were vital to examining fiber optic gratings in transmission and ,more recently, the implementation of time stretching for high speed A to D.

Papers are attached which document all of these efforts and the major results.

Harold Fetterman

High-Frequency Polymer Modulators with Integrated Finline Transitions and Low V_π

Datong Chen, Daipayan Bhattacharya, Anand Udupa, Boris Tsap, Harold R. Fetterman, *Fellow, IEEE,*
Antao Chen, Sang-Shin Lee, Jinghong Chen, William H. Steier, *Fellow, IEEE,* and Larry R. Dalton

Abstract— Ultrahigh-speed integrated electrooptic polymer phase modulators have been fabricated and tested. They are made from a new nonlinear optical polymer, amino phenylene isophorone isoxazolone (APII), and are incorporated with integrated high-speed electrode transitions for W-band (75–110 GHz) operation. This new polymer has also been used to fabricate Mach–Zehnder modulators. These devices show good performance over a wide frequency band ranging to 40 GHz and have a $V\pi < 10$ V. The measurements establish APII, and other chromophores specially designed to minimize chromophore–chromophore interaction, as strong contenders for fabricating modulators for commercial and military applications.

Index Terms—Electrooptic modulation, finline transition, optical mixing, optical waveguides, traveling-wave devices.

NONLINEAR optical polymer materials have become a viable option for future high-performance integrated optics. This is especially true for high-frequency optical circuits because of their high nonlinearity, fast electronic response and near ideal velocity match for traveling-wave devices. Recent progress in research on nonlinear optical polymer materials and devices made from them confirm these predictions [1]–[4].

Previously, we demonstrated the operation of polymer traveling-wave phase modulators up to 110 GHz [5]. In those experiments, we used commercial coplanar waveguide probes (Picoprobe Model 120) to launch the driving power into the modulators. Though these probes provided excellent coupling of the power up to 120 GHz, they are unsuitable for integrated modulator structures due to their cost, size, and geometry. In this paper, we present the design and fabrication of a set of devices with monolithically integrated antipodal finline transitions, the structure of which is shown in Fig. 1. It has the advantage of low loss and high-dimensional fabrication tolerance. The transition gradually transforms the electric field
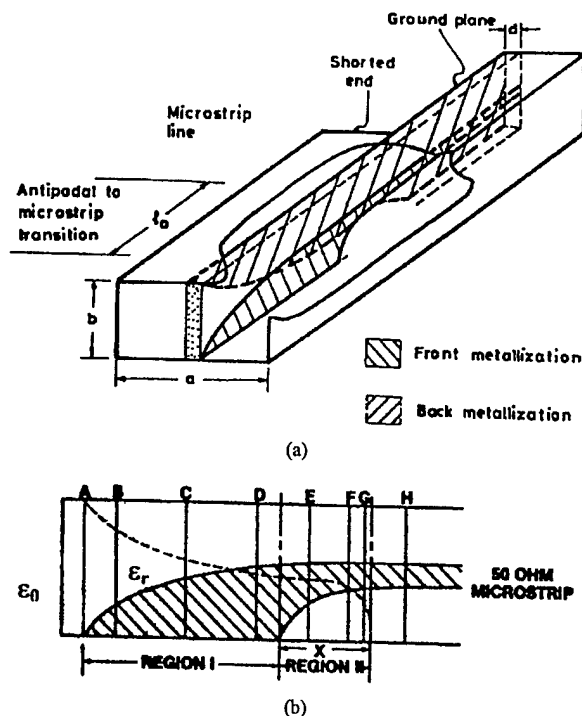
Fig. 1. (a) Design of the finline transition. (b) The changing overlap between the top and bottom electrodes gradually rotates the electric field by 90°.

profile of the rectangular metallic waveguide to that of the microstrip line electrode on the device and effectively couples the microwave driving power into the modulator.

We chose to use a 127-μm-thick Mylar film as the dielectric substrate owing to its low microwave loss tangent; good electrical, chemical, thermal and mechanical properties. The Mylar film was glued onto a silicon wafer for mechanical support during processing and detached from it just before insertion into the waveguide. A layer of silver and gold was deposited on the Mylar to serve as the lower ground plane for the microstrip lines.

Using photolithography, the lower finline transition pattern was etched in the region to be inserted into the waveguide. The lower cladding layer and the active polymer layer were spin coated and the active polymer was corona poled. The optical waveguide pattern was defined on the polymer using reactive ion etching with alignment to the pre-etched ground pattern. The upper cladding was spun on and a thin layer of chromium and gold was deposited for the top electrode.

(a)

(b)

Fig. 2. (a) Photograph of the fabricated polymer modulator with integrated finline transitions at both ends of the traveling-wave electrode. (b) Photograph of the packaged W-band polymer modulator. This shows one modulator in the array connected to the rectangular waveguide.

A thick photoresist was patterned to define the top electrode and the upper finline transition. This pattern was precisely aligned to the polymer optical waveguide and the lower finline. Electrochemical gold plating was used to increase the thickness of the top electrode to 7 μm. The end surfaces of the optical waveguide were prepared using a dicing saw. A photograph of the fabricated device is shown in Fig. 2(a). The particular finline transition region to be inserted into the rectangular waveguide was separated from the array and the polymer layers on the lower finline transition pattern removed using a solvent. The transition was then inserted into the waveguide as shown in Fig. 2(b).

Previously, we have made polymer modulator devices using PUR-DR 19 that had an electrooptic coefficient $r_{33} = 15$ pm/V, about half that of LiNbO$_3$. Recent efforts in nonlinear organic chemistry have resulted in the synthesis of polymers with electrooptic coefficients close to or even exceeding that of LiNbO$_3$. This is a direct consequence arising out of a better understanding of the London forces governing the dipole–dipole electrostatic interactions [6]. One such polymer developed by Dalton et al. is amino phenylene isophorone isoxazolone (APII) which has a $r_{33} = 30$ pm/V at an optical wavelength of 1.06 μm [1]. In addition to impressive nonlinearities, APII has exhibited low optical losses and high stability. Fig. 3 shows the
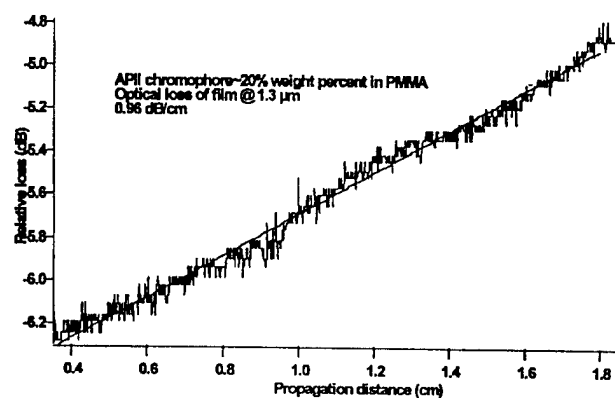

Fig. 3. Optical loss of the APII as a function of the propagating distance. Note that losses typically increase after crosslinking.

intrinsic optical loss ($\sim$1 dB/cm) of the APII as a function of the propagating distance of light. The temporal stability of the induced acentric dipole alignment is achieved by incorporating chromophores into a crosslinked polyurethane thermosetting network. This increases the optical losses slightly, but makes these systems very robust. We have used them with relatively high-power levels ($>$20 mW) for long periods of time. APII exhibits high thermal stability, the decomposition temperature being 235 °C. Alignment temporal stability ranges from 90 °C to 120 °C for a crosslinked polymer network.

The performance of these APII polymer devices was measured using an optical heterodyne technique [7]. This technique involves mixing of the modulated output of our device and the output of a tunable laser that is set at a fixed frequency away from the center frequency of the modulated laser beam. A generalized schematic of this measurement is shown in Fig. 4(a). Assuming small-signal case, one of the terms generated by the beating between the three arms has a frequency $\Delta f = f - (F_1 - F_2)$ and has the following form:

$$E_1 E_3 \cdot \frac{\pi V_m}{V_\pi} \cdot \sin[2\pi \cdot \Delta f \cdot t - \Delta \phi] \qquad (1)$$

where E_1 and E_3 are electric field strengths in the first and third arm, respectively, V_m and f are the peak voltage and frequency of the microwave signal, $F_1 - F_2$ and $\Delta \phi = \phi_1 - \phi_3$ are the difference in frequency and static phase between the two lasers and V_π is the half-wave voltage of the phase modulator. By tuning the two lasers, Δf can be made to fall in the IF band of our detection setup. The magnitude of the photocurrent generated by the detector is inversely proportional to the V_π of the modulator at the frequency of operation. Since it depends only on the interaction between the phase-modulated arm and the heterodyne arm, this technique can be used equivalently to measure the frequency performance of phase and Mach–Zehnder modulators.

Light from a diode-pumped Nd:YAG laser ($\lambda = 1310$ nm) was butt-coupled to the optical waveguide endface of our modulator using a single-mode PM fiber. Light for the local oscillator was derived from an external-cavity semiconductor diode laser, which could be tuned several hundreds of gigahertz around the Nd:YAG laser. Fine tuning of the difference frequency was achieved by precisely adjusting the frequency
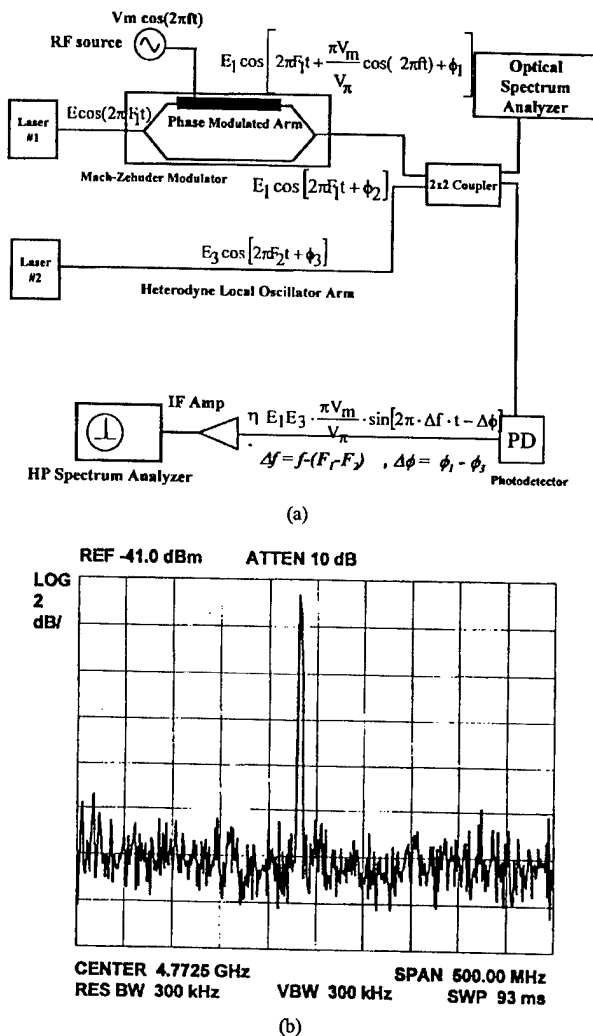
(a)

(b)

Fig. 4. (a) Generalized schematic of the optical heterodyne setup showing the Mach–Zehnder structure and local oscillator configuration. (b) Modulation signal of the APII phase modulator at 95 GHz down-converted to an IF of 4.77 GHz.

optical heterodyne measurement of the modulation signal. The initial measurements on the modulator showed considerable rolloff over the 0–40-GHz band of operation resulting from losses in the microstrip line. As we have found in related polymer structures, the V_π can be made almost flat over this frequency range by increasing the thickness of the microstrip line.

Traditionally, it has been accepted that the main advantage of polymer modulators over LiNbO$_3$ modulators is their ultrahigh-theoretical bandwidth. This results from the polymers' almost perfect velocity match that allows them to be configured as traveling-wave devices [8]. However, the problem of the limited nonlinearities in polymer materials has so far kept them from finding widespread use. This new generation of polymer devices have shown vast improvement in performance over DR19 [9] and can compete with LiNbO$_3$ devices in many important applications.

In conclusion, APII, a new polymer material with high nonlinearity and low optical loss has been synthesized and used to fabricate arrays of ultrahigh-frequency phase modulators with integrated finline transitions. These modulators have been tested at 95 GHz. The excellent microwave performance of the integrated transition signals the first successful efforts in packaging of polymer modulators at such high frequencies. Using this new polymer, Mach–Zehnder modulators have been fabricated and shown to work over a wide frequency band. Both these devices have shown very low V_π and have the ability to be commercially fabricated and packaged. Hence, these devices have widespread potential applications in commercial communication and military systems.

REFERENCES

[1] J. Chen, J. Zhu, A. Harper, F. Wang, M. He, S. Mao, and L. R. Dalton, "Synthesis and characterization of a high-$\mu\beta$ chromophore containing the isophorone moiety for electro-optic applications," *Polymer Preprints*, vol. 38, no. 2, pp. 215–216, 1997.

[2] K. W. Beeson, P. M. Ferm, K. A. Horn, C. W. Knapp, M. J. McFarland, A. Nahata, J. Shan, C. Wu, and J. T. Yardley, "Polymeric electro-optic materials and devices: Meeting the challenges of practical applications," *Nonlinear Optical Properties of Organic Materials VI, Proc. SPIE*, 1993, vol. 2025, pp. 488–498.

[3] *Polymers for Second-Order Nonlinear Optics*, G. A. Lindsay and K. D. Singer, Eds. Washington DC: Amer. Chem. Soc., 1994.

[4] Y. Shi, W. H. Steier, L. Yu, M. Chen, and L. R. Dalton, "Large stable photoinduced refractive index change in a nonlinear optical polyester polymer with disperse red side groups," *Appl. Phys. Lett.*, vol. 58, no. 11, pp. 1131–1133, Mar. 1991.

[5] D. Chen, H. R. Fetterman, A. Chen, W. H. Steier, L. R. Dalton, W. Wang, and Y. Shi, "Demonstration of 110 GHz electro-optic polymer modulators," *Appl. Phys. Lett.*, vol. 70, no. 25, pp. 3335–3337, June 1997.

[6] L. R. Dalton, A. W. Harper, and B. H. Robinson, "The role of London forces in defining noncentrosymmetric order of high dipole moment-high hyperpolarizability chromophores in electrically poled polymeric thin films," *Proc. Nat. Acad. Sci. USA*, vol. 94, pp. 4842–4847, May 1997.

[7] W. Wang, D. Chen, H. R. Fetterman, Y. Shi, W. H. Steier, and L. R. Dalton, "Optical heterodyne detection of 60 GHz electro-optic modulation from polymer waveguide modulators," *Appl. Phys. Lett.*, vol. 67, no. 13, pp. 1806–1808, Sept. 1995.

[8] R. Lytel, "Applications of electro-optic polymers to integrated optics," in *Nonlinear Optical Materials and Devices for Photonic Switching, Proc. SPIE*, Jan. 1990, vol. 1216, pp. 30–40.

[9] W. Wang, D. Chen, H. R. Fetterman, Y. Shi, W. H. Steier, and L. R. Dalton, "Traveling wave electro-optic phase modulator using cross-linked nonlinear optical polymer," *Appl. Phys. Lett.*, vol. 65, no. 8, pp. 929–931, Aug. 1994.

of the Nd:YAG laser. Both beams were combined using a 2 × 2 fiber beam splitter and made incident on a photodetector. A 50-mW GUNN diode was used as the microwave source at 95 GHz. The spectrum analyzer trace of the downconverted signal at 95 GHz for the APII integrated phase modulator is shown in Fig. 4(b). This is an encouraging result for a phase modulator that has a $V_\pi = 16$ V, that corresponds to a V_π of 10.6 and 5.3 V in Mach–Zehnder and push–pull configurations, respectively.

To test the performance of the APII based modulators to 40 GHz, we fabricated a set of Mach–Zehnder devices on silicon substrates. The major fabrication steps were similar to those outlined for the devices on Mylar substrates. For an electrode–waveguide interaction length of 1.7 cm, the V_π of these devices in a Mach–Zehnder configuration was 10 V. In a push–pull configuration, this would correspond to a $V_\pi = 5$ V, which makes this new set of polymer devices acceptable for commercial applications. Two tunable diode pumped Nd:YAG lasers at 1.319 μm were used as sources for lower frequency

Demonstration of 110 GHz electro-optic polymer modulators

Datong Chen[a] and Harold R. Fetterman
Department of Electrical Engineering, University of California, Los Angeles, Los Angeles, California 90095

Antao Chen, William H. Steier, and Larry R. Dalton
Departments of Electrical Engineering and Chemistry, University of Southern California, Los Angeles, California 90089-0483

Wenshen Wang and Yongqiang Shi
TACAN Corporation, Carlsbad, California 92008

Electro-optic modulation up to 113 GHz has been demonstrated using traveling wave polymer modulators. The modulation signal was directly detected at 1.3 μm using a laser heterodyne system with an external-cavity tunable semiconductor laser. The device optical response variation, as a function of frequency over the whole W band, was within 3 dB. A well-matched coplanar probe was used to launch W band millimeter wave driving power into the microstrip line electrode on the device. Based upon these measurements, high speed electrodes with integrated millimeter wave transitions had been fabricated and tested. © *1997 American Institute of Physics.*
[S0003-6951(97)03125-2]

Polymer materials have become increasingly important for integrated optics[1] because of their low dispersion and fast electronic response. Decades of research[2-5] on nonlinear electro-optic polymer materials have made it possible to make high frequency photonic switching and modulating devices.[6-10] Recently our group demonstrated frequency response of an electro-optic polymer modulator up to 60 GHz,[10] and measured its frequency-length product to be well above 100 GHz cm.[11] However, in extending these measurements beyond 60 GHz, the millimeter wave circuits become more complex, and electro-optical phase modulation characterization becomes more demanding. In this letter, we report our latest high frequency measurement results over the whole W band (75–110 GHz) and up to 113 GHz.

The device being tested was a traveling wave polymer phase modulator.[12] The optical wave propagates along a vertically stacked optical ridge waveguide, which consists of a poled PUR-DR19 active core sandwiched between lower and upper claddings made of Epoxylite 9653. The driving millimeter wave electric field propagates along the microstrip line on top of the upper cladding in the same direction as the optical wave. Because of polymer's low index of refraction and low dispersion, we were able to use a straightforward traveling wave design to achieve velocity matching between the millimeter and optical waves. For high frequency operation, the main problems are to effectively couple the millimeter wave driving power into the microstrip line on the device and to reduce the microstrip line Ohmic loss. In this demonstration we used high frequency coplanar probes to drive the microstrip line electrode on the device in well-matched configurations at 61 GHz, and from 74 to 113 GHz.

A dc probe tip was used to precisely open small holes on the thin polymer dielectric layer at both sides of the microstrip line and to expose the ground contact regions. The distance between the coplanar probe tips is 100 μm, and the dielectric layer is only 10 μm thick so the three probe tips made an effective contact with a spring loaded contact

mechanism. We also measured the contact resistance before doing the measurement. To reduce the microstrip line Ohmic loss, we improved our fabrication process by changing our gold-plating recipe. A pulse/reverse current through a non-cyanide-based solution yielded a thicker line with improved morphology, reduced electrode resistance and Ohmic loss.

We used an optical heterodyne detection system to characterize our device.[10,13] This is a very sensitive method, independent of detector response, to characterize the electro-optic phase modulation at high frequencies. As the detector is illuminated by the phase modulated light mixed with a second laser, it generates a photocurrent:

$$i_D \propto \sqrt{I_1 I_2}\{J_0(\phi_1')\cos(\Delta\omega t + \Delta\phi) - J_1(\phi_1')\sin[(\Delta\omega + \Omega)t + \Delta\phi] - J_1(\phi_1')\sin[(\Delta\omega - \Omega)t + \Delta\phi]\}, \quad (1)$$

where I_1 and I_2 are the intensities of the lasers, J_0, J_1 are zeroth and first order Bessel functions of the first kind, ϕ_1' is the phase modulation amplitude, $\Delta\omega$ is the frequency offset of the two lasers, and Ω is the millimeter wave modulation frequency. The last term in Eq. (1) is the downconverted heterodyne signal. For small signal operation

$$J_1(\phi_1') \cong \frac{\phi_1'}{2} = \frac{\pi n^3 r_{33} l}{2\lambda h} V \propto V. \quad (2)$$

As shown in Eq. (1), the optical heterodyne technique is used to downconvert the high frequency optical phase modulated signal ($\sim$100 GHz) into a strong low frequency electrical amplitude modulated signal ($\sim$3 GHz) requiring only a low speed photodetector. Equation (2) indicates that the heterodyne signal is proportional to the phase modulation amplitude.

Figure 1 shows the high frequency electro-optic phase modulator characterization setup. A 1.319 μm laser beam from a fine tunable Ligthwave Electronics 122 YAG laser was coupled into the end of a single mode optical fiber, with the other end of the fiber cleaved. This cleaved end was brought very close to the input end of the optical waveguide of the device, using a piezoelectric translation stage, and the
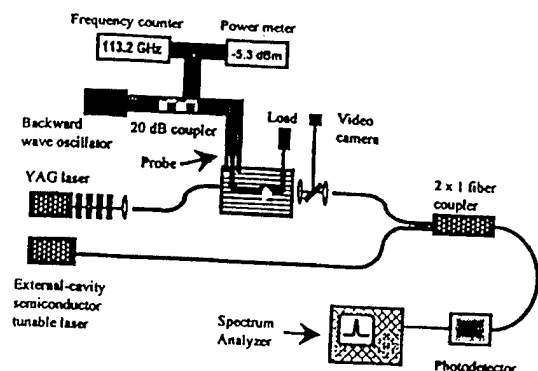
[a] Electronic mail: datong@ucla.edu

FIG. 1. Optical heterodyne setup for W-band electro-optic modulator characterization, a coplanar probe was used to couple the millimeter wave into the device, and an external-cavity semiconductor tunable laser was used to extend the detection frequency range.
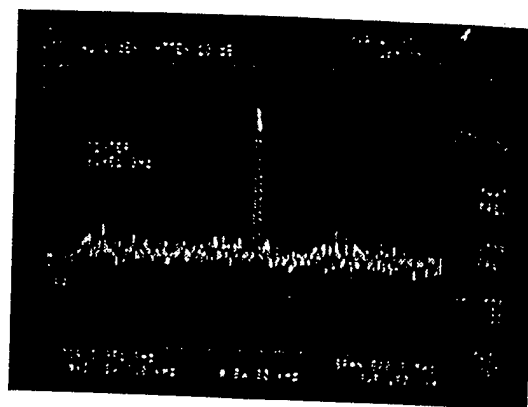

FIG. 2. Polymer modulator optical response at 105.8 GHz, optically down-converted to 3.9 GHz. The device was driven by a W-band backward wave oscillator.

light was directly butt coupled into the device. The modulated light output was then collected by a 20× microscope objective and fed into a single mode fiber through another 10× microscope objective. An Environmental Optical Sensors external-cavity semiconductor laser at 1.3 μm with a coarse tuning range of ~8 THz was used for the second beam of the heterodyne detection system. The two beams were combined through a 2×1 fiber coupler, rather than in free space, to reduce optical losses and to increase the optical alignment stability. Next, the combined beams were fed to a Fermionics photodetector, which can response up to 20 GHz. The output of the detector was amplified and displayed on an HP 8592 spectrum analyzer.

At first, the two lasers were turned on and an HP 70950B optical spectrum analyzer was used to find the wavelengths of the two lasers. We tuned the YAG laser frequency to the middle of its range, and tuned the external-cavity semiconductor laser so that the laser frequency offset was approximately equal to the intended millimeter wave modulation frequency. The tuning resolution of the external-cavity semiconductor laser was 1.7 GHz, and its power was set to 0.5 mW. When the millimeter wave power was turned on, the heterodyne signal appeared at low frequency on the spectrum analyzer. Fine tuning of the YAG laser brought the heterodyne signal to the desired preset frequency. When we changed the driving millimeter wave frequency, we also tuned the YAG laser frequency by the same amount so that the signal on the spectrum analyzer was always at the same reading to ensure a simple and reliable calibration. When the fine tuning YAG laser reached its maximum tuning range, we coarse tuned the external-cavity semiconductor laser to extend the frequency measurement range. Unlike the YAG laser, the external-cavity semiconductor tunable laser was not very stable in frequency with its frequency jumping about 100 MHz. The measurement span had to be increased to accommodate such a large drift and the noise floor was raised, thereby compromising the measured signal-to-noise ratio. Even in using these unlocked lasers, the signal was still quite high, due to the reduced optical insertion loss of our new devices.

Before we started to characterize our modulator at W-band frequencies, we tested the device at 61 GHz to re-

peat our previous 60 GHz performance[10] with V-band coplanar probes. Using W-band coplanar probes, we first observed the W-band phase modulation from the polymer modulator by using narrow band Gunn oscillators, which were relatively low noise and had about 20 mW output power at 94 GHz. Later we used several backward wave oscillators (BWO) as the microwave source to systematically characterize the device over the whole W band, and a typical measurement at 105.8 GHz is shown in Fig. 2. The BWOs were broadly tunable with output power levels ranging from a few mW up to 50 mW. A power meter and a frequency counter were used to closely monitor the millimeter wave driving power. After normalization for the millimeter wave driving power the device's optical response at different frequencies was plotted. As shown in Fig. 3, from 74 to 113 GHz, the device's optical response was characterized every 1 GHz, and exhibited a maximum variation of 3 dB. This 3 dB included the probe's frequency dependent coupling efficiency. The device's frequency characterization range was only limited by the commercial probe frequency response capability. Such a smooth response validated our predictions that the nonlinear electro-optic polymer materials work extremely well at high frequencies. Combined with our previous work at lower frequencies,[10] the current measurements indicate that these devices can operate effectively over the entire
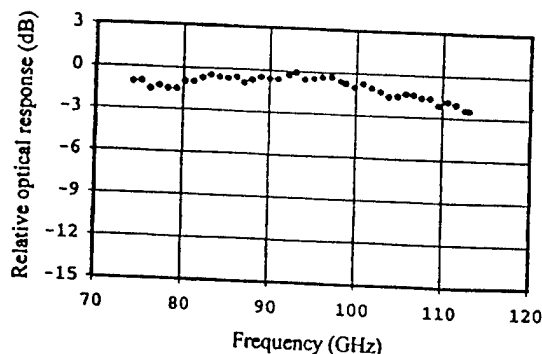

FIG. 3. High frequency optical response curve of the polymer modulator from 74 to 113 GHz. The total variation was less than 3 dB.
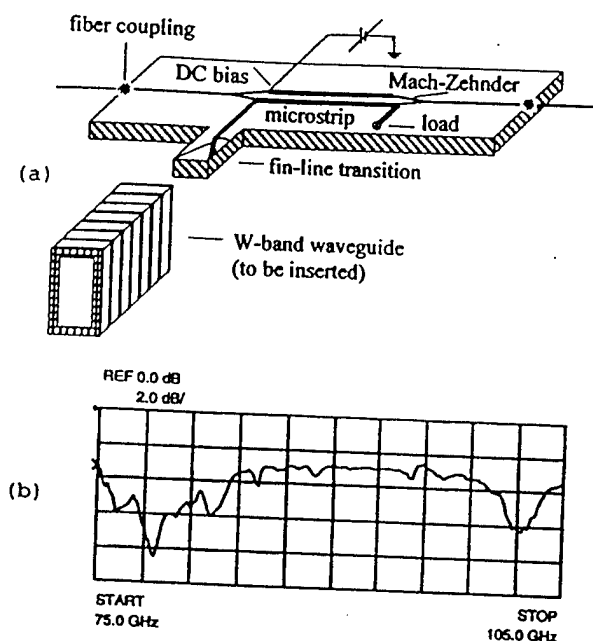
Chen *et al.*

FIG. 4. (a) Overview of the device with an integrated W-band antipodal fin-line transition. The transition section is to be inserted into the microwave waveguide for high speed device operation. (b) Measured W-band S_{21} of a test circuit.

range from 0 to 110 GHz. Also, on the high frequency plot no resonance appears, indicating that the coplanar probes were well matched to the microstrip lines on the devices.

Based upon these prototype demonstrations, we wanted to develop more robust, less costly devices which do not require the use of commercial rf probes. We have designed and made fin-line structures to effect the monolithic transition between our W-band microwave waveguide sources and various electrode configurations on the device. As shown in Fig. 4(a), such transitions gradually transformed the electric field profile and the impedance of the millimeter wave waveguide to that of the microstrip line electrode. Figure 4(b) is the measured W-band S_{21} of our test circuit for these monolithic modulators, fabricated on a Duroid 5880 substrate, and consisting of two antipodal fin-line transitions and a 4 cm long microstrip line.

In addition to our effort in extending our modulator's frequency response, processing parameters have now been

well characterized and optimized to reduce the optical insertion loss. Furthermore, a new tapered guide technique to make an optical mode match between optical fiber and device optical waveguide has been developed, so that our optical insertion losses can now be reduced to less than 5 dB. Integration of the polymer modulator with various semiconductor drivers on a single chip has also been studied in detail.[14]

In conclusion, we have successfully fabricated and characterized the electro-optic polymer modulators up to 113 GHz. Other key figures of merit including transmission efficiency have also been improved. These devices work at extremely high frequencies, can be configured with integrated microwave transitions, and can be easily fabricated into arrays, having both parallel and series configurations. They will provide an inexpensive alternative to conventional devices, and offer exciting new application areas.

[1] *Polymer for Lightwave and Integrated Optics: Technology and Applications*, edited by L. A. Hornak (Marcel Dekker, New York, 1992).

[2] J. Zyss, *Molecular Nonlinear Optics: Materials, Physics, and Devices* (Academic, Boston, 1994).

[3] *Polymers for Second-Order Nonlinear Optics*, edited by G. A. Lindsay and K. D. Singer (American Chemical Society, Washington, DC, 1994).

[4] D. M. Burland, R. D. Miller, and C. A. Walsh, Chem. Rev. **94**, 31 (1994).

[5] *Nonlinear Optical Properties of Organic Molecules and Crystals*, edited by D. S. Chemla and J. Zyss (Academic, Orlando, 1987).

[6] D. G. Girton, S. L. Kwiatkowski, G. F. Lipscomb, and R. S. Lytel, Appl. Phys. Lett. **58**, 1730 (1991).

[7] J. I. Thackara, J. C. Chon, G. C. Bjorklund, W. Volksen, and D. M. Burland, Appl. Phys. Lett. **67**, 3874 (1995).

[8] C. C. Teng, Appl. Phys. Lett. **60**, 1538 (1992).

[9] S. Ermer, J. F. Valley, R. Lytel, G. F. Lipscomb, T. E. Van Eck, and D. G. Girton, Appl. Phys. Lett. **61**, 2272 (1992).

[10] W. Wang, D. Chen, H. R. Fetterman, Y. Shi, W. H. Steier, L. R. Dalton, and P. D. Chow, Appl. Phys. Lett. **67**, 1806 (1995).

[11] W. Wang, D. Chen, H. R. Fetterman, Y. Shi, W. H. Steier, and L. R. Dalton, IEEE Photon Technol. Lett. **7**, 638 (1995).

[12] Y. Shi, W. Wang, J. H. Bechtel, A. Chen, S. Garner, S. Kalluri, W. Steier, D. Chen, H. R. Fetterman, L. R. Dalton, and L. Yu, IEEE J. Selected Topics Quantum Electron. **2**, 289 (1996).

[13] T. S. Tan, R. L. Jungerman, and S. S. Elliott, IEEE Trans. Microwave Theory Tech. **37**, 1217 (1989).

[14] S. Kalluri, M. Ziari, A. Chen, V. Chuyanov, W. H. Steier, D. Chen, B. Jalali, H. R. Fetterman, and L. R. Dalton, IEEE Photon Technol. Lett. **8**, 644 (1996).

Appl. Phys. Lett., Vol. 70, No. 25, 23 June 1997

Chen *et al.* 3337

Microwave Phase Conjugation Using Antenna Arrays

Yian Chang, Harold R. Fetterman, *Fellow, IEEE,* Irwin L. Newberg, *Life Member, IEEE,* and Steve K. Panaretos

Abstract— A technique has been developed and tested for achieving phase conjugation in the microwave and millimeter-wave regime. The effective nonlinearity required for this phase-conjugation process is provided by electronic mixing elements feeding an array of antennas. Using these balanced mixing circuits in conjunction with a one-dimensional array antenna, we have demonstrated two-dimensional free-space phase conjugation at 10.24 GHz. A critical factor of this technique is the delivery of a 2ω pump signal to each array element with the same phase. Two types of interconnects, electrical and a more versatile optical technique, have been implemented to distribute the pump signal in our demonstrations. In both systems, two-dimensional free-space phase conjugation was observed and verified by directly measuring the electric-field amplitude and phase distribution under various conditions. The electric-field wavefronts exhibited retro-directivity and the auto-correction characteristics of phase conjugation. Furthermore, these experiments have shown amplified conjugate-wave power up to ten times of that of the incoming wave. This amplifying ability demonstrates the potential of such arrays to be used in novel communications applications.

Index Terms—Antenna arrays, microwave, optical interconnection, phase conjugation.

I. INTRODUCTION

THE engineering community has been interested in dynamically constructing desired wavefronts of electromagnetic (EM) waves for many years. Consequently, there has been a significant amount of theoretical and experimental work on this subject. The development of such techniques in the microwave and millimeter-wave regime has concentrated on phased-array antennas. The idea behind these phased arrays is fairly simple: by controlling the amplitudes and phases of discrete antenna elements, any wavefront can be dynamically generated or detected. In the past decade, researchers have been trying to realize compact phased-array systems with broad-band capabilities. The most promising concept calls for optically controlled designs because photonic components are small, light, broad-band, and relatively immune to EM interference. In this paper, special types of phased arrays, which incorporate phase-conjugate elements, have been developed and implemented. These phase-conjugation arrays can be thought of as automatically configured phased-array
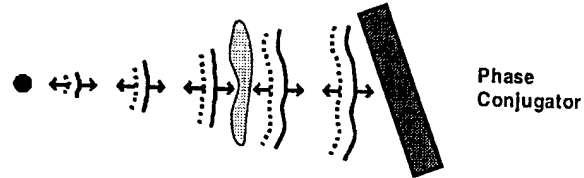
Fig. 1. Phase-conjugation properties: retro-directivity and automatic wavefront correction.

systems, which are capable of directing their outgoing signals back to the illuminating sources. We have demonstrated two-dimensional free-space phase conjugation at 10.24 GHz using both conventional microwave and novel photonic designs.

Phase conjugation, in general, utilizes the nonlinear susceptibility of a medium to reverse the phase factor of an incoming wave. A phase-conjugate wave propagates backward and has the same wavefronts as those of the incoming wave, as shown in Fig. 1 [1], [2]. This unique property of phase-conjugate waves is useful in many novel applications, including automatic pointing and tracking [3], phase aberration correction [4], and phase-conjugate resonators [5]. To further reveal phase-conjugation properties, let us consider an EM wave propagating along the positive z-direction. Its electric field can be written as

$$\mathbf{E} = \mathbf{A}(\mathbf{r})e^{i[\omega t - kz - \varphi(\mathbf{r})]} + \text{c.c.} \tag{1}$$

where ω is the angular frequency and k is the wavenumber of the EM wave. The amplitude $\mathbf{A}$ and the phase φ are real functions of position $\mathbf{r}$. Normally, $\mathbf{A}$ is a slow-varying function of z compared with $e^{i[\omega t - kz - \varphi(\mathbf{r})]}$, therefore, the wave propagation can be understood in terms of the motion of wavefronts, which are three-dimensional surfaces defined by

$$kz + \varphi(\mathbf{r}) = \text{constant.} \tag{2}$$

The phase-conjugate wave of (1) is defined as

$$\mathbf{E}_C = \mathbf{A}(\mathbf{r})e^{i[\omega t + kz + \varphi(\mathbf{r})]} + \text{c.c.} \tag{3}$$

Comparing (1) and (3), it is shown that the two waves have the same wavefronts at any point in space, but they travel in opposite directions. Also notice that the conjugate wave can be obtained by a time-reversal $t \rightarrow -t$ transformation or by taking the complex conjugate only of the spatial part of the electric field.

To appreciate the properties of phase conjugation, let us consider a plane wave propagating through a distorting medium. Due to the nonuniform distribution of refractive

index $n(\mathbf{r})$, the incident wavefronts are no longer planar after passing through the distorting medium. Equations (1) and (3) have shown that the conjugate wave has the same wavefronts as those of the incident wave. It can be proven the phase-conjugate wave satisfies Maxwell's equations, therefore, it propagates backward as the time-reversed incident wave through both space and the distorting medium and, consequently, the distortion is automatically removed [2]. Another important feature of phase conjugation is that we only need to generate the conjugate field $\mathbf{E}_c$ on one plane, this field will propagate backward and remain the phase-conjugate field of $\mathbf{E}$ everywhere [2]. This enables the possibility of accomplishing microwave and millimeter-wave phase conjugation using electronic-mixing phased-array antennas system.

To date, most of the phase-conjugation development has been concentrated in the optical [visible and infrared (IR)] regime. Efforts to extend this technique to microwave and millimeter-wave frequencies have encountered severe difficulties due to the small nonlinearity of natural materials and the low-power density of sources at these frequencies. To examine this problem, let us consider the phase-conjugation efficiency of degenerate four-wave mixing (DFWM) [2] techniques. Applying nominal parameters, this efficiency is lowered by about 16 orders of magnitude as one tries to extend optical DFWM techniques into microwave and millimeter-wave regime [6]. This drastic efficiency loss presents severe difficulties for microwave and millimeter-wave phase conjugation.

One possible solution for the above-mentioned efficiency problem is to increase the nonlinear susceptibility by many orders of magnitude. In the search for alternative nonlinear substances suitable for the use in microwave and millimeter-wave phase conjugation, artificial Kerr media were found to have much larger nonlinearity than that of natural materials. Using shaped microparticle suspensions [7] and microelectromechanical system (MEMS) structures [8], [9], volume grating formation for microwave phase conjugation has been demonstrated with DFWM techniques. Although these artificial Kerr media have demonstrated $\chi^{(3)}$ as high as 10^{-4} cm $\cdot$ s^2/g [6], they have a number of intrinsic problems. Due to the required movements of macroscopic particles in viscous fluid or polyimide supported metal beams in air, these media suffer from slow response time and are sensitive to surrounding conditions. Therefore, these techniques are not suitable for practical systems and applications.

II. ANTENNA-ARRAY APPROACH

Due to the above-mentioned difficulties in achieving microwave phase conjugation using traditional DFWM techniques, this paper approaches the problem from a very different perspective. Instead of using third-order nonlinear dipoles ($\chi^{(3)}$), as in DFWM, electronic-mixing phased arrays are used in a second-order three-wave mixing configuration to provide a high artificial nonlinearity for generating phase-conjugate waves. In this approach, microwave circuits, which combine antennas and mixers, effectively replace the roles of nonlinear dipoles of a medium. The idea is to "sample" the incident
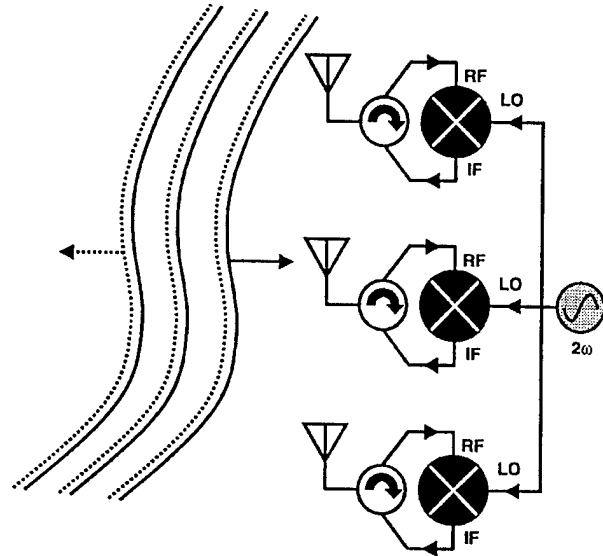

Fig. 2. First, the incident wavefront is sampled at different positions. Each element then generates a phase-conjugate current using microwave circuitry. This current will excite a phase-conjugate field at the sampling point. The superposition of these fields becomes the phase-conjugate wave.

wave at different positions of the wavefront using antenna elements and then generate phase-conjugate currents using microwave mixers. These currents will then excite a phase-conjugate field at each sampling point. The combined field of all the elements will be the phase-conjugate field of the incident beam. This sample-then-mix concept is shown in Fig. 2. It was first proposed in the 1960's, but due to the lack of modern semiconductor and photonic technologies, researchers did not have practical ways to realize this concept [10], [11].

To understand how the conjugate signal can be generated at each element using microwave circuitry, let us consider again the incident wave shown in (1). At the jth element of the array, the incoming electric field is

$$\mathbf{E} = \mathbf{A}(\mathbf{r}_j)e^{i(\omega t - \varphi_j)} + \text{c.c.} \tag{4}$$

where

$$\varphi_j = kz_j + \varphi(\mathbf{r}_j). \tag{5}$$

The signal picked up by the antenna and then sent to the mixer can be written as

$$V_{j1} \propto A(r_j)e^{i(\omega t - \varphi_j)} + \text{c.c.} \tag{6}$$

Now consider a 2ω signal delivered to the local oscillator (LO) port of the mixer given by

$$V_{j2} = Ce^{2i\omega t} + \text{c.c.} \tag{7}$$

This 2ω pump signal has to be delivered to all elements at the same amplitude and phase; otherwise, the mixed output will contain a term other than V_{jl} that depends on j. If this ever happens, the sum of the excited field at each element will be distorted and will not form the conjugate beam. Now, through different frequency generation in the mixer, the intermediate frequency (IF) output contains a current component

$$I_C \propto e^{2i\omega t} \times e^{-i(\omega t - \varphi_j)} = e^{i(\omega t + \varphi_j)}. \tag{8}$$

This current component has the conjugate-phase $+\varphi_j$ instead of the input phase $-\varphi_j$, therefore, it will excite the conjugate field at r_j when delivered to the antenna

$$\mathbf{E}_{C_j}(\mathbf{r}_j) \propto \mathbf{A}(\mathbf{r}_j)e^{i(\omega t + \varphi_j)} + \text{c.c.} \qquad (9)$$

When the sampling spacing is less than $\lambda/2$, the combined field $\mathbf{E}_c(\mathbf{r}) = \sum_j \mathbf{E}_{C_j}(\mathbf{r})$ forms the phase-conjugate signal on the sampling surface. It has been discussed earlier that if a phase-conjugate field is generated on a plane, it will propagate backward and be conjugate to the incident beam everywhere. Therefore, $\mathbf{E}_C(\mathbf{r})$ is the desired phase-conjugate field. In the past three years, various groups have explored retro-directive phased arrays utilizing this concept [12], [13]. These studies have concentrated on the retro-directive property of phase conjugation. In this paper, we focus on wavefront properties and reconstruction, and also investigate optical interconnection for the 2ω pump signal so that large phase-conjugation arrays can be constructed with less complexity.

There is an important issue we have to address here. Unlike any of the traditional phase-conjugation techniques, which utilize virtually infinite dipoles as far as our concern, this array approach can only have a limited number of elements because of economic and engineering constraints. To clarify the effects caused by a finite number of elements, the phase-conjugate wave of a dipole source has been calculated for three phase-conjugate arrays having different number of elements. The first array was formed by eight elements, the second one by 40 elements, and the third one by 200 elements. For the eight- and 40-element arrays, the spacing between elements was chosen to be 0.467λ. The 200-element array had a spacing of 0.093λ, which was one-fifth of that of the 40-element array. Therefore, the 40-element array had five times the aperture size of the eight-element one, with the same sampling density. The 200-element array had the same aperture size as the 40-element one, but with five times the sampling density. The antenna elements were assumed to have dipole radiation patterns and collinear axes.

In the calculation, the center of each array was used as the origin. The wavelength was assumed to be 3 cm, which corresponds to 10 GHz in frequency. Fig. 3 shows the conjugate electric-field magnitude distribution generated by the eight-element array at a given time. It clearly exhibits retro-directivity, but does not show the conjugate beam focusing back to the source. This is caused by the diffraction effects of a small aperture size. The conjugate electric-field distribution of the 40-element array is shown in Fig. 4. It demonstrates fairly well wavefront reconstruction, as well as retro-directivity and focusing can be clearly seen. The calculated conjugate field distribution of the 200-element array displays no perceivable improvement over the 40-element one. Therefore, a sampling spacing slightly less than $\lambda/2$ is acceptable for most cases. If the spacing is greater than $\lambda/2$, grating sidelobes can develop and, therefore, destroy the conjugate wavefront patterns.

From these comparisons, we have seen the main factor determining that the resolution is not the sampling density (as long as it is greater than $2/\lambda$), but the aperture size. If we require the phase conjugator to have a high resolving power, equally spaced arrays with $< \lambda/2$ spacing, like the examples,
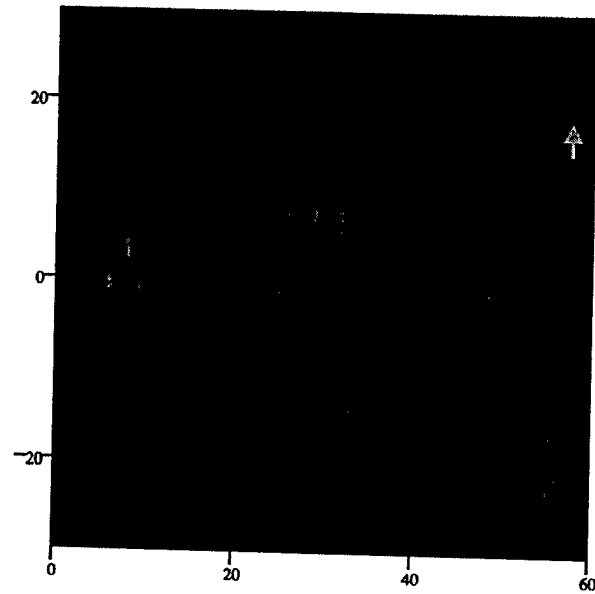

Fig. 3. The calculated conjugate electric-field magnitude distribution generated by an eight-element array. Brighter areas represent higher field. The element spacing is 0.467λ and a dipole source is located at (57.9 cm, 15.6 cm), as marked by the arrow. Only retro-directivity is observable in this configuration because of diffraction effects.
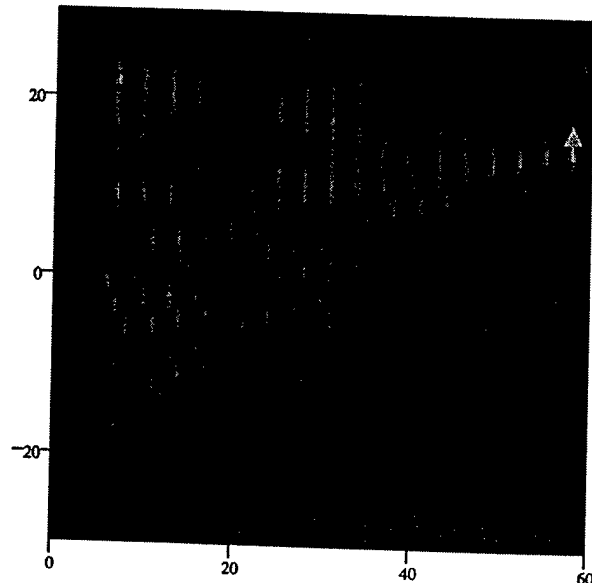

Fig. 4. The calculated conjugate electric-field magnitude distribution generated by a 40-element array. The element spacing is 0.467λ. Both retro-directivity and focusing can be clearly observed at this aperture size.

will not be practical, as the number of elements will be astronomical. For example, a resolving power of 10^{-5}–10^{-4} rad could require 4×10^8 to 4×10^{10} elements. However, using randomly distributed elements over the aperture to prevent the development of grating lobes can dramatically reduce the number of elements required in a sparse array [14].

III. ELECTRICAL-INTERCONNECTION EXPERIMENTS

The concepts of microwave phase conjugation using electronic-mixing antenna arrays have been discussed in

Section II. To prove the feasibility of this approach, we have built an array of eight phase-conjugate elements to demonstrate the generation of phase-conjugate waves. The equipment and devices available to us limited the number of elements used in this demonstration. Although an eight-element array would not be able to focus a diverging incident beam back to its source due to diffraction limitations (as calculated in Section II), it should exhibit retro-directivity and can demonstrate phase autocorrection when a distortion medium is introduced into the beam path. These two key characteristics of phase conjugation are strong evidences of the feasibility of this technique.

Since microwave components have relatively large loss, size, and weight, and are more susceptible to EM interference, we find that optical interconnection is the crucial technology for constructing large microwave phase-conjugate arrays. However, for an eight-element demonstration array, it is still feasible to build a system using straightforward microwave interconnects. Therefore, in this section, we will first discuss the construction and measurements of an electrically interconnected phase-conjugate array. Its optically interconnected counterpart will be considered in Section IV.

As mentioned in Section II, each element of a phase-conjugate array will excite the conjugate field at its sampling position via difference frequency generation. In an ideal elementary configuration, the sampled signal goes through a circulator into a low-noise amplifier. This amplifier provides compensation to the conversion loss of the mixing process in the next step. It can also provide gain so that the conjugate signal is more intense than the input one. After mixing with the 2ω pump signal in a mixer, the output IF signal has the conjugate phase and it is sent back to the sampling antenna through the circulator. In this configuration, the antenna has to be very efficient. The reason is that any reflection of the conjugate signal from the antenna will go through the circulator, as it were the sampled incident signal. This will affect the phase of the output signal and, thus, destroy the conjugate-phase generation. If the reflection is large enough, the circuit will even start oscillating by itself. To study this more closely, let us assume the return loss of the antenna is R, gain of the amplifier is G and conversion loss of the mixer is C. R, G, and C are complex output to input voltage ratios to include the phase change at each stage. The circulator and mixer are assumed to be perfect, no unwanted signal leakage between their ports. In order to generate the phase-conjugate wave, we require that the reflected conjugate signal be much smaller than the sampled signal. This requirement can be written as

$$G \cdot C \cdot R \ll 1 \tag{10}$$

and when $G \cdot C \cdot R = 1$, the system starts to oscillate.

Commercial mixers normally have a conversion loss around 10 dB, which corresponds to $|C| = 0.32$. With a specially designed narrow-band antenna array, a 30-dB return loss can be achieved. This corresponds to $|R| = 0.032$. Equation (10) gives us $|G| \ll 100$. If we choose $|G| = 10$, the phase-conjugate signal will be ten times more powerful than the incident signal. Unfortunately, the antenna array available to us had a return loss of about 7 dB at the desired
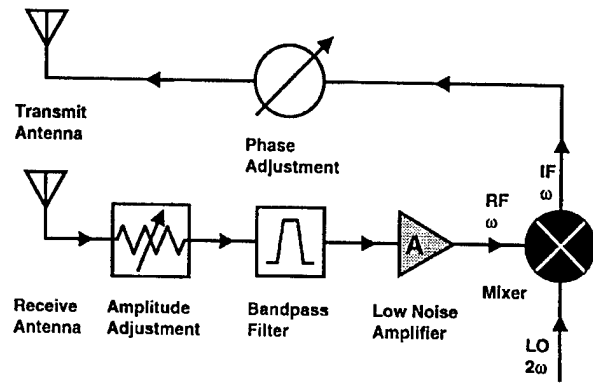

Fig. 5. The configuration of a phase-conjugate element used in this paper. The transmit and receive antennas are separated. A bandpass filter, phase adjustment, and amplitude adjustment are added to the circuit.

10.24 GHz, which corresponded to $|R| = 0.45$. This high reflection was a direct consequence of the wide-band design of the antenna array. Applying (10), we obtained $|G| \ll 7$. Basically, this means there could be no gain in this phase-conjugate element. Therefore, we somehow needed to reduce the antenna reflection.

Since we planned to demonstrate a two-dimensional free-space phase conjugation using a one-dimensional electronic-mixing antenna array, instead of designing new antennas, we had chosen to separate the transmit and receive antennas. This means the sampling of the incident field and the excitation of the conjugate field happened at the same (x, y) coordinates, but at a slightly different vertical z-coordinate. This small shift in the z-direction would only disturb the electric-field distribution on the $z = 0$ plane to a negligible level.

The modified elementary configuration used in this paper is shown in Fig. 5. An amplitude adjustment and a phase adjustment had been added to the configuration to compensate for any differences between the phase-conjugate elements because the amplifiers and mixers were not matched. By displaying and comparing the output signal of each element to a reference signal using a computer-controlled digital sampling oscilloscope (DSO), the phase and amplitude of each element could be measured and adjusted. The amplitudes of all phase-conjugate elements were first matched with different attenuators to within ±2%. The phases were then matched to within ±0.2 ps (0.2%) by adjusting the variable delay line of each element.

The mixer is the key component of the phase-conjugate element. It provides the nonlinearity for generating phase-conjugate waves. In this study, MY50C triple-balanced mixers from Watkins–Johnson were used. The conversion loss of these mixers at 10.24-GHz input and output signals with a 20.48-GHz pump (LO) signal is around 10 dB. The leakage from the input (RF) to the output port (IF) of the mixer is about −20 dB. Therefore, the unwanted 10.24-GHz input leakage is 10 dB smaller than the desired phase-conjugate output signal. This can be further reduced by designing mixers for the desired frequency or by using a two-stage mixing technique. In a two-stage mixing element, the undesired incoming frequency can be filtered out by a bandpass filter after the first-stage mixing.
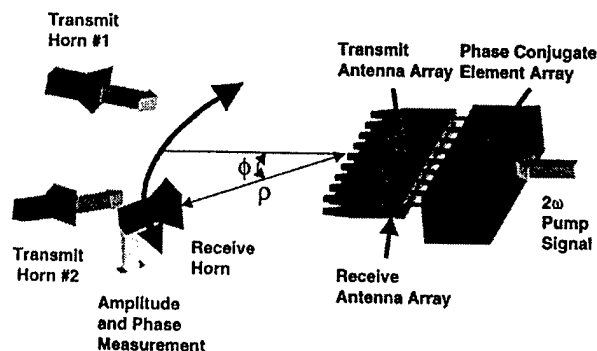
Fig. 6. This setup is used to map out two-dimensional electric-field magnitude distribution. The receive horn is at a lower height than the transmit horns to prevent blocking of the incident beams. It can be moved to different positions to measure the electric-field strength.

This filtered signal can then be mixed in the second stage to produce the final conjugate signal. Again, a second bandpass filter can filter out any undesired leakage signals. This four-wave mixing technique can achieve higher isolation between the incoming signal and the conjugate signal at the cost of an additional pump source for each element. The details of this technique will be explained later.

To demonstrate microwave phase conjugation using the eight-element electronic mixing array, we prepared an electric-field mapping setup in an anechoic chamber, shown in Fig. 6. As mentioned earlier, the transmit and receive antennas of the conjugator were separated in the z-direction (height) by 1.4 cm. One or two transmit horns were used as illuminating sources. Both transmit horns were 60 cm from the conjugator. This distance was chosen because of the sizes of the chamber and conjugator. The receive horn was mounted on a translation stage for radial movement. Its distance to the conjugator (ρ) was varied at 0.5 cm intervals from $\rho = 45$ cm to $\rho = 55$ cm. The translation stage itself was mounted on a stepping motor stage for angular control. A computer controlled the rotation stage at $1°$ intervals from $\phi = -30°$ to $\phi = 30°$. The signal detected by the receive horn was proportional to the electric field at that point and was amplified and then displayed on a DSO. By comparing the received signal to a reference signal using a computer, the amplitude and phase of the electric field at the receiving horn position could be accurately measured.

In the first set of measurements, only one transmit horn was used as the source. It was placed at $\phi = 15°$. This angle was chosen for convenience, it could be varied between $-30°$ to $30°$. The conjugate electric-field distribution is shown in Figs. 7 and 8, labeled as "without distortion." In the contour plot of Fig. 7, gray scale is used to represent the magnitude of the electric field. The black dot next to the plot is the source location. The phase-conjugate array is located on the left of each plot and the tick mark labels are in centimeters. The wavefronts of the conjugate wave can be seen clearly, and are traveling from left to right. Although the focusing effect cannot be observed because of the diffraction limits, retro-directivity is certainly demonstrated. In the surface plot of Fig. 8, the electric-field magnitude is represented by the height at a given
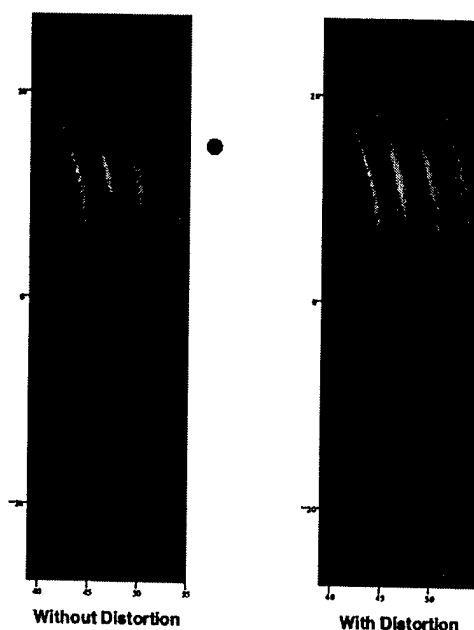

Without Distortion   **With Distortion**

Fig. 7. The contour plots of the measured phase-conjugate electric field of a source at $+15°$, as marked by the black dots. The high-contrast areas represent the conjugate beams, and the faint fringes are due to leakage. They demonstrate retro-directivity and automatic phase correction when a distorting medium is inserted in front of the conjugator.

point. The white dot on the zeroth-field plane marks the source position. The smaller bumps in this figure were caused mainly by the amplified incident signals leaking through the mixers. This amplitude of the electric field was about one-third to one-fourth of that of the conjugate beam. This means the leakage power was about -10 dB of the conjugate power, as mentioned earlier in this section.

Our next step was to demonstrate automatic phase correction. This was achieved by inserting a distorting medium in front of the phase conjugator. We used a piece of Plexiglas as the distorting medium. The conjugate electric field is shown in Figs. 7 and 8, labeled as "with distortion." By comparing the fringes of the two plots in Fig. 7, the wavefronts of the conjugate beam remained the same shape and phase with or without the distortion, as the theory predicted. The leakage wavefronts were distorted when the distorting medium was present. In Fig. 8, the leakage bumps were again destroyed by the distortion, while the phase-conjugate beam maintained its phase and amplitude. These results unambiguously demonstrate the retro-directivity and automatic phase correction ability of this microwave phase conjugation.

In order to reveal the automatic phase correction more quantitatively, the receive horn was placed in the conjugate beam at 55 cm from the conjugator. The electric field versus time was recorded and then compared with and without the distortion. The phase difference in time was less than 1 ps for a distorting medium capable of 25-ps one-way delay. To further demonstrate that the phase-conjugate beam does carry a negative incident phase, we moved the distorting medium to cover the source only. Therefore, only the incident beam went through the distortion. The electric-field distribution is
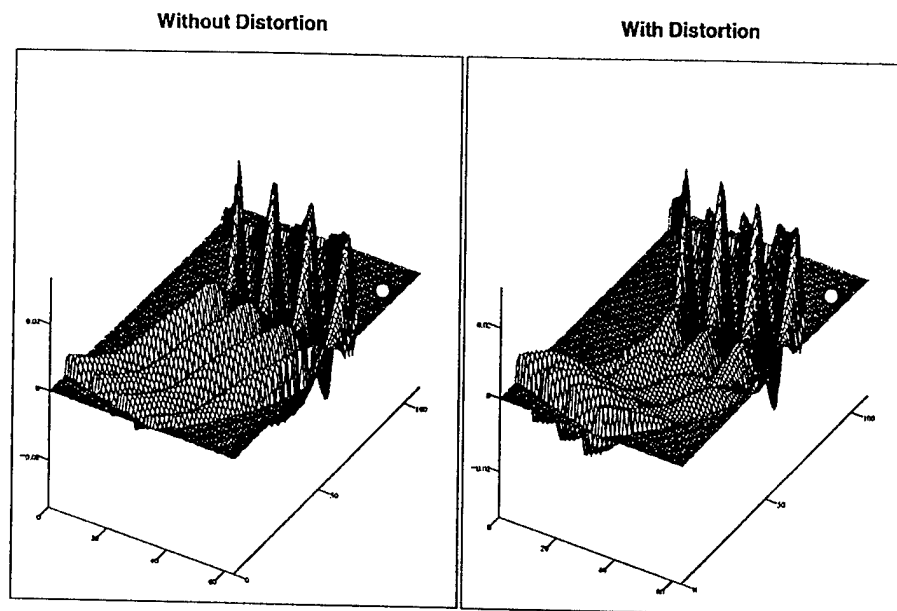
Without Distortion   **With Distortion**

Fig. 8.   The surface plots of the phase-conjugate electric field of a source at +15°, as marked by the white dots. They show retro-directivity and automatic phase correction. The smaller bumps are caused by amplified leakage and are destroyed by the distortion.

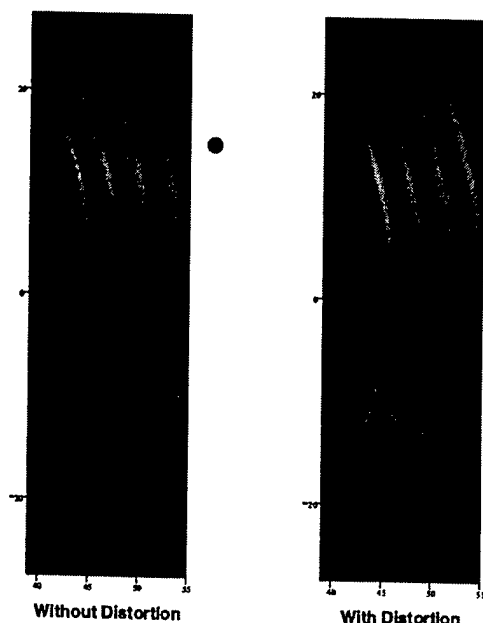**Without Distortion**   **With Distortion**

Fig. 9.   This data is taken with the distorting medium covering only the transmit horn. The conjugate beam now has advanced wavefronts, while the reflected beam is distorted and has retarded wavefronts.

shown in Fig. 9, labeled as "with distortion." Due to the existence of the distorting medium, the phase of the incident beam was retarded by $\Delta\varphi$. If this signal was leakage, it would carry the same phase retardation $\Delta\varphi$. However, if the incident beam was phase-conjugated by the conjugator, the phase of the conjugate beam would be $-\Delta\varphi$, which means its phase was advanced by $\Delta\varphi$. This theory is shown in Fig. 9 as the conjugate wavefronts moved toward the source (advanced phase), while the leakage wavefronts moved

toward the conjugator (retarded phase). Also noticeable in Fig. 9, the leakage beam was deflected away from the center because of the distortion. This shows the Plexiglas did act as an effective distorting material and further confirms the previous experiments.

IV. OPTICAL-INTERCONNECTION EXPERIMENTS

As mentioned earlier, electrical interconnection will not be able to handle a large two-dimensional phase-conjugate array for complete three-dimensional wavefront reconstruction. The problems in the electrical scheme are due to the high loss, heavy weight, and large size of microwave and millimeter-wave components. It is also more susceptible to EM interference. In contrast, using optical interconnection, the 2ω pump signal can be delivered to all elements with very little loss ($\sim$0.3 dB/Km) at very high density (e.g., 1 element/millimeter for millimeter-wave arrays). Therefore, in this paper, we propose and demonstrate the optical-interconnection technique to address these electrical-interconnection problems.

In this optical-interconnection scheme, the eight phase-conjugate elements were the same as in the electrical configuration shown in Fig. 5. A Lightwave 122 diode-pumped Nd:YAG laser was used as the light source. The optical wavelength was at 1319 nm, with a linewidth $\leq$5 KHz. This wavelength was chosen to minimize the dispersion in optical fiber systems. In our demonstration, it was not an important issue because of the relatively short propagation distances. However, to be able to extend this technique into large arrays and/or millimeter-wave frequencies, minimized dispersion will be a crucial factor.

The laser light was directed into a Mach–Zehnder optical modulator using a polarization preservation fiber. The modulator was biased at its transfer function halfway point for optimal linear modulation. The 10.24-GHz signal was

frequency-doubled to 20.48 GHz, amplified, and then used to modulate the laser light. A more interesting way to modulate the light at 2ω is to bias the modulator at its transfer function minimum and apply an ω signal to its RF electrode. Due to the nonlinearity of the transfer function at the minimum, the optical power varies at 2ω as desired. The advantage of this technique is that no microwave frequency-doubler is required. The disadvantage is that it is very sensitive to the bias of the transfer function. Even small fluctuations will result in loss of modulation efficiency and unwanted linear modulation. Therefore, the bias point has to be monitored closely by a feedback loop.

This 2ω modulated light can now be delivered to photodetector-attached phase-conjugate elements, which may be far away for a large array or close together for high operating frequencies. In this paper, this 20.48-GHz modulated light entered an 1 × 8 optical power splitter and split into eight equal-intensity equal-phase signals. The 20.48-GHz pump signal was then extracted by a p-i-n diode at each element. This pump signal was amplified to a power level of 9 dBm, and then fed to the phase-conjugate element, as in the electrically interconnected system.

Using the experimental setups and procedures mentioned earlier, the output amplitudes of these eight elements were matched to within ±6% and their phases were matched to within ±0.2 ps (0.2%). After this calibration, we were able to demonstrate two-dimensional microwave phase conjugation using the optically interconnected electronic-mixing array. All the tests performed in the electrical demonstration have been successfully duplicated.

To demonstrate phase conjugation with more complicated wavefronts, we used two sources locate at 15° and −20°, both were 60 cm from the conjugator. Due to the interference between the two sources, the combined incident wavefronts represented a good example of complicated wavefronts. The results are shown in Fig. 10, labeled as "without distortion." They exhibit multiple-source retro-directivity with both conjugate beams shifted ~3° toward the negative angles. This was caused by the interference between the leakage of one source and the conjugate beam of the other. To prove this point, the following test was performed. First, the horn at −20° was disconnected from the source and the conjugate field of the +15° horn was recorded. Then the horn at +15° was disconnected and the field of −20° was measured. In both cases, retro-directivity was shown without the angular shift. A computer then added up the two single-source electric fields. The calculated sum field showed the same angular shift and was almost identical to the measured two-source electric field. Therefore, the interference from the leakages was causing this problem and can be solved by using two-stage mixing to avoid leakage. In order to verify the phase-correction ability, a distorting medium was inserted in front of the conjugator. The conjugate electric-field distribution is shown in Fig. 10, labeled as "with distortion." By comparing the two plots in Fig. 10, the automatic phase-correction effect can be confirmed. It can also be noticed that the small angular shift disappeared when the distortion was present. This is because the existence of the distorting medium destroyed the leakage
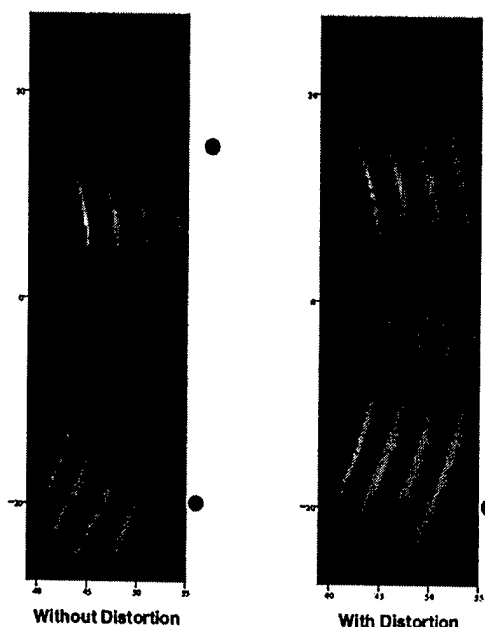

Without Distortion   **With Distortion**

Fig. 10. The phase-conjugate electric-field distribution of two sources at +15° and −20°, obtained using an optically interconnected phase-conjugate array. These plots demonstrate multiple-source retro-directivity and automatic phase correction when a distorting medium is inserted in front of the conjugator.

signal while maintaining the conjugate signal, as shown in previous experiments.

To test that a phase conjugator can transmit information back to the source, we A.M. modulated the 20.48-GHz pump signal before it was used to modulate the light. In this example, the modulation frequency was set to 10 MHz. This frequency was chosen by convenience and can be varied as long as it is small compared to the phase-conjugation frequency. If it becomes comparable to the phase-conjugation frequency, the output signal will not be the conjugate beam any more. The two sources used in the previous experiments were used to illuminate the conjugator. The detected spectra at different angles are shown in Fig. 11. The top spectrum was detected in the +15° conjugate beam. It shows the 10.24-GHz carrier and two A.M. modulation sidebands at 10.23 and 10.25 GHz. The bottom spectrum was detected in the −20° conjugate beam and it shows the same characteristics as the +15° one. When the receive horn was moved out of the conjugate beams to 0°, the carrier and sidebands were about 20 dB lower than those of the conjugate beams. The signal detected here was mainly due to diffraction and leakage. Using a large phase-conjugate array and two-stage mixing, this contrast ratio can be further increased because of the reduction of diffraction effects and mixer leakage.

V. CONCLUSIONS

Thus far, we have demonstrated two-dimensional microwave phase conjugation in free space. In order to extend this effort to complete three-dimensional wavefront reconstruction, two-dimensional arrays will have to be used. At microwave frequencies, a phase-conjugate array can be
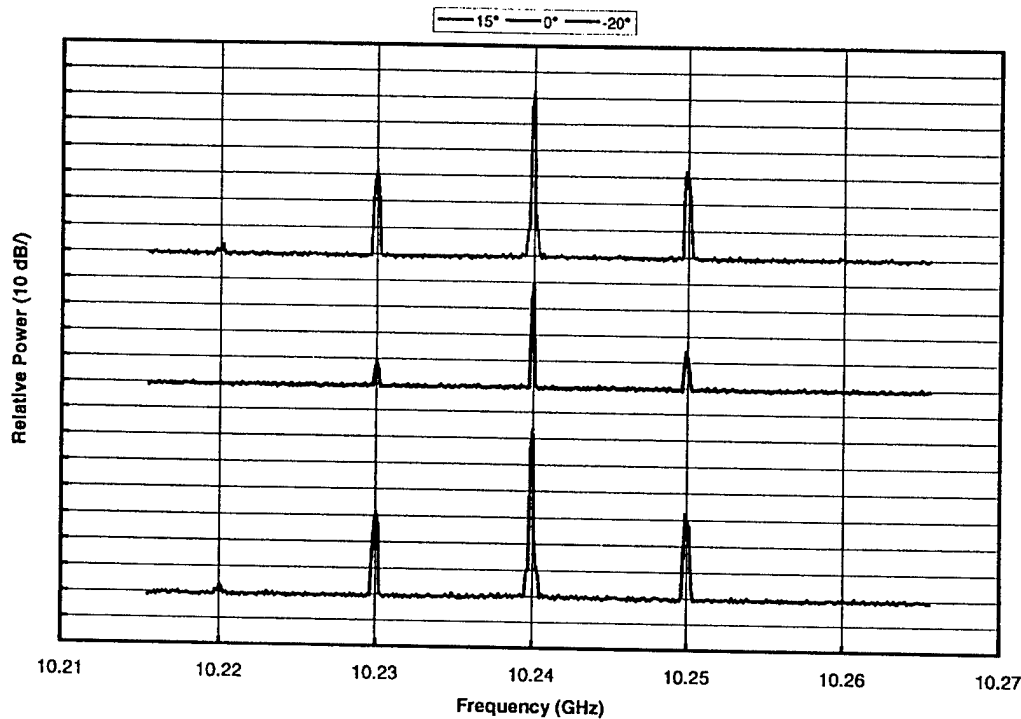
Fig. 11. Detected spectra at different angles with a modulation on the pump signal. This demonstrates that retro-directivity can also be used to communicate between a conjugator and its illuminating sources. The top curve and bottom curve represent the two conjugate beams. The leakage signal between the conjugate beams is about 20 dB smaller than the conjugate beams. These spectra have been moved in the vertical direction for easier comparison.

constructed using discrete components, as done in this paper. As we have demonstrated, optical interconnections can solve the 2ω pump signal distribution problem for large two-dimensional arrays. However, in the millimeter-wave regime, monolithic design will be needed in order to satisfy the small $\lambda/2$ spacing requirement. Using high-speed photodetectors and mixing devices [15], [16] in conjunction with on-wafer polyimide optical waveguides [17], two-dimensional millimeter-wave phase-conjugate surfaces can be realized. Fig. 12 shows this concept.

To address the problem of amplified leakage signals coming out from our phase-conjugate elements, a two-stage mixing technique has been proposed [11]. To understand how it works, let us consider that the sampled incident signal has a phase factor of $\omega t - \varphi$. This incident signal will be mixed with a pump signal having a phase factor of Ωt, where $\omega < \Omega < 2\omega$ and this phase factor Ωt is the same for all elements. After the first-stage mixing, there will be four major components coming out from the mixer: $(\Omega-\omega)t+\varphi$, $(\Omega+\omega)t-\varphi$, $\omega t-\varphi$, and Ωt. The first term is the signal we want because of its reversed phase $+\varphi$. The second term is the sum frequency, and the last two terms are the leakage through the mixer. Since these four signals are at different frequencies if $\Omega \neq 2\omega$, a bandpass filter at $\Omega - \omega$ can be used to remove the three unwanted components. A second-stage mixing is needed because the signal carrying the conjugate phase is not yet at the incident frequency. To convert the $(\Omega-\omega)t+\varphi$ signal back to frequency ω, it is mixed with a second pump signal $(2\omega - \Omega)t$. Again, this pump signal has to be the same for all elements. As in
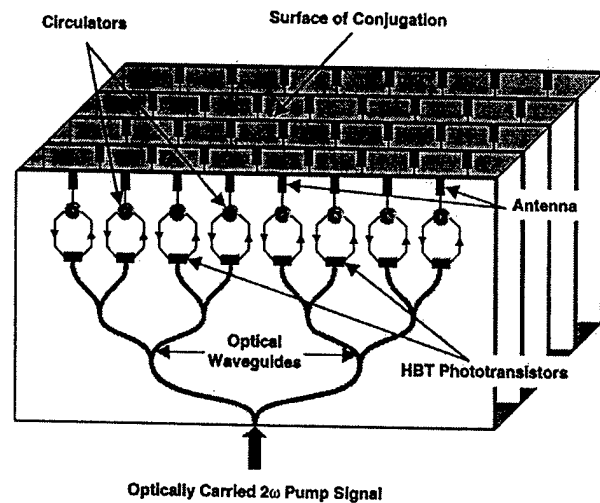

Fig. 12. Monolithic one-dimensional arrays forming a two-dimensional artificial nonlinear surface for generating three-dimensional microwave phase conjugation.

the first stage, four components will appear on the output port: $\omega t + \varphi$, $(2\Omega - 3\omega)t + \varphi$ or $(3\omega - 2\Omega)t - \varphi$, $(\Omega - \omega)t + \varphi$, and $(2\omega - \Omega)t$. Using a second bandpass filter at frequency ω, only the conjugate signal $\omega t + \varphi$ will be radiated back to form the conjugate beam. Therefore, this two-stage mixing scheme can eliminate the leakage problems caused by the single-mixer approach, and has the advantage of never dealing with frequencies as high as 2ω.

There are still other sources which can contribute to the output phase error, namely, the leakage of circulators and reflection of antenna elements. In this paper, we solved this problem by separating the sampling and radiating antennas. For a true three-dimensional wavefront reconstruction setup, sampling and radiating should occur at the same point and, therefore, only one antenna is desired. Both circulator leakage and antenna reflection can be reduced to below 30 dB if they are specially designed for a specific narrow band. Also, for pulsed applications, wide-band operations can still be realized if the sampled signal and conjugate signal can be separated in time. This can be achieved by delaying the conjugate signal in a long optical fiber during the sampling period. During the radiating period, the mixer input is blocked and, therefore, the reflected conjugate signal will not enter the mixer.

In this paper, we have concentrated on generating phase conjugation using electronic-mixing arrays. This technique can also be extended to other nonlinear optics analogies. For example, by replacing the 2ω pump signal feeding the mixer in a phase-conjugate element with the sampled ω signal, the element can generate 2ω, therefore, acting as a second-harmonic element. This type of electronic mixing arrays can perform free-space second-harmonic generation. Using different configurations for the basic elements, these electronic-mixing microwave arrays can provide very high effective $\chi^{(2)}$ or $\chi^{(3)}$, which are not available in any natural material.

Due to the retro-directivity and automatic phase correction properties, microwave and millimeter-wave phase conjugation is useful in applications requiring automatic pointing and tracking and phase aberration corrections. We have also demonstrated that information can be transmitted in phase-conjugate signals without prior knowledge of where the targets are. Therefore, microwave and millimeter phase conjugation can be very useful for novel communications systems such as satellite links on moving vehicles and deep-space transponder applications. Another interesting application is to use these structures to combine the output power from many elements to form high-power beams with excellent mode quality.

In this paper, we have developed and demonstrated a new approach to achieve phase conjugation in the microwave and millimeter-wave regime. We have obtained similar results for both electrical and optical-interconnection techniques. The proof of two-dimensional free-space phase conjugation has been obtained by direct measurements of the output electric-field magnitude distribution at 10.24 GHz. Using a distorting medium and two sources, retro-directivity and automatic phase correction have been directly observed on the electric-field wavefronts. The capability of data communication using phase conjugation has also been validated by transmitting a 10-MHz modulated signal back to the two sources illuminating the conjugator. Furthermore, the conjugate signal has shown a 10-dB power gain, which is desired for communications applications. In the near future, we foresee many nonlinear optical techniques being extended to the microwave and millimeter-wave regime and also new microwave and millimeter-wave applications being developed using these electronic mixing arrays.

REFERENCES

[1] A. Yariv and P. Yeh, *Optical Waves in Crystals*. New York: Wiley, 1984.

[2] B. Ya. Zel'dovich, N. F. Pilepetsky, and V. V. Shkunov, *Principles of Phase Conjugation*. Berlin, Germany: Springer-Verlag, 1985.

[3] Y. I. Kruzhilin, "Self-adjusting laser-target system for laser fusion," *Sov. J. Quantum Electron*, vol. 8, no. 3, pp. 359–363, 1978.

[4] D. M. Pepper and A. Yariv, "Compensation for phase distortions in nonlinear media by phase conjugation," *Opt. Lett.*, vol. 5, no. 2, pp. 59–60, 1980.

[5] J. A. Yeung, D. Fekete, D. M. Pepper, and A. Yariv, "A theoretical and experimental investigation of the modes of optical resonators with phase-conjugate mirrors," *IEEE J. Quantum Electron.*, vol. QE-15, pp. 1180–1188, Oct. 1979.

[6] R. Shih, "Microwave phase conjugation in an artificial Kerr medium," Ph.D. dissertation, Dept. Elect. Eng., Univ. California at Los Angeles, Los Angeles, CA, 1991.

[7] R. Shih, H. R. Fetterman, W. W. Ho, R. McGraw, *et al.*, "Microwave phase conjugation in a liquid suspension of elongated microparticles," *Phys. Rev. Lett.*, vol. 65, no. 5, pp. 579–582, 1990.

[8] B. Tsap, K. S. J. Pister, and H. R. Fetterman, "MEMS orientational optomechanical media for microwave nonlinear applications," *IEEE Microwave Guided Wave Lett.*, vol. 6, pp. 432–434, Dec. 1996.

[9] _____, "Grating formation in orientational optomechanical media at microwave frequencies," *Appl. Phys. Lett.*, vol. 70, no. 18, pp. 2475–2477, 1997.

[10] C. C. Cutler, R. Kompfner, and L. C. Tillotson, "A self-steering array repeater," *Bell Syst. Tech. J.*, vol. 42, pp. 2013–2032, 1963.

[11] E. L. Gruenberg, H. P. Raabe, and C. T. Tsitsera, "Self-directional microwave communication system," *IBM J. Res. Develop.*, vol. 18, no. 2, pp. 149–163, 1974.

[12] C. Pobanz and T. Itoh, "A conformal retrodirective array for radar applications using a heterodyne phased scattering element," in *Proc. IEEE MTT-S Int. Microwave Symp. Dig.*, vol. 2, Orlando, FL, May 1995, pp. 905–908.

[13] S. L. Karode and V. F. Fusco, "Novel retrodirective beam formation techniques," in *Proc. 27th Microwave Conf.*, vol. 1, Jerusalem, Israel, Sept. 1997, pp. 81–85.

[14] B. D. Steinberg, *Principles of Aperture and Array System Design: Including Random and Adaptive Arrays*. New York: Wiley, 1976.

[15] D. C. Scott, D. V. Plant, and H. R. Fetterman, "60 GHz sources using optically driven heterojunction bipolar transistors," *Appl. Phys. Lett.*, vol. 61, no. 1, pp. 1–3, 1992.

[16] D. Bhattacharya, P. S. Bal, H. R. Fetterman, and D. Streit, "Optical mixing in epitaxial lift-off pseudomorphic HEMT's," *IEEE Photon. Tech. Lett.*, vol. 7, pp. 1171–1173, Oct. 1995.

[17] D. P. Prakash, D. V. Plant, H. R. Fetterman, and B. Jalali, "Optically integrated millimeter wave systems," *Proc. SPIE—Int. Soc. Opt. Eng.* vol. 2153, pp. 101–110, 1994.

Yian Chang received the Ph.D. degree in physics from the University of California at Los Angeles (UCLA), in 1996.

He is currently working at the Center for High Frequency Electronics, UCLA, as a Post-Doctoral Researcher, where his work has concentrated on the areas of microwave and millimeter phase conjugation and optically controlled phased-array radars.

Harold R. Fetterman (SM'81–F'90) received the Ph.D. degree from Cornell University, Ithaca, NY, in 1967.

He is currently a Professor in the Department of Electrical Engineering, University of California at Los Angeles (UCLA). He joined UCLA after 14 years at the Lincoln Laboratory, Massachusetts Institute of Technology (MIT), Cambridge, where he was active in submillimeter-wave/millimeter-wave detectors and source programs. He successfully developed heterodyne receivers and solid-state sources with applications in plasma diagnostics, remote sensing, and radar modeling. Since joining UCLA, he has concentrated on millimeter-wave GaAs and InP devices and the optical control and testing of high-frequency systems.

Dr. Fetterman is a fellow of the Optical Society of America (OSA).

Steve K. Panaretos, photograph and biography not available at the time of publication.

Irwin L. Newberg (S'53–A'54–M'59–LM'95) received the B.S. degree in electrical engineering from the University of Cincinnati, Cincinnati, OH, in 1953, and the M.S. degree from the Massachusetts Institute of Technology (MIT), Cambridge, in 1959.

Since 1965, he has been with the Hughes Aircraft Company (now Raytheon Systems Company), Los Angeles, CA, where he has been involved in radar-system engineering and, for the past ten years, in the application of high-speed digital and microwave fiber-optic links for radar systems.

Millimeter-wave phase conjugation using artificial nonlinear surfaces

Yian Chang[a)] and Harold R. Fetterman
Electrical Engineering Department, University of California, Los Angeles, California 90095

Irwin L. Newberg and Steve K. Panaretos
Hughes Aircraft Company, Los Angeles, California 90009-2426

An artificial nonlinear surface has been developed using antenna-coupled mixers with optical interconnects for microwave and millimeter-wave phase conjugation. Prototype one-dimensional arrays have been constructed and have been used to demonstrate two-dimensional free-space phase conjugation at 10.24 GHz. The phase conjugation properties have been observed and verified by directly measuring the electric-field distribution of the conjugate wave under various conditions. Furthermore, the experiments have shown amplified conjugate wave power up to ten times of that of the incoming wave. This amplifying ability demonstrates the potential of such surfaces to be used in novel communications applications. © *1998 American Institute of Physics.*
[S0003-6951(98)02106-8]

Since its first demonstration, optical phase conjugation has been studied intensively. Most of this interest can be traced to potential applications in image processing and in dynamic compensation for distortion. This technique utilizes the nonlinear susceptibility of a medium to reverse the phase factor of an incoming wave. The phase-conjugate wave propagates backward and has the same wave fronts as that of the incoming wave.[1] This unique property of phase-conjugated waves is useful in many novel applications including automatic pointing and tracking, phase aberration corrections, and phase-conjugate resonators. To date, most of the phase conjugation development has been concentrated in the optical (visible and IR) regime. Efforts to extend this technique to microwave and millimeter wave (MMW) have encountered severe difficulties due to the small nonlinearity of materials and the low-power densities available at these wavelengths. In the search for alternative media suitable for use in MMW nonlinear optics, artificial media were found to have much larger nonlinearities than that of crystals. Using shaped microparticle suspensions[2] and MEMS structures,[3] volume grating formation for microwave phase conjugation has been demonstrated using degenerate four-wave mixing techniques.

During the past decade, quasioptical approaches have been studied intensively for MMW generation, amplification, and other applications.[4–6] In this current study, the basic idea is to use quasioptical techniques to replace the weak microwave nonlinearities of electron distributions in a crystal with the strong nonlinear *I–V* response of *P–N* junctions. This method effectively creates a surface with a strong nonlinear susceptibility $\chi^{(2)}$, which can then be used to generate phase-conjugate waves using a three-wave mixing technique. Because this process takes place entirely on the surface, phase matching is not required. We have effectively demonstrated an artificial nonlinear surface exhibiting two-dimensional free-space phase conjugation at 10.24 GHz by using an array of antenna-coupled mixers synchronized with optical interconnects.

It has been proven theoretically that if a wave is conjugate to another at a certain plane, they will conjugate to each other everywhere.[7] In other words, phase conjugation can be achieved using a strong nonlinear surface instead of a volume of weak nonlinear material. To realize this theory, we turn to the nonlinear *I–V* characteristic of diodes. Microwave circuits that combine antennas and microwave mixers can effectively replace the nonlinear dipoles of a medium. The idea is to "sample" the incident wave at different positions of the wave front with an array of antennas and then generate phase-conjugate currents using microwave mixers. These currents will then excite a phase-conjugate field at each sampling point. If the sampling is dense enough, the combined field of all elements will be the phase-conjugate wave of the incident beam. This sampling concept was proposed in the 1960's, but due to the lack of modern semiconductor and optical technologies, researchers did not have a practical way to implement the concept.[8] To understand how the conjugate signal can be generated at each element using microwave circuitry, let us consider the incident electric field at the *j*th element:

$$\mathbf{E}=\mathbf{A}(\mathbf{r}_j)e^{i(\omega t-\varphi_j)}+\text{c.c.}, \tag{1}$$

where

$$\varphi_j=\mathbf{k}\cdot\mathbf{r}_j+\varphi(\mathbf{r}_j). \tag{2}$$

The signal picked up by the antenna and then sent to the rf port of the mixer can be written as

$$V_{j1}\propto A(r_j)e^{i(\omega t-\varphi_j)}+\text{c.c.} \tag{3}$$

Now consider a 2ω signal delivered to the LO port of the mixer given by

$$V_{j2}=Ce^{2i\omega t}+\text{c.c.} \tag{4}$$

This 2ω pump signal has to be delivered to all elements at the same amplitude and phase; otherwise, the mixed output will contain a term other than V_{j1} that depends on *j*. If this ever happens, the sum of the excited field at each element will be distorted and will not form the conjugate beam. Optical interconnection is the crucial technology implemented
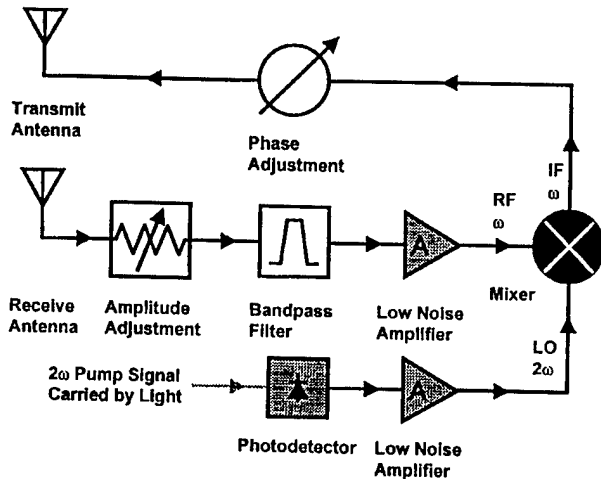
[a)]Electronic mail: ychang@ucla.edu

745   © 1998 American Institute of Physics

FIG. 1. The configuration of a phase-conjugate element used in this study.

to carry this 2ω microwave pump signal in phase to all mixing elements because of its low loss, light weight, and small size compared to microwave components. Using difference frequency generation in a mixer, the if output current can be written as

$$I_C \propto e^{2i\omega t} \times e^{-i(\omega t - \varphi_j)} = e^{i(\omega t + \varphi_j)}. \quad (5)$$

This current component has the conjugate phase $+\varphi_j$ instead of the input phase $-\varphi_j$. Therefore, when it is delivered to the antenna, it will excite the conjugate field at r_j:

$$E_{Cj}(r_j) \propto A(r_j) e^{i(\omega t + \varphi_j)} + \text{c.c.} \quad (6)$$

When the sampling spacing is less than $\lambda/2$, the combined field $E_C = \Sigma_j E_{Cj}(r)$ forms the phase-conjugate wave on the sampling surface and, therefore, everywhere. Computer simulations have shown that the quality of the conjugate wave is limited by the size of the conjugation surface, not the element spacing, as long as the element spacing is less than $\lambda/2$.

To implement the above-mentioned concepts, we have built an eight-element one-dimensional array with optical interconnects to deliver the 2ω pump signals. Figure 1 shows the configuration of each element. Since we had planned to demonstrate two-dimensional (in the xy plane) free-space phase conjugation using a one-dimensional array, we have chosen to separate the transmit and the receive antennas in the z direction for simplicity. This means the sampling of the incident field and the excitation of the conjugate field happen at the same (x,y) coordinates but a slightly different z coordinate. This small shift in the z direction will only disturb the electric-field distribution on the xy plane to a negligible level. To avoid this small spatial shift of the conjugate field, a circulator can be used to allow a single antenna to perform both transmitting and receiving functions at each element. In this case, however, the return loss of the antenna has to be much larger than the gain provided by the element at the operating frequency in order to prevent oscillation and distortion.

Because the incoming wave (rf) and the conjugate wave (if) have the same frequency, filters cannot be used to separate these two signals. In order to achieve maximum isolation between the rf and the if signals, a triple-balanced mixer

was used in the configuration shown in Fig. 1. An alternative way to accomplish signal isolation is to use a two-stage mixing technique. In this method, the undesired incoming frequency can be filtered out by a bandpass filter after the first stage mixing. This filtered signal can then be mixed in the second stage to produce the final conjugate signal. Again, a second bandpass filter can filter out any undesired leakage signals. This four-wave mixing technique can achieve higher isolation between the incoming signal and the conjugate signal at the cost of an addition pump source for each element.

In Fig. 1, a filter is used to reduce the noise and to limit the gain of the element to a narrow band to prevent two-tone oscillations. Furthermore, one phase adjustment and one amplitude adjustment device are used at each element to compensate the differences between the amplifiers and the mixers of different elements. These adjustments can be eliminated by fabricating matched amplifiers and mixers. In this demonstration, the rf frequency was set at 10.24 GHz. The element spacing of the antenna arrays was 0.467λ and the spacing between the transmit and receive arrays was 0.478λ. A diode-pumped Nd:YAG laser was used as the light source. The optical wavelength was 1319 nm, with a linewidth ≤ 5 kHz. This wavelength is chosen to minimize the dispersion in optical fiber systems. In this demonstration, it is not an important issue because of the relatively short propagation distances. However, to be able to extend this technique into large surfaces and/or millimeter-wave frequencies, minimized dispersion will be a crucial factor.

The laser light was directed into a LiNbO$_3$ Mach–Zehnder optical modular using a polarization preserving fiber and was modulated by the 2ω (20.48 GHz) signal. This optically carried 2ω pump signal is delivered to each element using optical fibers. It is then extracted by a photodetector for use as the LO signal for mixing. Using a digital sampling oscilloscope (DSO) to display the conjugate signals, the amplitudes of all phase-conjugate elements were matched to within $\pm 2\%$ and the phases matched to within ± 0.2 ps (0.2%).

For testing of the phase conjugation properties, two transmitting horns were aimed at the one-dimensional nonlinear surface inside an anechoic chamber. A receiving horn was mounted on a computer-controlled rotation stage, which allowed the receiving horn to rotate from $-30°$ to $+30°$. The rotation stage was then mounted on a translation stage to allow for changing the distance to the nonlinear surface. The receiving horn was arranged slightly below the transmitting horns to permit free movement without blocking the incoming beams. The received signal was amplified and then displayed on a DSO. By comparing the received signal to a reference signal using a computer, the amplitude and phase of the electric field at the receiving horn position can be measured relative to the transmitted signal. The conjugate electric-field distribution in the xy plane was measured by rotating the receiving horn from $-30°$ to $+30°$ with $1°$ steps and by changing the distance from 45 to 55 cm with 0.5 cm steps. A typical result is shown in Fig. 2. In this case, the transmitting horns were located at $+15°$ and $-20°$ with distances of 60 cm from the nonlinear surface, as marked by the black dots. The nonlinear surface was located at the left of each contour plot.
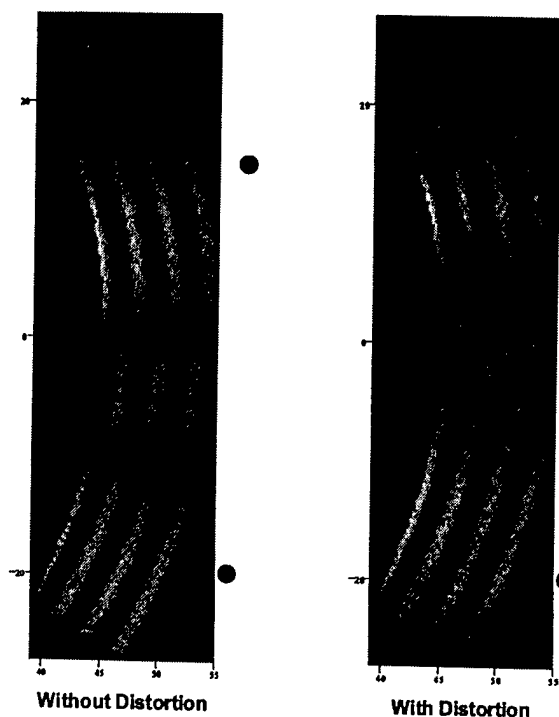
Appl. Phys. Lett., Vol. 72, No. 6, 9 February 1998

Chang *et al.*   747

Without Distortion   **With Distortion**

FIG. 2. The contour plots of the phase-conjugate electric field of two sources at $+15°$ and $-20°$. They demonstrate multiple-source retrodirectivity and automatic phase correction when a distorting medium is inserted in front of the conjugator. The four black dots represent the transmitting horns and the brighter color represents higher field in the plots. Leakage signals, down by about 10 dB, also appear adjacent to the conjugate signals.

The brightness of the contour plots indicates the magnitude of the electrical field at a given time at a given position, with white for high field and black for low field. The first plot, marked as without distortion, was obtained without anything in the beam paths. It exhibits multiple-source retrodirectivity, as indicated by the wave fronts traveling back to the sources. Note that mixer leakage signals can also be seen adjacent to the two main conjugate beams. The leakage signals were about 10 dB lower than the conjugate signals. As mentioned earlier, this leakage can be minimized by using a two-stage mixing technique. The conjugate beams also acquired a 10 dB gain from the amplifiers of the nonlinear surface. In the same plot, however, the conjugate wave does not show the effect of focusing back to the sources, which is expected in a true wave-front reconstruction. This is a result of diffraction distortion caused by the small size of the nonlinear surface. Our computer simulations have predicted this for the eight-element array. Simulations have also shown that a clear focusing effect can be observed for a 40-element array with the same element spacing.

To demonstrate the multiple-source retrodirectivity indeed originated from phase conjugation, not from corner reflections or any other means, a dielectric distorting material was inserted in front of the phase conjugator. The resulted field distribution is shown in the second contour plot. By comparing the fringes in the two plots, we clearly observe the two main phase-conjugate beams maintain the same phases with or without the distorting medium, as expected from a phase-conjugate wave. At the same time, the leakage
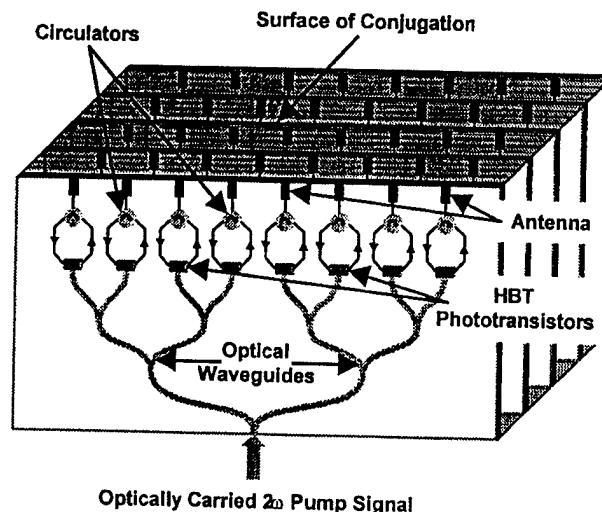

FIG. 3. Monolithic one-dimensional arrays forming a two-dimensional artificial nonlinear microwave surface for generating three-dimensional microwave phase conjugation.

signals are completely distorted due to the fact that they travel through the distorting medium twice without any phase inversion.

In summary, we have demonstrated two-dimensional free-space phase conjugation at 10.24 GHz with diffraction-limited results using an optically injected artificial nonlinear microwave array. By extending this one-dimensional array into a two-dimensional surface, as shown in Fig. 3, complete three-dimensional wave-front reconstruction can be realized at MMW frequencies. Other types of artificial media can also be created to provide large $\chi^{(2)}$ and $\chi^{(3)}$ on single surfaces by changing the basic elementary configuration. Using modern monolithic fabrication techniques, we foresee many nonlinear optical processes being extended to the MMW regime and also MMW applications being developed using these artificial nonlinear surfaces.

[1] B. Ya. Zel'dovich, N. F. Pilepetsky, and V. V. Shkunov, *Principles of Phase Conjugation* (Springer, New York, 1985).

[2] R. Shih, H. R. Fetterman, W. W. Ho, R. McGraw, D. Rogovin, and B. Bobbs, Phys. Rev. Lett. 5, 579 (1990).

[3] B. Tsap, K. J. Pister, and H. R. Fetterman, Appl. Phys. Lett. 18, 2475 (1997).

[4] E. A. Sovero, M. Kim, R. M. Weikle II, D. S. Deakin, W. J. Ho, J. A. Higgins, and D. B. Rutledge, *14th Annual IEEE Gallium Arsenide Integrated Circuit Symposium Technical Digest*, FL, 1992 (IEEE, New York, 1992), p. 305.

[5] J. Hubert, J. Schoenberg, and Z. B. Popovic, *Proceedings of 1995 IEEE MTT-S International Microwave Symposium*, FL, 1995, edited by L. Kirby (IEEE, New York, 1995), p. 585.

[6] S. Kawasaki and T. Itoh, IEEE Trans. Microwave Theory Tech. 4, 717 (1993).

[7] R. Saxena and P. Yeh, *Optical Phase Conjugation*, edited by M. Gower and D. Proch (Springer, New York, 1994), p. 8.

[8] C. C. Cutler, R. Kompfner, and L. C. Tillotson, Bell Syst. Tech. J. 42, 2013 (1963).

MEMS Orientational Optomechanical Media for Microwave Nonlinear Applications

B. Tsap, K. S. J. Pister, and H. R. Fetterman

Abstract— The fabrication and testing of orientational optomechanical media suitable for microwave phase conjugation is described. It consists of metal-coated dielectric elongated beams 1 mm × 100 μm × 10 μm suspended by nonconductive torsional springs attached to a microwave transparent frame. Rotation of single elements, in a polarized electromagnetic field at 15 GHz, was measured and found to be in a good agreement with theory. This first experimental implementation of using microelectromechanical structures (MEMS) for nonlinear microwave devices demonstrates the potential of an entirely new class of devices.

I. INTRODUCTION

PHASE CONJUGATION at microwave frequencies has attracted much attention in recent years [1]–[3]. Optical birefringence [2] and phase conjugation via degenerate four-wave mixing (DFWM) [3] using a mineral oil–heptane suspension of shaped carbon microfibers at centimeter wavelength has been demonstrated. To obtain a number of practical advantages over liquid suspensions of shaped microparticles for device applications, a new class of artificial dielectric media was suggested [1], [4]. These media consist of three-dimensional (3-D) arrays of electrically small, anisotropic particles that are mechanically supported and free to rotate, under the action of electromagnetically induced torques, into preferred directions set by the net polarization vector of the incident radiation. Rotation of the particles changes the effective index of refraction of the medium and gives rise to orientational index gratings that can be used for active optical processes. These particle arrays are referred to as orientational optomechanical media and have unique dielectric and dynamic properties such as reasonable optical response times, overall thermal, optical, and mechanical stability, and control. They are therefore an unusually promising microelectromechanical structures (MEMS) candidate for active optical applications at microwave and millimeter frequencies.

In this letter, we report fabrication and testing of the first prototype of an optomechanical medium consisted of 1 mm × 100 μm × 10 μm polyimide beams covered with 0.2 μm of aluminum and supported by two nonconductive torsional springs attached to a 10-μm-thick dielectric frame. Our MEMS device demonstration combines the micromachining fabrication techniques with the concept of active millimeter-wave nonlinear devices. As a next step, microwave

phase conjugation via DFWM in 3-D arrays of mechanically supported metal-coated rods will be measured.

II. DESIGN AND FABRICATION

A particle with polarizability tensor $\alpha(\hat{\Omega})$, where $\hat{\Omega} \equiv (\theta, \phi)$ are the orientational angles of its symmetry axis, in the electromagnetic field $\vec{E}(\vec{r}, t)$ acquires a dipole moment $\vec{p} = \alpha(\hat{\Omega}) \cdot \vec{E}$. This then couples back to the radiation field giving rise to an electrostrictive potential $U(\vec{r}, \hat{\Omega}; t)$. Associated with $U(\vec{r}, \hat{\Omega}; t)$ is electrostrictive force $\vec{F}(\vec{r}, \hat{\Omega}; t)$ and electrostrictive torque $\vec{\Gamma}(\vec{r}, \hat{\Omega}; t)$. If the particles are fixed in space, we can neglect electrostrictive forces that tend to change the particles' density distribution. The maximum field induced torque can be expressed as $|\vec{\Gamma}| = (4\pi/c)\beta I$, where β is the asymmetric component of particle polarizability, I is the field intensity, and c is the speed of light. Nonabsorbing, symmetrical microellipsoids are characterized by polarizability components α_{ll} parallel to the symmetry axis and $\alpha_\perp$ in any direction perpendicular to this axis. It can be shown that the asymmetric polarizability β can be expressed in terms of the components of the tensor $\alpha(\hat{\Omega})$

$$\alpha_{ll} = \frac{V}{4\pi} \frac{\epsilon - 1}{1 + \frac{3}{8\pi}(\epsilon - 1)A_1(a, b)}$$

and

$$\alpha_\perp = \frac{V}{4\pi} \frac{\epsilon - 1}{1 + \frac{3}{8\pi}(\epsilon - 1)A_2(a, b)}$$

where V is the ellipsoid's volume, ϵ is the dielectric constant, and A_1 and A_2 are depolarization coefficients [5].

For metal or metal-coated ellipsoids, the asymmetric component of the particle's polarizability is

$$\beta = \alpha_{ll} - \alpha_\perp = abc\left(\frac{1}{A_1} - \frac{1}{A_2}\right)$$

where a, b, c are the major ellipsoid semiaxises. Field-induced torques can therefore be optimized choosing appropriate shaped ellipsoid particles. For fabricated beams of dimensions 1 mm × 100 μm × 10 μm the calculated asymmetric component of polarizability was $\beta = 4.68 \times 10^{-5}$ cm^{-3}.

For an optomechanical medium composed of an array of spring-supported beams, we must take into account the twisting torque that the springs generate as the beams rotate. The torque Γ_S is given by $\Gamma_S = (J_S G/L)\Delta$, where J_S is the polar moment of inertia of the spring with the length L, and spring shear modulus G with Δ the angle of rotation.
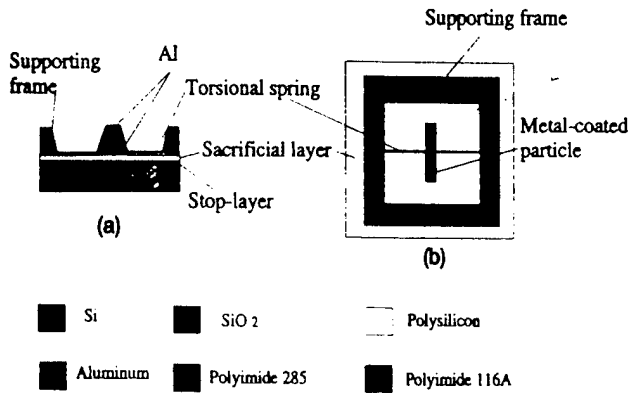
Fig. 1. (a) Cross section and (b) top views of a single rotating element fabricated by standard micromachining techniques.

$$\Delta = 1/2(\Theta_1 - \Theta_2)$$

$$\Theta_2 = \sin^{-1}(b/(x^2 + b^2)^{1/2})$$

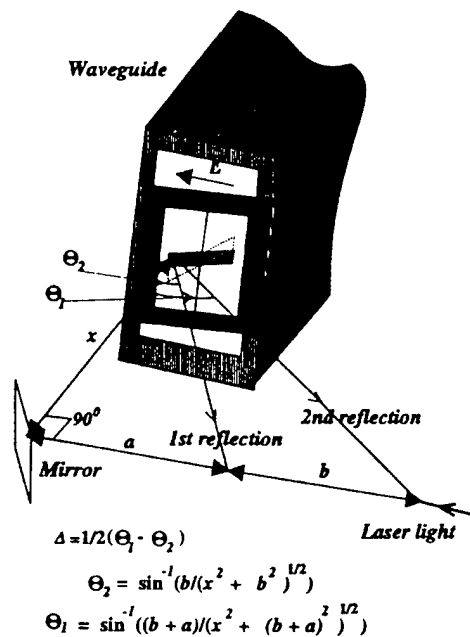$$\Theta_1 = \sin^{-1}((b + a)/(x^2 + (b + a)^2)^{1/2})$$

Fig. 2. Optical part of experimental setup for measurement of interaction of optomechanical medium with microwave radiation.

Assuming field-induced torques of about 10^{-13} Nm and a desired rotation of 90°, this requires torsional spring constant $k = \Gamma_S/\Delta$ of approximately 6×10^{-15} Nm deg^{-1}. Such a small spring constant eliminates from consideration such attractive fabrication materials as polysilicon and SiO$_2$. We consequently chose polyimide for our applications because of its low shear modulus ~ 1 GPa and relative ease of processing. Moreover, it allows us to fabricate nonconducting springs and supporting frames of sufficiently different thicknesses using commercially available Probimide 100 and 200 series. Fig. 1 shows a cross section and a top view of a single rotating element. Two by two square inch arrays with 100 equally spaced elements were fabricated on the top of 4-in. silicon wafer with a sacrificial polysilicon layer and low temperature oxide used as a stop layer with standard photolithography techniques. To release the fabricated structures xenon difluoride (XeF$_2$), a dry isotropic etchant [6] was used to circumvent the liquid surface tension forces present during conventional wet
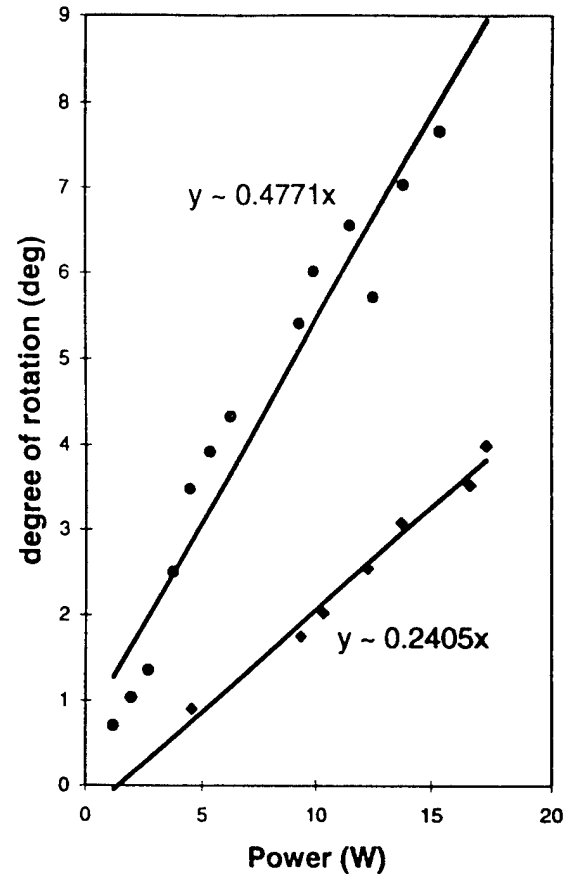

Fig. 3. Degree of rotation of two metal-coated dielectric beams each suspended by two torsional springs with the width of 4 μm (top line) and 7 μm (lower line), respectively. Solid lines are least square approximation for linear dependence $\Delta(P)$.

etching. Finally, fabricated structures were glued to a Rexolite frame, which later will allow for 3-D stacking. As a result, we fabricated arrays of dielectric beams covered with aluminum with dimensions 1 mm $\times$ 100 μm $\times$ 10 μm each supported by 1-mm-long, 0.6-μm-thick torsional springs. To vary the spring constant k as well as its mechanical strength, springs with widths between 4 μm and 10 μm were fabricated. The torsional spring constant of the most compliant spring was calculated to be 1.5×10^{-13} Nm deg^{-1}.

III. MEASUREMENTS

In our first experiments the response of fabricated arrays of mechanically suspended metal-coated particles to microwave radiation at 15 GHz was measured. A TWT amplifier with output power up to 20 W in Ku-band was used to illuminate the rotating elements. The light of a He-Ne laser was focused to a spot size less than 100 μm on the side of a particle, and the reflection was directly observed with a video camera. The optical part of the setup (Fig. 2) allowed for the measurements of the rotation of a single element resulting from electrostrictive torques produced by the interaction of the orienting beam with electromagnetic radiation.

Fig. 3 shows the measured degree of rotation of 1 mm $\times$ 100 μm $\times$ 10 μm aluminum coated dielectric beam

suspended by two torsional polyimide springs. The width of the strings was 4 μm and 7 μm. respectively. Elements were placed very close to the edge of the microwave waveguide to maximize the intensity of the field. The intensity is assumed to be $I = P/S$, where P is measured output power and S is cross-sectional area of the waveguide. The rotation of the beam versus intensity of the electromagnetic field is linear. We observed no hysteresis in the beam's rotation with several consecutive changes in the field magnitude. The ratio of the measured two spring constants is $k_1/k_2 \approx 1.98$. which is fairly close to theoretical (geometry based) value of 1.87. The experimental value of a spring constant for 4-μm- and 7-μm-wide torsional springs was found to be 3.28×10^{-14} Nm deg^{-1} and 6.51×10^{-14} Nm deg^{-1}, respectively, which are four times less than our theoretically calculated values. This fact reflects an underestimate of the asymmetric part of beams polarizability. In our calculations we assumed them to be of the shape of the ellipsoid of revolution whose volume is almost one half of the actual volume of the fabricated parallelepiped beams of the dimension $2a \times 2b \times 2c$.

IV. CONCLUSION

Two-dimensional arrays of elongated metal-coated dielectric rods each supported by nonconductive torsional springs were fabricated by micromachining techniques. Rotation of the beams induced by microwave irradiation at 15 GHz was found to be in a good agreement with theoretical calculations of the response of such optomechanical medium to electromagnetic radiation. This is the first implementation of previously suggested orientational optomechanical media. This demonstrates the feasibility of a MEMS approach, the use of microelectromechanical structures, to generate an entirely new class of nonlinear microwave and millimeter-wave devices. A stacked 3-D array is now being constructed for use at Ku-band. As a next step, fabricated arrays will be used in phase conjugation experiments via degenerate four-wave mixing.

REFERENCES

[1] D. Rogovin and T. P. Shen, "Orientational optomechanical media for microwave applications." *J. Appl. Phys.*, vol. 71, no. 10, pp. 5281–5283, 1992.

[2] B. Bobbs, R. Shih, H. Fetterman. and W. Ho, "Nonlinear microwave susceptibility measurements of an artificial Kerr medium." *Appl. Phys. Lett.*, vol. 52, no. 1, pp. 4–6, 1988.

[3] R. Shih, H. R. Fetterman, W. W. Ho, R. McGrow, D. Rogovin, and B. Bobbs, "Microwave phase conjugation in liquid suspensions of elongated microparticles." *Phys. Rev. Lett.*, vol. 65, no. 5, pp. 579–582, 1990.

[4] H. R. Fetterman, D. Rogovin, R. Shih, and B. Tsap, "Nonlinear microwave optics using microparticles," *Nonlinear Optics*, vol. 7, pp. 219–223, 1994.

[5] J. A. Osborn, "Demagnetizing factors of the general ellipsoid." *Phys. Rev.*, vol. 67, no. 11–12, pp. 351–357, 1945.

[6] F. I. Chang, R. Yeh, and G. Lin *et al.*, "Gas-phase silicon micromachining with xenon difluoride." in *SPIE 1995 Symp. Micromachining and Microfabrication*, Austin, TX, Oct. 24–25, 1995.

Grating formation in orientational optomechanical media at microwave frequencies

Boris Tsap, Kristofer J. Pister, and Harold R. Fetterman
Department of Electrical Engineering, University of California, Los Angeles, Los Angeles, California 90095

Orientational optomechanical media, consisting of three dimensional arrays of elongated metal coated dielectric beams suspended by torsional springs, was fabricated using microelectromechanical system (MEMS) technology. Response of a single rotating element to a polarized electromagnetic radiation was found to be in a good agreement with theory. Spatial grating formation in fabricated orientational optomechanical media was detected and measured under the influence of two orthogonally polarized electromagnetic fields at 15 GHz. This process demonstrates the feasibility of using optomechanical media for phase conjugation, via degenerate four-wave mixing, and for other nonlinear processes at microwave and millimeter wave frequencies. © *1997 American Institute of Physics.* [S0003-6951(97)00718-3]

In recent years optical birefringence[1] and phase conjugation via degenerate four-wave mixing (DFWM)[2] have been extended into centimeter and millimeter wavelength spectral regions. Liquid suspensions of shaped carbon microfibers were used in these initial experiments. To obtain a number of practical advantages for three-dimensional device applications a new class of artificial dielectric media was suggested.[3,4] These media consist of three-dimensional arrays of small, anisotropic mechanically supported particles. Particles are free to rotate, under the action of electromagnetically induced torques, into preferred directions set by the net polarization vector of the incident radiation. Rotation of the particles changes the effective index of refraction of the medium and creates orientational index gratings that can be used for active optical processes. These particle arrays have unique dielectric and dynamic properties such as reasonable optical response times, overall thermal, optical, and mechanical stability. They are therefore referred to as orientational optomechanical media. The implementation of micromachining techniques for fabrication of such arrays demonstrated the potential of an entirely new class of nonlinear microwave devices.[5] However, the relatively high twisting torque of the previously fabricated supporting springs confined rotation of the particles to small angles and would require very high power electromagnetic fields for practical applications. In this letter we report a considerable improvement in flexibility of the mechanical supports. This allows for the first observation of spatial grating formation in orientational optomechanical media fabricated with micromachining techniques (OMEM) under influence of two orthogonally polarized electromagnetic fields at 15 GHz.

An elongated particle with polarizability tensor $\alpha(\hat{\Omega})$, where $\hat{\Omega} \equiv (\theta, \phi)$ are the orientational angles of its symmetry axis, in the electromagnetic field $E(r,t)$ acquires a dipole moment $p = \alpha(\hat{\Omega})E$ which then couples back to the radiation field giving rise to an electrostrictive potential $U(r,\hat{\Omega};t)$. Associated with $U(r,\hat{\Omega};t)$ are the electrostrictive force $F(r,\hat{\Omega};t)$ and electrostrictive torque $\Gamma(r,\hat{\Omega};t)$. If the particles are fixed in space, we can neglect electrostrictive forces which tend to change the particles' density distribution. The field-induced torque tends to rotate the micropar-

ticles into a direction specified by the vector polarization of the electromagnetic field. If the particles are irradiated by a single, plane polarized electromagnetic beam, then they will tend to point in a given direction. For the media irradiated by more than one field, coherent interferences between the electromagnetic waves will give rise to a modulation of the preferred particle orientation. This produces a variation of the effective dielectric constant, which is an optical index grating, that can be utilized for optical phase conjugation.

For two linearly plane polarized degenerate microwave beams of equal amplitude oscillating at the frequency ω, the vector sum is denoted by

$$E(r,t) = \sum_{j=x,y} E_0 \, \hat{e}_j \, \exp[i(\omega t - k_j r)], \tag{1}$$

where $j = 1, 2, \hat{e}_j$ are the normalized polarization vectors, and k_j are the corresponding wave vectors. In this case the electrostrictive potential can be written in the form

$$U(r,\hat{Q}) = gK_{xy} \exp(iQr) + c.c, \tag{2}$$

where $Q = k_1 - k_2$, $g = \beta E_0^2/4kT$, and $K_{xy} = \hat{e}_x \overleftrightarrow{K} \hat{e}_y$, with β being the asymmetric part of particles polarizability and $\overleftrightarrow{K}$ being the orientational matrix.[6] The matrix element K_{xy} specifies the orientation of the microparticles with respect to the direction of polarization of electromagnetic radiation. For two electromagnetic waves polarized in the z direction the electrostrictive torque can be expressed as

$$|\Gamma| = \frac{1}{2} \beta E_0^2 \cos\left(\frac{2\pi}{\Lambda} y\right) \sin(2\theta). \tag{3}$$

Here, y is the coordinate along the direction defined by Q.

Due to the spatially varying potential [Eq. (2)], the microparticles distribution is perturbed by electrostrictive torques [Eq. (3)] in such a way that an orientational grating with spatial period $\Lambda \equiv 2\pi/|k_1 - k_2|$, is formed. For metal coated beams $\beta > 0$, and if we look along Q direction, the particles will first tend to align themselves parallel to the polarization axis. This trend continues until $y = \Lambda/4$ at which point the electrostrictive torques are zero and there is no preferred orientation for the particles. For $\Lambda/4 < y < 3\Lambda/4$, the particles tend to orient at right angles to the polarization
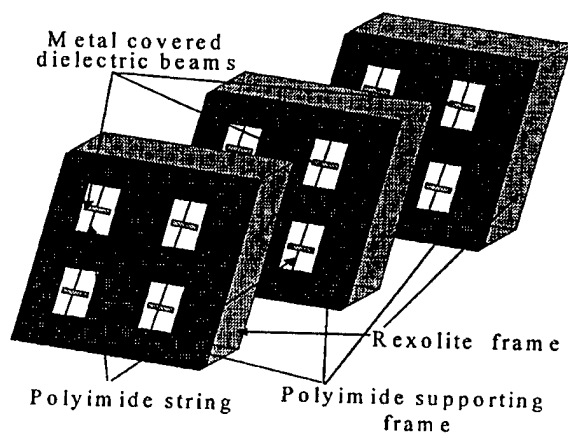
FIG. 1. Two-dimensional arrays of metal covered dielectric beams supported by torsional springs can form three-dimensional orientational optomechanical medium.
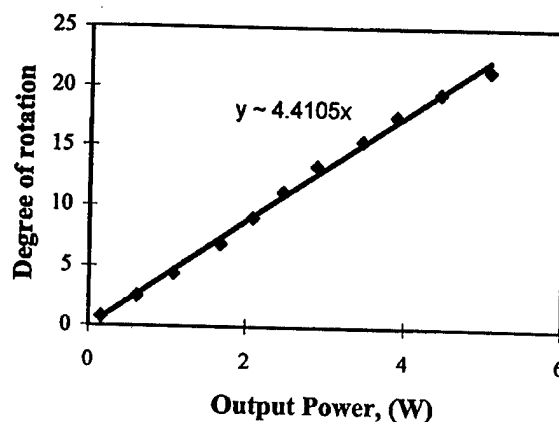

FIG. 2. Degree of rotation of a single microbeam in a linearly polarized electromagnetic field. Solid line is a least square approximation for linear dependence of the angle of rotation on power.

axis. At $y = 3\Lambda/4$, the electrostrictive torque is again zero and microparticles are randomly oriented. For fully degenerate mixing, $|\mathbf{k}_1| = |\mathbf{k}_2|$, and this grating has a period $\Lambda = \lambda/[2 \sin(\psi/2)]$, where ψ is an angle between $\mathbf{k}_1$ and $\mathbf{k}_2$.[7]

Two by two inch arrays of $1\,\text{mm} \times 100\,\mu\text{m} \times 10\,\mu\text{m}$ polyimide beams covered with 0.2-μm-thick aluminum and each supported by two $1\,\text{mm} \times 3\,\mu\text{m} \times 0.27\,\mu\text{m}$ polyimide strings were fabricated using micromachining techniques previously described.[5,8] The microbeams were equally spaced by 4 mm as shown in Fig. 1. Beams are free to reorient in the plane perpendicular to the supporting strings under the influence of electrostrictive torques due to the interaction of their asymmetric polarizability component with the electrostrictive potential of the electromagnetic field. These arrays can be easily stacked into three-dimensional structures for future use in free space phase conjugation experiments via degenerate four-wave mixing.

The asymmetric component of the beam's polarizability calculated according to Rogovin et al.[6] was $\beta = 4.68 \times 10^{-5}\,\text{cm}^{-3}$. In these calculations, microbeams were assumed to be of the form of an ellipsoid of revolution. The actual shape of the beams was close to that of a parallelepiped whose volume is about twice the volume of the ellipsoid of revolution with the same dimensions. This fact, and the difference in the value of the depolarization coefficients of a parallelepiped and an ellipsoid[7] used in our calculations, reflects an underestimate of the asymmetric part of the beam's polarizability.

First, in our experiments, the response of a single beam to microwave radiation at 15 GHz, in a setup described previously,[8] was measured. A focused laser light reflected from the rotated microbeam was observed with a video camera. Due to the geometry of the setup, the linear motion of the reflected light corresponds to the rotation of the beam. Figure 2 shows the degree of rotation of a $1\,\text{mm} \times 100\,\mu\text{m} \times 10\,\mu\text{m}$ aluminum coated dielectric beam supported by two torsional springs with dimensions $1\,\text{mm} \times 3\,\mu\text{m} \times 0.27\,\mu\text{m}$ as a function of radiated power. The torsional spring constant calculated from the slope of the straight line on Fig. 2 is $3.56 \times 10^{-15}\,\text{N m deg}^{-1}$. This value

is lower than the theoretically (geometry based) predicted spring constant. During the calculation we used a calibration procedure which took into account the underestimated value of the particle's asymmetric polarizability which leads to the reduced value of the experimentally extracted spring constant. The torsional spring constant of the fabricated springs corresponds to the ninefold decrease in the twisting torques compared with that of the most compliant springs previously reported.[6]

To create an orientational grating in fabricated OMEM two orthogonally polarized beams propagating in the perpendicular directions were used. They were formed by equally splitting the power of a traveling wave tube amplifier into two Ku-band waveguides. For two orthogonally polarized beams of equal magnitude propagating perpendicular to each other, $\psi/2 = 45°$, so that they form spatial grating with a period $\Lambda = \lambda/\sqrt{2}$. Figure 3, set of data no. 1, depicts a measured rotation of a single microbeam moved along the direction specified by $\mathbf{k}_1 - \mathbf{k}_2$. The degree of rotation of the beam represents a reorientation angle $\Delta\alpha$ between an initial orientation of the beam and its orientation set by the interacting
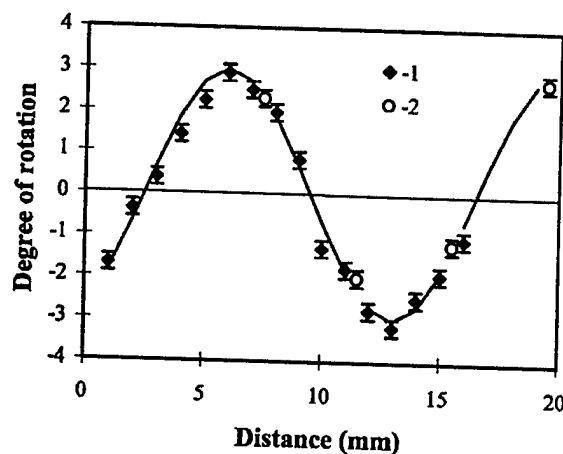

FIG. 3. Degree of rotation of microbeams in two orthogonally polarized fields at 15 GHz. Set No. 1 (■) for a single beam moved along $\mathbf{k}_1 - \mathbf{k}_2$ direction. Set no. 2 (O)-for an array of four beams separated by 4 mm each. Solid line is a theoretical curve calculated using Eq. (3).

Tsap, Pister, and Fetterman

electromagnetic fields. It displays a propensity of the beam to reorient in two opposite directions in accordance with the spatially varying electrostrictive torque. The amplitude of the beam rotation corresponds to the intensity of combined electromagnetic field of about 0.5 W cm^{-2}. It can be seen from Fig. 3 that the grating period Λ is about 14 mm which is very close to the theoretical value of 14.1 mm calculated for 15 GHz ($\lambda = 2$ cm). More importantly, Fig. 3, set of data no. 2, shows the reorientation from their initial direction for one of our arrays of four microbeams, fixed in space, each separated by the distance of 4 mm. Reorientation of the beams exhibits a spatial grating formation with the same period. To our knowledge this is the first direct experimental observation of orientational grating formation in nonlinear media consisting of arrays of shaped microparticles.

In conclusion, response of orientational optomechanical media fabricated by standard micromachining techniques to polarized electromagnetic radiation was measured. Spatial orientational grating formation in such a medium was observed. The measured grating period is found to be in good agreement with the theoretical predictions. Because the whole structure was fabricated on a single wafer by micromachining with very high uniformity, the initial orientation of the microbeams tends to be close to the plane of fabrication. It means that OMEM are intrinsically prealigned which can greatly improve microparticle grating formation times and index grating depth.[9] The next step, of course, is to use three-dimensional stacked arrays of OMEM to actually perform optical birefringence and phase conjugation via DFWM experiments at microwave frequencies.

[1] D. Rogovin and T. P. Shen, J. Appl. Phys. **71**, 5281 (1992).
[2] B. Bobbs, R. Shih, H. Fetterman, and W. Ho, Appl. Phys. Lett. **52**, 4 (1988).
[3] R. Shih, H. R. Fetterman, W. W. Ho, R. McGrow, D. Rogovin, and B. Bobbs, Phys. Rev. Lett. **65**, 579 (1990).
[4] H. R. Fetterman, D. Rogovin, R. Shih, and B. Tsap, Nonlinear Opt. **7**, 219 (1994).
[5] B. Tsap, K. S. J. Pister, and H. R. Fetterman, Microwave Guided Wave Lett. **6**, 432 (1996).
[6] D. Rogovin, Phys. Rev. A **32**, 2837 (1985).
[7] J. A. Osborn, Phys. Rev. **67**, 351 (1945).
[8] B. Tsap, K. S. J. Pister, and H. R. Fetterman, Proc. SPIE **2881**, 118 (1996).
[9] D. Rogovin and J. Scholl, Phys. Rev. A **43**, 4965 (1991).

Group Velocity Dispersion Cancellation and Additive Group Delays by Cascaded Fiber Bragg Gratings in Transmission

Shamino Wang, *Student Member, IEEE*, Hernan Erlig, *Student Member, IEEE*, Harold R. Fetterman, *Fellow, IEEE*, Eli Yablonovitch, *Fellow, IEEE*, Victor Grubsky, Dmitry S. Starodubov, and Jack Feinberg

Abstract—We have demonstrated that cascaded fiber Bragg gratings can provide delays of propagating pulses with minimal pulse reshaping. The grating pair used exhibited an overlap transmission region centered at 1551.05 nm, where both gratings contribute to the group delay and the group velocity dispersion (GVD) was canceled. Using wavelength tunable pulses spectrally sliced from a mode-locked fiber laser, the measurement was performed in the time domain with single picosecond resolution. Both gratings were 3 mm long and a maximum group delay of 15 ps was measured for the cascaded sequence. This compound grating configuration can be implemented as encoders and decoders in spread spectrum CDMA systems.

Index Terms—CDMA, dispersion compensation, fiber Bragg grating, group delay, wavelength slicing.

I. INTRODUCTION

UNIFORM fiber Bragg gratings, essentially one-dimensional photonic crystals, exhibit low group velocity and large dispersion near their stop bands. Therefore, delays can be achieved in transmission at band edge frequencies of uniform gratings, eliminating the need for circulators or couplers in conventional reflection schemes [1]. These delays are also coupled with dispersion, which severely limits their application to communication systems. In this letter we demonstrate that this dispersion can be effectively compensated for by transmission through opposite sides of grating pair stop bands, while both gratings contribute to the additive delay. Simulations have demonstrated the advantages afforded by gratings in long-haul fiber dispersion compensation [2], [3]. So far experimental investigations in this arena have been performed in the frequency domain [4] or in the time domain using a 50-GHz sampling oscilloscope [5]. Previously we reported single picosecond resolution time-domain measurements of group delay incurred by optical pulses propagating through a uniform grating [6]. We also demonstrated that the group delay was additive for nearly

identical cascaded gratings; however, the transmitted pulse was severely distorted [7].

In this letter we explore a fiber Bragg grating pair that provided a 15-ps group delay with compensated GVD in transmission. The gratings were 3 mm long each and spatially separated to avoid any coupling effect. The measured transmission spectrum is shown in Fig. 1. The grating pair exhibited bandgap centers at 1550.25 and 1552.10 nm with 3-dB bandwidths of 1.40 and 1.82 nm, respectively. The overlap transmission region had a 1551.05-nm central wavelength, a 0.5-nm 3-dB bandwidth, and −3-dB peak intensity transmission. A commercial simulation program was used to model the gratings with parameters chosen to match the measured transmission spectrum. The simulated group velocities are shown in Fig. 2. The constant effective group velocity from 1550.99 to 1551.10 nm in the overlap transmission region resulted from GVD and higher order dispersion compensation. This was confirmed experimentally in the time domain by the minimal pulse distortion.

II. EXPERIMENTAL SETUP

The output from a 1.55-μm mode-locked erbium-doped fiber laser exhibiting a 56-nm bandwidth was spectrally sliced [8] by an HP optical spectrum analyzer. The resulting 0.5-nm bandwidth pulses produced a ~16-ps full-width at half-maximum (FWHM) auto-correlation. Using a 3-dB coupler the pulse train was divided into the grating pair and into a reference fiber, subsequently recombined, and fed to an auto-correlator. The pulse train timing difference was then measured from the separation between the cross-correlation and auto-correlation traces, and the grating pair induced pulse distortion from the cross-correlation trace, by varying the center frequency of the 0.5-nm optical pulses. This experimental arrangement was detailed in [6] and [7].

III. RESULTS

The wavelengths at which the measurements were performed are labeled on the transmission spectrum. Point A was situated at 1545.00 nm where we expected no grating pair effect. E was at the center of the overlap transmission region. B and F were on opposite sides of the spectrum and had the same transmission as E. D produced the same delay as that of E. C was the spectral midpoint of B and D.

For some of these wavelengths the correlation traces are plotted in Fig. 3(a). The 52-ps separation between the cross-
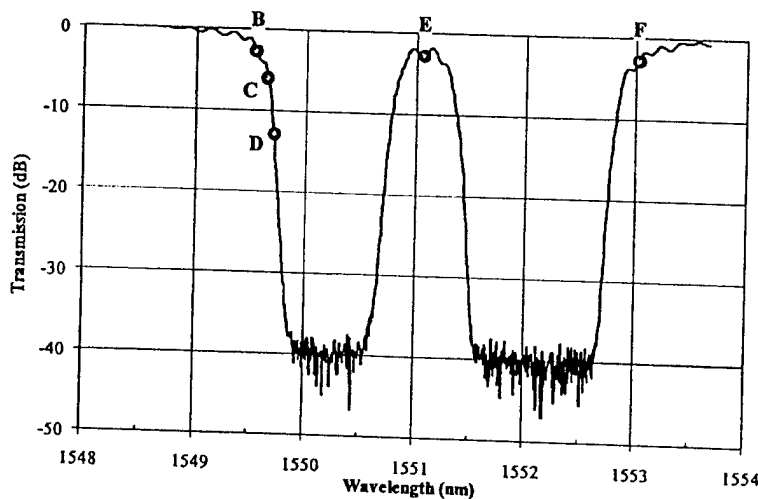
Fig. 1. Transmission spectrum of the grating pair, with bandgap centers at 1550.25 and 1552.10 nm, and 3-dB bandwidths 1.40 and 1.82 nm, respectively. The overlap transmission region had a 1551.05-nm central wavelength, a 0.5-nm 3-dB bandwidth, and −3-dB peak intensity transmission. Operating wavelengths of interest are B: 1549.55 nm, C: 1549.63 nm, D: 1549.70 nm, E: 1551.05 nm, and F: 1553.01 nm.
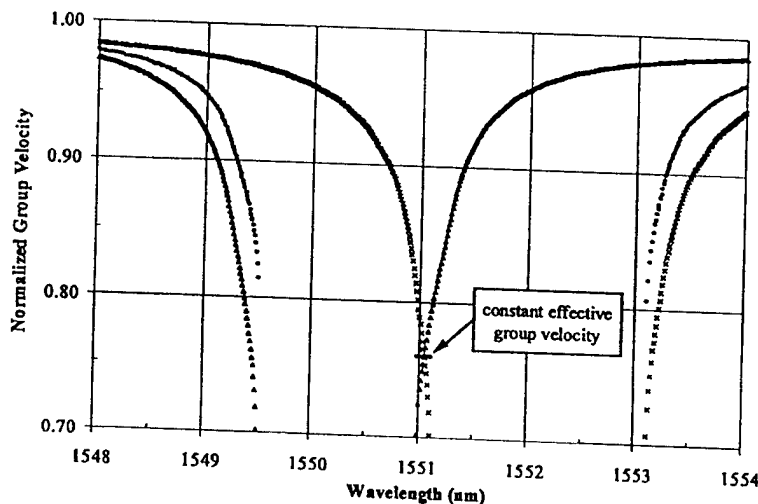

Fig. 2. IFO_Gratings simulation results. (△) normalized group velocity of the grating centered at 1550.25 nm, (×) normalized group velocity of the grating centered at 1552.10 nm, and (•) normalized effective group velocity of the gratings cascaded. The group velocities are normalized to the speed of light in bare fiber. Note the almost flat effective group velocity from 1550.99 to 1551.10 nm.

correlation and auto-correlation traces for point A was intentionally introduced by choosing the grating pair arm ~1 cm longer. Group delays of 11, 13, 15, 15, and 7 ps for points B, C, D, E, and F, respectively, were measured as the additional displacement of the cross-correlation trace relative to the auto-correlation trace. The maximum 15-ps delay corresponds to a group velocity 66% of the speed of light in bare fiber. Assuming a symmetric bandgap for each of the gratings the delay at E was expected to equal that at B plus F, 18 ps. At points E, B, and F the transmission loss amounted to 3 dB. In comparison, point D provided the same delay as E with a 13-dB transmission loss.

A zoom-in view of the cross-correlation traces for several wavelengths is shown in Fig. 3(b). From these we deduced the extent of pulse reshaping. The traces were purposefully superimposed and normalized to their respective peak values for ease of comparison. The structure that appeared at ~90 ps

was caused by the leading edge of the auto-correlation trace. The cross-correlation at A exhibited a FWHM of 19.0 ps and it was taken as the reference pulse shape. Operation at E produced a cross-correlation trace with a FWHM of 21.5 ps, 13% larger than that at A. There were three reasons for the slight pulse reshaping at E. First, for a uniform grating, there were oscillations in the transmission and group velocity characteristics [4]. Second, although the GVD was canceled, cubic and higher order dispersion were not [2]. Third, the 0.5-nm pulse bandwidth was larger than the 0.11-nm zero dispersion region. At C and D the cross-correlation FWHM were 28.3 and 29.3 ps, respectively. The pulses widened as expected since at these points there was no dispersion compensation.

IV. CONCLUSION

We have experimentally demonstrated a grating pair sequence with wavelength dependent group delay exhibiting
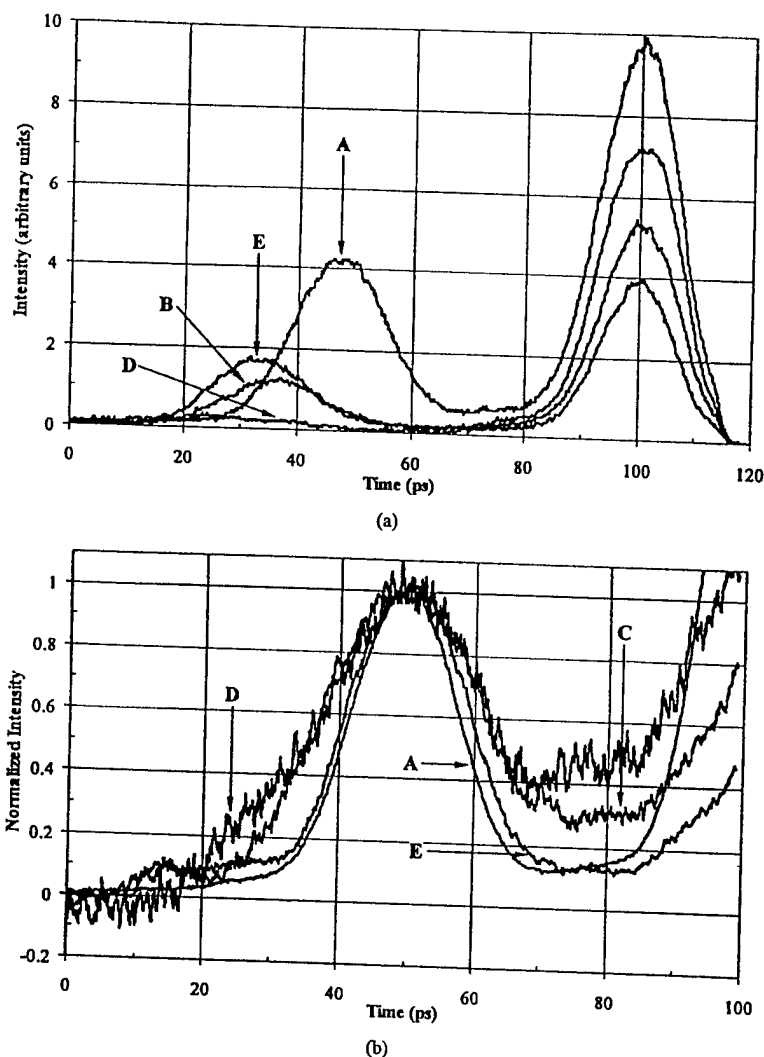
(a)

(b)

Fig. 3. (a) Correlation traces for the various operating wavelengths. The auto-correlation traces are located at 100 ps. (b) Zoom-in view of normalized cross-correlation traces for various operating wavelengths defined in Fig. 1.

compensated GVD over a 0.5-nm band. Over this range both gratings contributed to the optical pulse propagation characteristics enabling a 15-ps group delay with 3-dB transmission loss. One possible application of this is in matched filtering schemes, where for a fixed center wavelength one grating in the transmitter stretches the pulse in time while a conjugate grating in the receiver is used for pulse reconstruction. Both gratings can be further expanded as specially designed grating sequences to meet orthogonal code requirements among different channels for CDMA systems.

ACKNOWLEDGMENT

REFERENCES

[1] W. H. Loh, R. I. Laming, N. Robinson, A. Cavaciuiti, F. Vaninetti, C. J. Anderson, M. N. Zervas, and M. J. Cole, "Dispersion compensation over distances in excess of 500 km for 10-Gb/s systems using chirped fiber gratings," *IEEE Photon. Technol. Lett.*, vol. 8, pp. 944–946, July 1996.

[2] N. M. Litchinitser, B. J. Eggleton, and D. B. Patterson, "Fiber Bragg gratings for dispersion compensation in transmission: Theoretical model and design criteria for nearly ideal pulse recompression," *J. Lightwave Technol.*, vol. 15, pp. 1303–1313, Aug. 1997.

[3] N. M. Litchinitser and D. B. Patterson, "Analysis of fiber Bragg gratings for dispersion compensation in reflective and transmissive geometries," *J. Lightwave Technol.*, vol. 15, pp. 1323–1328, Aug. 1997.

[4] B. J. Eggleton, T. Stephens, P. A. Krug, G. Dhosi, Z. Brodzeli, and F. Ouellette, "Dispersion compensation using a fiber grating in transmission," *Electron. Lett.*, vol. 32, pp. 1610–1611, Aug. 1996.

[5] B. J. Eggleton, C. M. de Sterke, and R. E. Slusher, "Nonlinear pulse propagation in Bragg gratings," *J. Opt. Soc. Amer. B*, vol. 14, pp. 2980–2993, Nov. 1997.

[6] S. Wang, H. Erlig, H. R. Fetterman, E. Yablonovitch, V. Grubsky, D. S. Starodubov, and J. Feinberg, "Measurement of the temporal delay of a light pulse through a one-dimensional photonic crystal," *Microwave Opt. Technol. Lett.*

[7] S. Wang, H. Erlig, H. R. Fetterman, V. Grubsky, and J. Feinberg, "One-dimensional photonic crystals for CDMA," in *Multimedia Networks: Security, Displays, Terminals, and Gateways, Proc. SPIE 3228*, 1997, pp. 408–417.

[8] T. M. Goyette, W. Guo, F. C. De Lucia, J. C. Swartz, H. O. Everitt, B. D. Guenther, and E. R. Brown, "Femtosecond demodulation source for high-resolution submillimeter spectroscopy," *Appl. Phys. Lett.*, vol. 67, pp. 3810–3812, Dec. 1995.

Fabrication and Characterization of High-Speed Polyurethane-Disperse Red 19 Integrated Electrooptic Modulators for Analog System Applications

Yongqiang Shi, Wenshen Wang. *Member. IEEE.* James H. Bechtel, Antao Chen.
Sean Garner, *Student Member. IEEE.* Srinath Kalluri, William H. Steier. *Fellow. IEEE.*
Datong Chen. *Student Member. IEEE.* Harold R. Fetterman. *Fellow. IEEE.*
Larry R. Dalton, and Luping Yu

Abstract—The fabrication and characterization of polymeric electrooptic modulators, made of a thermally crosslinkable polyurethane with Disperse Red 19 side chains, are summarized in this paper. Straight channel and Mach–Zehnder modulators have been fabricated, packaged and tested for the fiber-optic analog transmission system applications. Device performances including halfwave voltage, insertion loss, on–off ratio, and modulation frequency responses were measured. Long-term halfwave voltage stability, dc-bias voltage stability, and optical power handling capability at 1.3-μm wavelength were investigated. A carrier-to-noise ratio of 53 dB and 80-channel television transmission have been demonstrated using the packaged polymer modulators.

I. INTRODUCTION

ELECTROOPTIC (E-O) polymers are a class of new materials gaining increasing research interest for high speed E-O devices and their commercial applications [1]–[8]. The low (2.5 ~ 4) and nondispersive relative dielectric constants of E-O polymers can result in low capacitance for lumped circuit devices and provide a natural velocity matching between optical waves and microwaves for broad-band traveling-wave structures using simple planar circuits. The easy thin film processing technology of polymers promises a low cost and fast fabrication of E-O devices. Their compatibility with semi-conductor substrates and circuits allows vertical integration of E-O polymer devices on semiconductor driving circuits and detectors as a compact hybrid optoelectronic module for

various applications [9]–[10]. In addition, the recent advances in highly active chromophores have exhibited a great potential in the synthesis of polymers with E-O coefficients 2 ~ 3 times larger than those of typical crystalline materials [11]–[12]. In fact, several poled polymers have shown E-O coefficients larger than 30 pm/V [13]–[14].

E-O polymer-based high-speed modulator research started in the early 1990's when 20 GHz modulation was observed from a Mach–Zehnder (M–Z) modulator using a thermoplastic E-O polymer [1]. Later, 40-GHz 3-dB bandwidth was demonstrated in an E-O polymer modulator with a similar polymer [2]. To improve the device stability, new thermoset and other thermally stable E-O polymers were used in device fabrication, and modulation frequencies from 20 to 60 GHz were demonstrated [3]–[6], [15]. At the same time, the required driving voltage for the high speed polymer modulators decreased significantly due to the improvement in material nonlinearities and efficient poling. A halfwave voltage V_π of 5 V with a halfwave voltage-modulation length product ($V_\pi L$) of 13 V·cm was obtained [15].

Analog fiber-optic transmission systems are widely used in fiber-optic sensors, community access television (CATV) distribution, radio frequency (RF) remoting, phased array radar feeds, and analog/digital microwave links. For most externally modulated fiber-optic analog transmitters, the desired performance characteristics are low V_π, low-optical insertion loss, wide frequency bandwidth, large output power, and high stability. Similar requirements can also be found in digital fiber-optic transmitters. In this paper, instead of pursuing a single parameter optimization such as a wider modulation bandwidth or a lower V_π, we focus on the E-O polymer modulator fabrication process and a comprehensive performance test for practical analog system applications. A detailed evaluation of E-O polymer devices will provide a panoramic view of our E-O polymer device fabrication and testing efforts. The test results will also provide useful information for future research directions of material synthesis and device constructions.

In this paper, starting from material processing, the fabrication and the tests of E-O polymer modulators are discussed

Fig. 1. Structure of PUR-DR19 polymer: (a) prepolymer and (b) crosslinker triethanolamine.

Fig. 2. Refractive index of an unpoled PUR-DR19 film.

using a representative E-O polymer. Polyurethane with Disperse Red 19 side chains (PUR-DR19) [16]–[17]. Our tests include not only performance parameters such as V_π, insertion loss, and RF responses, but also the stability parameters such as optical power handling capability, dc-bias stability, and V_π stability. Demonstration of applications for analog transmission systems are also presented. Although the discussion on device fabrication is based on E-O modulators for externally modulated fiber-optic analog transmission systems, the technology including packaging and testing can be applied to devices used in other systems such as digital transmitters and integrated waveguide switches.

II. MATERIAL PREPARATION AND PROPERTIES

A. Preparation of Substrates and Polymer Thin Films

Our polymeric E-O modulators were made of two different polymers: a passive polymer (Epoxylite 9653 series [18]) for both upper and lower cladding layers and the PUR-DR19 E-O polymer for the waveguide layer. The PUR-DR19 polymer was obtained from mixing and thermal crosslinking of a prepolymer and a crosslinker, triethanolamine, as shown in Fig. 1. The material synthesis and characteristics were reported in [16] and [17]. The crosslinking time and temperature were typically 20 ~ 30 min at 160 °C or longer at lower temperatures [16].

Polished fused silica slides were chosen as the substrates for the E-O polymer modulator in this work. Other substrates such as silicon wafers can also be used. For the ground electrode of the device, chromium/gold layers were deposited on the substrates by dc sputtering. Titanium/gold layers were also used to improve adhesion to the substrate.

The lower cladding layer was spin-coated on the substrates. The two components of the cladding polymer (Epoxylite 9653-2) were mixed in a 1:1 ratio. The spin speed was calibrated for different thickness, and the cladding solution may need to be diluted when thinner layers are desired. In our fabrication process, the spin speeds were adjusted for a film thickness between 4–6 μm. The coated substrates were thermally cured before the spinning of the active polymer layer.

In a typical device fabrication run, 0.20 g of the PUR-DR19 prepolymer were mixed with 2.0 ml dioxane in a dry and clean vial. After the powdery prepolymer was completely dissolved,
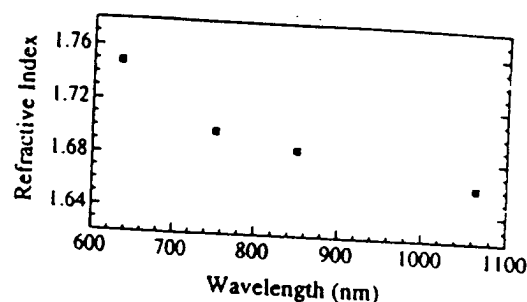
the solution was mixed with 1.04-ml crosslinker solutio which was obtained by dissolving 0.52 g triethanolamine i 25 ml dioxane. The prepolymer and crosslinker mixture wa filtered through a 0.2==μm filter and then precured on a 80–8: °C hot plate for approximately 1 h. During the precuring dry nitrogen was purged into the solution containing vial t remove excess solvent due to the addition of the crosslinker The precured solution was then cooled to room temperatur and filtered again through a 0.2-μm filter. The final polyme solution was spin-coated on the lower cladding layer with a film thickness 1.2–1.5 μm. The obtained polymer films appeared to be deep orange in color with a smooth and shining surface.

After drying overnight in a vacuum oven at 45 °C–60 °C. the polymer films were poled on a corona discharge poling set-up. The typical needle-to-plane distance was ~2 cm, and the applied dc voltage to the needle electrode was 5–6 kV. which yielded a poled area approximately 2.5 cm in diameter. The poling temperature profile of the heater was controlled by a programmed temperature controller. The curing time for a waveguide device was 45 min at 140 °C. The curing temperature was probed between the heater and the sample holder and not at the sample, so the actual sample temperature was slightly lower than the thermocouple reading. A successful poling yields no visible damages on the surfaces of the poled polymer samples. To monitor the efficiency of corona poling. test samples of PUR-DR19/Epoxylite were deposited and poled on transparent indium–tin–oxide (ITO) coated substrates for second-harmonic generation (SHG) measurement.

B. Properties of Polymer Materials

PUR-DR19 has a low-optical loss window covering the near infrared wavelength range. The absorption peak corresponding to the $\pi - \pi^*$ transition is approximately at 470 nm. The refractive indices of an unpoled but cured polymer thin film were measured by ellipsometry and waveguiding methods (Fig. 2).

The nonlinear optical properties were characterized by both SHG and direct E-O modulation measurements. At 1064-am fundamental wavelength, a resonance enhanced SHG coefficient d_{33} of 120 pm/V was measured [17]. Using a two-level dispersion model, an E-O coefficient r_{33} of 12 pm/V was extrapolated from the SHG data. Direct E-O coefficient measurements at several wavelengths were carried out using an external M-Z interferometer [17], a double-slit interferometer [19], modulated ellipsometry, attenuated total internal
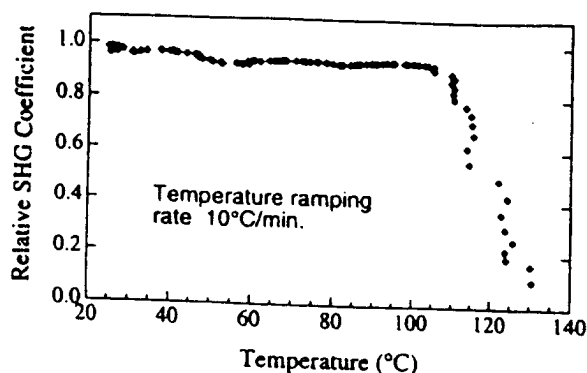
Fig. 3. The normalized second harmonic generation coefficient as a function of temperature. The temperature ramping rate was 10 °C/min.

reflection, and waveguide modulator. The E-O coefficient of a well-poled film was typically 12–14 pm/V at 1.3 μm wavelength. The SHG signal levels of PUR-DR19 films spun on lower cladding layers were consistent with those directly spun on ITO/glass substrates, indicating that most of the poling voltage was dropped across the PUR-DR19 film.

The thermal stability of the second-order nonlinearity of poled PUR-DR19 films was characterized by an *in situ* SHG-temperature ramping method. For the samples cured at 140 °C heater temperature, the SHG signal remained stable until the sample temperature reaches 100 °C–110 °C, as shown in Fig. 3. For samples cured at higher temperatures (160 °C), long-term stability at 90 °C was observed [17], [20]. During our device fabrication, solvent drying and baking of the poled films were controlled at 60 °C–65 °C, which showed no effect on the material nonlinearity.

III. E-O POLYMER MODULATOR DESIGN

A traveling-wave integrated E-O modulator is generally a combination of an optical waveguide and a microwave waveguide. The optimized parameters of both waveguide structures sometimes conflict. A balanced design often requires a compromise among these parameters. In our modulator design, we have focused on a balanced performance among driving voltage, frequency response, and fabrication process.

A. Optical Waveguide Design

A triple stack structure, i.e., an E-O polymer layer sandwiched between two cladding layers, was used to provide vertical confinement for the optical wave. Lateral confinement was achieved from a ridge structure on the guiding layer. Optimized input/output (I/O) fiber coupling requires a waveguide cross section of 5 μm × 5 μm or larger. We have compromised I/O mode matching for material compatibility and fabrication flexibility. The polyurethane based coating material, Epoxylite 9653, has good chemical and physical properties as claddings for PUR-DR19 active waveguide layer. It has a lower bulk resistivity than PUR-DR19 to facilitate electric field poling, can be crosslinked to withstand solvents during the brief spinning of subsequent layers, and can be wet by the PUR-DR19 solution without special surface treatment. Because of the fixed index difference between guiding layer and cladding

layer, we can only optimize the waveguide design by adjusting the width and etch depth of the ridge waveguide structure. Future optimization in vertical dimension can be achieved by using similar cladding materials that are modified to yield a smaller index difference, such as polymers with doped or attached chromophores.

We have used a waveguide width of 5 μm, film thickness of 1.3 μm, and an etched ridge depth of 0.2 μm in our device fabrication to ensure single-mode operation, which has been confirmed by experimental observation. In addition, the different curing procedures for upper and lower cladding layers resulted in a small index difference for the cladding layers, which allowed a slightly larger single-mode waveguide cross section (up to 7 μm in width) with an etch depth of 0.2 μm.

Two modulator architectures were used in our device design: the straight channel modulator architecture and the integrated M-Z interferometer architecture, as shown in Fig. 4. The modulation characteristics of the two modulator architectures are listed in Table I for comparison. The straight channel waveguide modulators can be used as phase modulators, when input polarization is arranged to excite transverse electric (TE) or transverse magnetic (TM) mode only. They can be also used as intensity modulators when the input polarization is arranged to excite TE and TM modes equally with a compensator and an analyzer at the output end [21]. Our straight channel modulators were typically 20–32 mm long with electrodes 12–30 mm in length. The modulation arm lengths of the M-Z modulators were 14–20 mm, and the length of the Y-branch transition with a continuous S-bend was 3 mm at each side. As shown in Table I, the main difference between the straight channel and M-Z modulator is that the M-Z modulator can exploit the largest E-O coefficient r_{33} while straight channel modulator utilizes only 2/3 of r_{33} for intensity modulation. However, for the same optical waveguide length, the straight channel device allows a longer electrode while M-Z modulators need extra space for waveguide branching and combining.

B. Microstrip Line Electrode Design

The microwave circuit design of the PUR-DR19 polymer modulators was based on the integrated microstrip line (MSL) structures. The advantages of such structures include high and uniform interaction field distribution, broad-band frequency response, and suitability for corona poling. The characteristic impedance of a MSL is primarily determined by the ratio of the line width and the electrode separation. A wider electrode would have lower characteristic impedance, and vice versa. A 50-Ω transmission line, compatible with the majority of the microwave sources, can be obtained by carefully choosing the width and separation of the electrodes. Based on the measured relative dielectric constant of ~3.2 for PUR-DR19 [20] and 2.5 estimated for cladding polymer layers, we have numerically simulated the characteristics of the MSL structure using commercial microwave simulation software (Touchstone, EE Soft). The width-to-gap ratio of 2.5–3.0 was chosen for 50-Ω impedance. For a typical gap distance of 10–12 μm, the MSL width was 30–36 μm. The calculated frequency
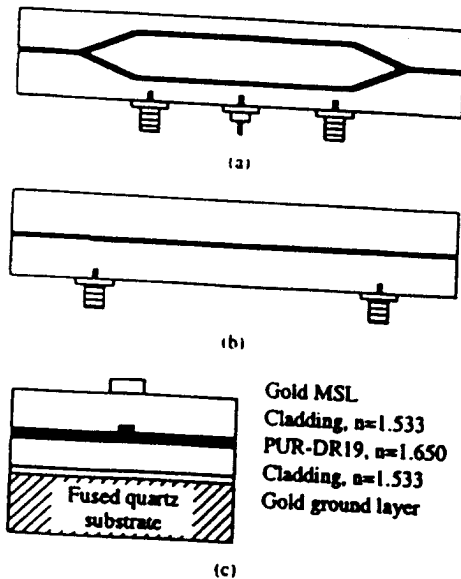
Fig. 4. The schematic diagrams of PUR-DR19 M-Z (a) and straight channel (b) modulators and the cross section of the waveguide (c).

TABLE I
CHARACTERISTICS OF STRAIGHT CHANNEL AND M-Z MODULATORS

	Mach-Zehnder	Straight Channel
r_{eff}	r_{33}	$r_{33} - r_{13}$
$V_\pi L$	$V_\pi L_{MZ}$	$1.5 \times V_\pi L_{MZ}$
Optical power in active waveguide	$P_i/2$	P_i
Device length	L + Y branch	L

bandwidth–modulation length product for this simple MSL structure was ~120 GHz·cm, which gave ~60-GHz bandwidth for a 2-cm interaction length. However, the actual device performance will be determined by the workmanship, accuracy of machining, properties of electrical connectors, and cables.

In addition to the characteristic impedance consideration, the design was also an engineering compromise among other considerations. Smaller electrode gap design would result in low driving voltage. However, this could lead to higher microwave loss and tighter fabrication tolerance because the MSL needs to be narrower to maintain 50-Ω impedance, and therefore, the ohmic loss would be higher.

IV. DEVICE FABRICATION AND PACKAGING

As discussed in Section II, the device fabrication process actually started from the materials preparation stage, followed by thin film spinning, and then electric field poling of the E-O polymer layer. This section covers the waveguide definition, electrode fabrication, and device packaging.

A. Fabrication

Channel waveguides were defined on the poled polymer thin films using standard photolithography technology. A positive photoresist layer was directly spun on the polymer surface after poling, and patterned as an etch mask. Then the maske samples underwent an oxygen plasma reactive ion etchin (RIE) process. The etch conditions such as RF power, oxyge pressure, and flow rate were optimized for the best surfac, morphology [22]. With an etch rate controlled at ~200 Å/min, smooth channel waveguide walls were obtained after cleanin, off the photoresist mask. The height of the etched ridge wa, checked by a surface profiler and was within ±10% of th, expected value.

Epoxylite 9653-1 was spin-coated on the patterned polymei film to form the top cladding layer. After drying the triple-stack samples at room temperature, a thin layer of chromium-gold layer was sputtered on the top surface and was then covered with a photoresist layer. A gold MSL electrode was masked and electroplated to a thickness of 5–8 μm followed by cleaning off the mask and wet etching. Two small quartz pieces (clamping plates) were mounted on both ends of the waveguides to sandwich the polymer layers between the clamping pieces and the substrate. Such a structure can protect the polymer layers from the shear forces of the dicing blade during cutting and allows us to obtain a secure bond between the optical waveguide and the fiber pigtail because of the large bonding cross-section. After dicing cut, the endfaces were polished with a modified fiber polisher.

B. Packaging

The general requirements for E-O polymer modulator packaging are rugged structure, fiber pigtail, convenient dc-bias connection, and standard 50-Ω RF ports. Our device packaging effort was focused on fiber pigtail to polymer waveguides and microwave interface to the MSL.

Our approach to fiber pigtailing was to bond I/O fibers directly to the polished waveguide endfaces using active alignment. The optical fibers for modulator packaging were connectorized at one end and mounted in a ferrule at the other end. Polarization maintaining (PM) fibers, with keyed FC-PC connectors, were used as the input fibers for all modulators to ensure proper input polarization. The polished ferrule was first coarsely aligned to the polymer waveguide, and then a laser beam was coupled into the optical fiber. The output power from the polymer waveguide was monitored and optimized by adjusting the mounts that held the fiber and the sample. Once the optimized coupling was achieved, the ferrule was glued to the polymer waveguide by a UV adhesive. The pigtailed modulator chip was next mounted onto a brass case with clamps and adhesives. The fiber pigtails were secured through the end walls with crimp sleeves and rubber boots for stress relief.

The output fibers were different for M-Z and straight channel modulators. A regular single-mode fiber was used for M-Z modulators, while the requirement in a straight channel modulator needs more consideration. For a phase modulator, the output fiber was either a PM or a regular single-mode fiber to maintain the modulated phase front. However, for an intensity modulator, a polarizing (PZ) fiber was used as the external polarizer. The orientation of the polarizing fiber was adjusted for the maximum extinction ratio. The variable
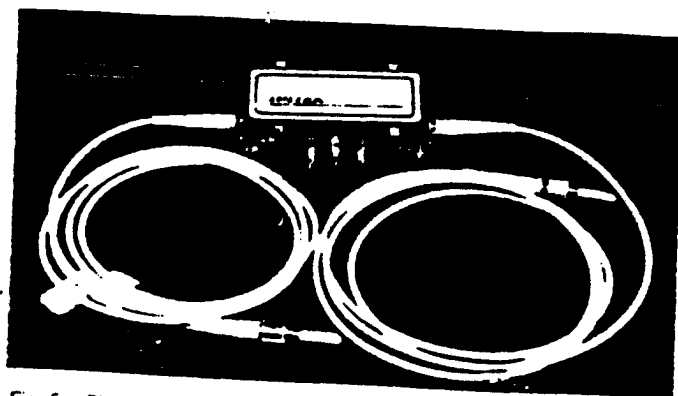
Fig. 5. Photograph of a packaged M–Z modulator.

Fig. 6. Intensity modulation response of a packaged M–Z modulator arranged in a push–pull configuration. The upper trace is the modulator output signal, and the lower trace is the applied voltage.

phase compensation was achieved via the E-O effect by applying a dc voltage to the electrode through an RF bias-tee. The elimination of free-space compensator and polarizer with PZ fiber and built-in waveguide compensator allowed us to package a compact, rugged straight channel intensity modulator.

To launch a microwave signal from a source to the 50-Ω MSL on the polymer modulator, we have used the coaxial to planar microwave transitions (for example, the Wiltron K and V series transitions). Typical launchers have a launching pin about a few hundred micrometers in diameter. Direct application of the launcher to 50-Ω MSL will cause severe size mismatch. Such mismatch can cause difficulties for electrical contact during microwave packaging and seriously degrade device performance.

A typical way to improve the electrical contact is to introduce a contact pad and tapered transition to the MSL. We have used rectangular contact pads and linear transitions between the wide contact pads and the 50-Ω MSL in our modulators. In order to achieve wide-band frequency response in the PUR-DR19 modulators, the size of the pads and the transitions were optimized to support the operation frequencies up to 60 GHz while maintaining good electrical contact to the microwave launchers to ensure good responses at both low and high frequency ends.

In our packaged modulators, as shown in Fig. 5, the connector pins were directly pressed onto the ends of the MSL electrode. Occasionally, a tiny drop of conducting epoxy was used to improve connection. The modulator chips were carefully grounded to minimize RF resonance. A dc feedthrough connector was used for dc-bias port in M–Z modulators. External 50-Ω microwave termination was used.

V. MODULATOR TESTS

Our modulator tests were focused on both device performance characteristics and operation stability. The performance ests include the measurements of halfwave voltage, optical nsertion loss, modulation frequency bandwidth, electrode RF oss, and the impedance of the driving electrodes. The stability ests cover the E-O coefficient stability, the optical power handling capability, and the bias voltage stability. All these tests re directly related to the field application of the integrated olymer modulators.
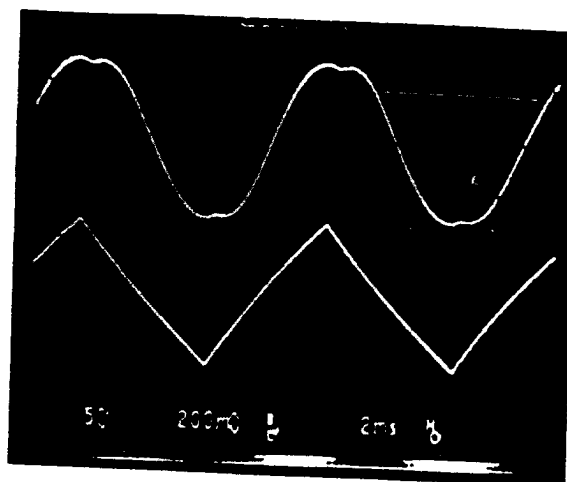
A. Performance Tests

Halfwave Voltage V_π: Given the optical modulation index (OMI) in an externally modulated fiber-optic transmitter, the required driving power is derived from modulator's V_π, which is a function of the material E-O coefficient, device structure, electrode geometry, and modal property of the optical waveguide.

We tested a packaged PUR-DR19 M–Z modulator with 15-mm-long arms covered by electrodes in each optical path. The MSL-ground separation was 11 μm. The electrodes were arranged in a push–pull configuration so that the modulation fields had opposite directions on the two arms of our M–Z modulator. A bias-tee was used to couple dc-bias voltage to one of the modulator electrodes. The output optical beam was directly coupled to an optical power meter (HP 8152A) which converted the optical power into electric signal. From the turning point of the output signal on the oscilloscope (Fig. 6), a push–pull V_π of 11 V was obtained. The corresponding $V_\pi L$ product was 16.5 V·cm. Without using the push–pull configuration, the single arm modulation V_π was ~23 V. From the measured V_π and the waveguide geometry, an E-O coefficient r_{33} of 13 pm/V was obtained when an effective overlap integral value [13] of 0.75 was taken.

Halfwave voltages of 36–55 V, depending on the electrode length and gap distance, were measured for the straight channel waveguide intensity modulators. The higher V_π values were expected since the effective E-O coefficient for straight channel modulator is smaller than that of an M–Z device, as listed in Table I. The lower V_π can be obtained by using longer electrode when wide bandwidth is not the main concern. The E-O coefficient from V_π measurement was similar to that from M–Z modulators and was consistent with SHG extrapolation and other measurements [19].

Waveguide Loss and Device Insertion Loss: The total device insertion loss was the sum of the waveguide propagation loss and the fiber–waveguide–fiber coupling loss. The waveguide propagation loss was a collection of the losses from material intrinsic absorption, waveguide/cladding

layer scattering, and poling induced scattering [23]. At 1.3-μm wavelength, the unpoled PUR-DR19 planar waveguides exhibited ~1-dB/cm loss mainly due to material absorption [22], [24]. To find the losses induced by RIE, we compared the waveguide losses of a slab waveguide before and after the RIE process. Under our optimized etching conditions, no significant increase in waveguide loss was observed [22], [24]. For our packaged PUR-DR19 polymer modulators, the insertion loss was dominated by the fiber-waveguide-fiber coupling loss due to significant mode mismatch. The standard 1300 nm optical fiber mode size was ~9 μm in diameter, but the waveguide sizes of the PUR-DR19 modulators were 1.3-μm thick and 5–7-μm wide. The fiber-to-waveguide coupling loss for PUR-DR19 waveguide (cross section 1.3 μm × 7 μm) was estimated numerically to be 5.0 ± 0.2 dB/facet. The insertion losses and their distribution of the test waveguides were measured during prototype modulator chip characterization. The measurement set-up consisted of an input PM fiber, a 20× output microscope objective, and the test chip mounted on a translation stage. The first set [Fig. 7(a)] was the insertion losses from a group of poled straight channel waveguides separated by 210 μm with electrodes on top. The average loss was 11.5 dB, which included ~5-dB fiber to waveguide coupling, ~3-dB output coupling loss from the microscope objective, and losses from 2.5-cm-long waveguides. The variations in waveguide transmission were within ±0.7 dB of the average output level. The average propagation loss was calculated as 1.4 dB/cm. The numerical calculation of the coupling loss and the measured average waveguide propagation loss were confirmed by using a waveguide cut-back method, in which the fiber-to-waveguide loss and the propagation loss of PUR-DR19 waveguides were measured as 5–6 dB/facet and 1.4 dB/cm, respectively. The difference between the losses of the poled (~1.4 dB/cm) and unpoled (~1 dB/cm) waveguides was mainly due to poling. The second data set [Fig. 7(b)] was the loss measurement results of an M–Z modulator array with waveguide widths from 5 μm to 7 μm separated by 250 μm. The average loss was 13.5 dB. Since no voltage was applied for quadrature bias, the waveguide loss distribution was slightly larger than that of the straight channel waveguides, which may result from small asymmetry of the interferometer arms. The typical insertion loss of a packaged PUR-DR19 M–Z modulator was ~15 dB when 3-dB quadrature bias loss was excluded. The extra losses were due to the fiber shift during bonding epoxy curing which can be reduced by improved curing process.

On–Off Ratio: The on–off ratio was also measured for the polymer modulators before and after packaging. The fiber pigtailed modulators showed higher contrast ratios than those of lens coupled test chips. Obviously, the out-coupling fiber functioned as a mode filter which blocked the light leaked through the cladding or scattered by the waveguide. Good optical on–off ratios were obtained from the packaged modulators, as listed in Table II.

Frequency Response: The microwave characteristics of our PUR-DR19 modulators were measured by a network analyzer for their scattering matrix elements, or the S-parameters. The tested RF transmission S_{21} from connector to connector is shown in Fig. 8 from 45 MHz to 20 GHz for a 2.8 cm long
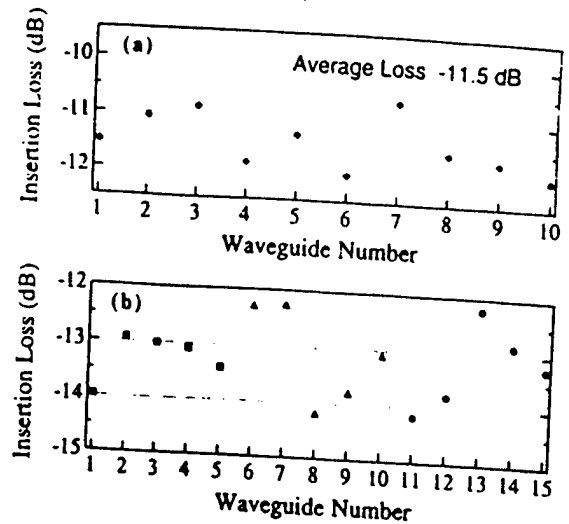

Fig. 7. (a) The insertion losses measured from a group of straight channel waveguides on a poled PUR-DR19 film under microstrip line electrodes. (b) The insertion loss measured from 5 μm (square), 6 μm (triangle), and 7 μm (circle) arrays of M–Z modulators on a poled PUR-DR19 film.

TABLE II
MEASURED MODULATOR OPTICAL ON-OFF RATIO FOR PACKAGED MODULATORS

Modulators	Typical	Best
Straight Channel	13–20 dB	>30 dB
Mach-Zehnder	15–20 dB	>20 dB

(including two 90° bend) MSL electrode. The measured S_{21} showed a smooth response to 20 GHz, limited by the network analyzer used. The calculated microwave loss (including the coupling loss) from the measured S_{21} is about 0.56 dB/(cm-GHz$^{1/2}$). The reflection S_{22} measurement showed a better than 15 dB return loss and good impedance matching. At 10 GHz, the measured impedance was $52.4 + i0.2\ \Omega$.

The same M–Z modulator was tested on a lightwave signal analyzer for its optical modulation frequency response. The measured response is shown in Fig. 9 from 2.7 GHz to 18 GHz, limited by our tracking generator (HP70301A). No roll-off in frequency response was observed in our measurement. The difference between the measured S_{21} and lightwave response can be explained by the fact that the S_{21} measures the total losses of the entire microwave circuit including the MSL, transitions, and connectors, while the lightwave data results from the interaction electrode length (1.5 cm) and phase mismatch. For higher frequencies, an optical heterodyne technique was implemented to measure the frequency response up to 60 GHz [6]. A broad-band response from 2 ~ 60 GHz is shown in Fig. 10 for an earlier straight channel modulator.

B. Modulator Stability Tests

There are several stability issues related to the application of polymer modulators. It was realized earlier that the molecular alignment stability over the life-time of the device at the allowed environment conditions was one of the most important issues. The optical power stability (optical power handling capability) of the E-O polymer device at 1300 nm was raised later when researchers discovered 1300-nm laser induced
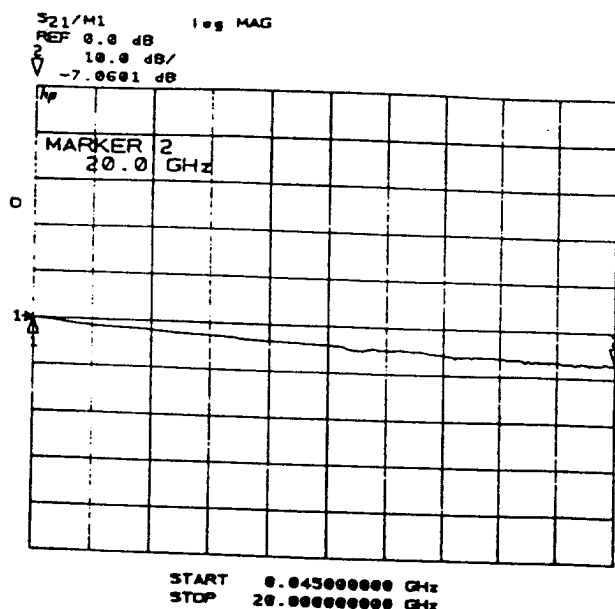
S21/M1   log MAG
REF 0.0 dB
10.0 dB/
-7.0601 dB

MARKER 2
20.0 GHz

START   0.045000000 GHz
STOP   20.000000000 GHz

Fig. 8. Connector-to-connector RF transmission parameter (S_{21})of a microstrip line electrode with contact pads of a M–Z modulator. The vertical axis is the transmission loss (10 dB/div.), and the horizontal axis is frequency (2 GHz/div.).
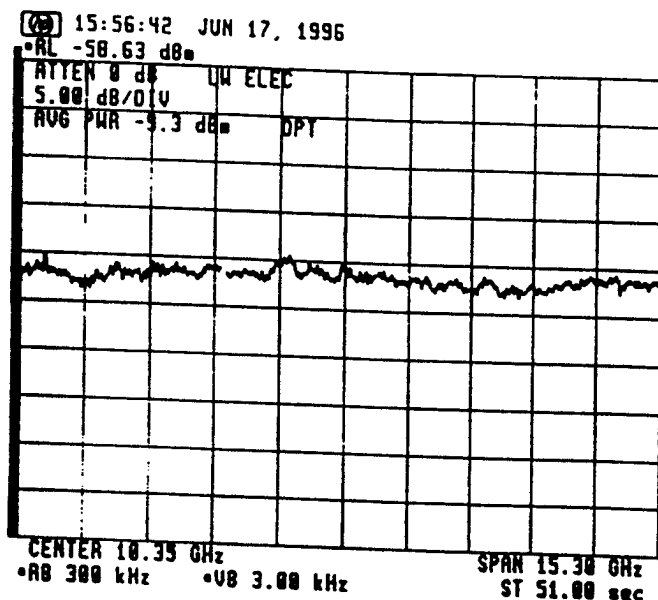
15:56:42 JUN 17, 1996
•RL -58.63 dBm

ATTEN 0 dB   UW ELEC
5.00 dB/DIV
AVG PWR -5.3 dBm   OPT

CENTER 10.35 GHz
•RB 300 kHz   •VB 3.00 kHz   SPAN 15.30 GHz
ST 51.00 sec

Fig. 9. The frequency response of a M–Z modulator measured by lightwave signal analyzer from 2.7 to 18 GHz.
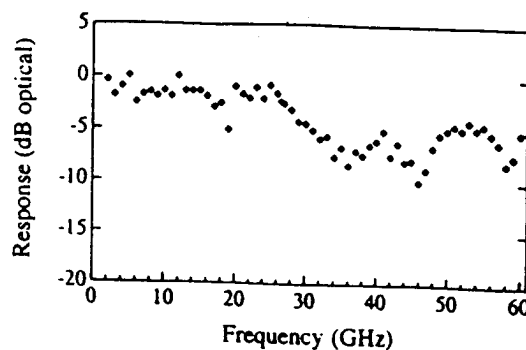

Fig. 10. The frequency response of an early PUR-DR19 straight channel modulator. The responses from 2 GHz to 26 GHz was measured directly from spectrum analyzer and from 26 to 60 GHz was measured by optical heterodyne technique.
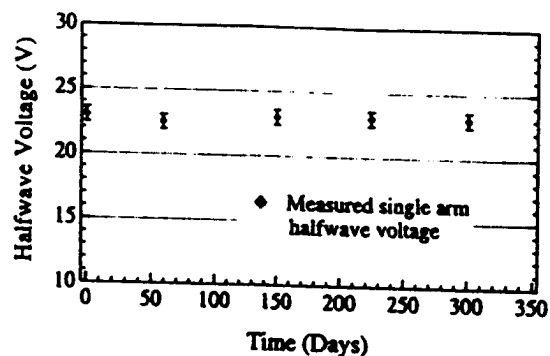

Fig. 11. The halfwave voltage stability of a packaged modulator stored at room temperature.

damage in E-O polymers with a dimethylaminonitrostilbene (DANS) chromophore [25]. Another stability issue addressed recently was the dc-bias stability of the modulators during long-term operation [26]. The tests of the temporal stability, optical power handling capability, and modulator bias stability were the center of our device stability measurements.

Half-Wave Voltage Stability: To maintain a stable OMI in an externally modulated RF link, a stable V_π is required for the E-O modulator. The packaged E-O polymer modulators provided us a convenient way to repetitively monitor the V_π of modulators over a long period of time. The stability of our modulator's V_π reflects the chromophore alignment stability in PUR-DR19 polymer. At room temperature, the PUR-DR19

modulator showed a very stable temporal behavior: no detectable V_π change was observed over a period of ~300 days, as shown in Fig. 11. In fact, although the modulator was mainly stored at room temperature, it has been used in various device tests including long-term bias stability and was occasionally cycled up to ~60 °C.

Photochemical Stability: Typical externally modulated analog fiber-optic transmitters require an output optical power between 1–50 mW. The corresponding input power is 5–250 mW which translates to an optical intensity on the order of 10^4–10^6 W/cm^2 inside the waveguide. These intensity levels are well below the conventional damage threshold of the polymers at near infrared. However, the small photosensitivity of certain chromophores often results in a slow degradation of the material properties. Since a practical component must be reliable in field service for a number of years with a low failure rate, the endurance of the polymer devices under continuous photoillumination is of vital importance for the commercialization of polymer photonic devices.

We have tested the photochemical stability over a spectral span from 543 nm visible to 1320 near infrared wavelengths for PUR-DR19 polymer films [27]. Except for the photoinduced depoling effect at visible wavelengths, PUR-DR19 films were quite stable at infrared wavelengths for low intensities, which was evidenced by our packaged modulators operating for weeks during bias stability tests at ~10-mW 1320-nm input power without showing any degradation. In our high optical power test, a straight channel waveguide was directly pigtailed
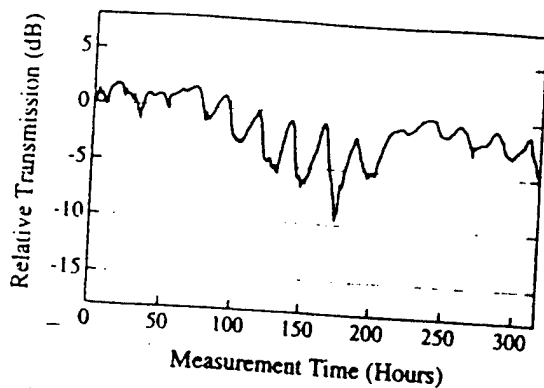
Fig. 12. Normalized transmission of a PUR-DR19 waveguide as a function of exposure time at 1320 nm. The input power was 150 mW.

Fig. 13. The measured dc-bias voltage of a PUR-DR19 modulator over 120 h.

to an optical fiber and connected to a fiber coupled 150 mW 1320 nm Nd:YAG laser. The waveguide was sandwiched between two pieces of quartz plates and was isolated from air. The output of the waveguide was monitored over 300 hours, as shown in Fig. 12. Clearly, at high input power level, the waveguide output exhibited an unpleasant oscillatory structure, an indication of possible photochemical degradation in the test PUR-DR19 waveguide. Compared with test results using DANS containing polymers [25], [28], however, the optical transmission decay rate in PUR-DR19 was ~2 orders of magnitude slower than those in polymers with the DANS chromophore.

DC-Bias Voltage Stability: High-performance multioctave wideband analog signal transmission systems require minimized harmonic distortion of the input signals. The minimization of the composite second order (CSO) distortion is usually achieved by applying proper dc-bias voltage to the dc-bias port of an M–Z modulator to reach the so-called quadrature operation point. Because of the layer structure of modulators, electrical charges may accumulate along the boundaries between different material regions after certain service time. The charge accumulation may enhance or screen out the external applied electric field and therefore, change the bias point. These effects have been observed and well-documented for some crystalline modulators [29].

In polymer devices, little attention was paid to the dc-bias stability until recently [26], [30]. Obviously for commercial applications, the low CSO distortion of an analog system requires that the deviation of the bias point from the quadrature point be within a very small range. A feed-back bias control circuit is required to provide the precise bias control. The smaller the bias drifting range is, the easier the control circuit design will be. Therefore, the device bias point must be traceable within a certain range and remains relatively stable.

The PUR-DR19 modulators exhibited a traceable dc-bias voltage in our tests. A computer controlled automatic bias control circuit was used to monitor the bias drifting behavior over a period of several days. With a sinusoidal signal applied to the RF port as a pilot tone, the output optical signal was detected by a photoreceiver and the second-harmonic frequency (2f) of the pilot tone was measured by a lock-in amplifier. The computer monitored the 2f signal and controlled the bias voltage to minimize the 2f signal. Both the
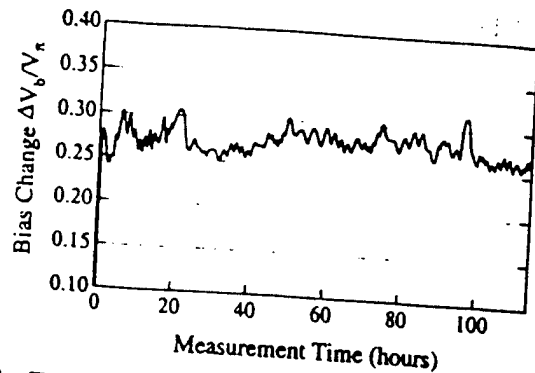
dc voltage and harmonic signal were recorded by the computer. The recorded bias voltage data showed that PUR-DR19 M–Z modulators have a relatively small dc-bias drift. The bias voltage fluctuation during a 120-h testing period was less than 10% of V_π, as shown in Fig. 13. No "run away" behavior, i.e., a continuous drift of bias voltage in one direction [28], [30], was observed. To further investigate the bias voltage stability under a large perturbation, we purposely switched the bias voltage to the adjacent quadrature points. The PUR-DR19 modulator exhibited a "negative" recovery tendency: the bias voltage was always drifting against the external voltage change, which provided intrinsic stability for the modulator device.

System Application Tests: We have tested the packaged PUR-DR19 M–Z modulators for a practical CATV transmission system application using standard procedures and commercial testing equipment (Matrix Multiple Signal Generator, HP Lightwave Analyzer, and an IPITEK® CATV optical receiver). With an OMI of 3.4% and a standard 0 dBm (1 mW) received optical power, a high-quality RF signal was obtained at 55.25 MHz for NTSC (National Television System Committee) Channel 2 (Fig. 14). The corresponding calculated carrier-to-noise ratio was 53 dB, limited by the receiver shot noise, which was the same as that measured in a commercial system using a LiNbO₃ modulator. The required driving power was larger than that for LiNbO₃ modulators because the V_π of the test polymer modulator was higher. The test PUR-DR19 modulator has also transmitted 80 channels of NTSC CATV signals to an optical receiver, as shown in Fig. 15. The successful CATV transmission demonstrated that, when the performance is optimized, the polymer modulators can play a major role in the commercial communication systems.

VI. CONCLUSION

Traveling-wave M–Z and straight channel E-O modulators have been designed and fabricated based on the PUR-DR19 material. A comprehensive performance and stability test has exhibited a push–pull V_π of 11 V for M–Z devices, long-term V_π stability, and traceable dc-bias voltage. A relatively flat frequency response to ~20 GHz was measured in an M–Z modulator, and high-frequency operation up to 60 GHz was achieved in a straight channel modulator. The PUR-DR19 modulators have also been packaged with connectorized fiber input and output interface, standard 50-Ω RF ports, and a dc-bias connection. These packaged modulators have been
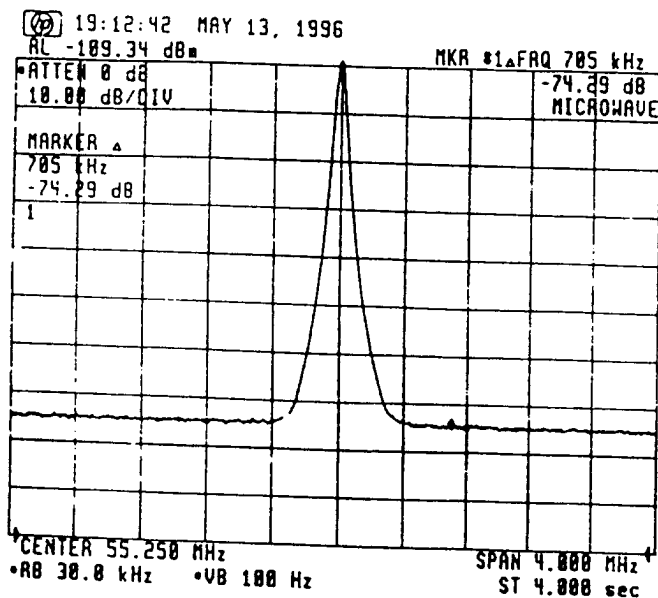
Fig. 14. A received 55.25-MHz (NTSC Channel 2) RF-signal output from an externally modulated analog link using a packaged PUR-DR19 modulator. The optical modulation index was 3.4%.
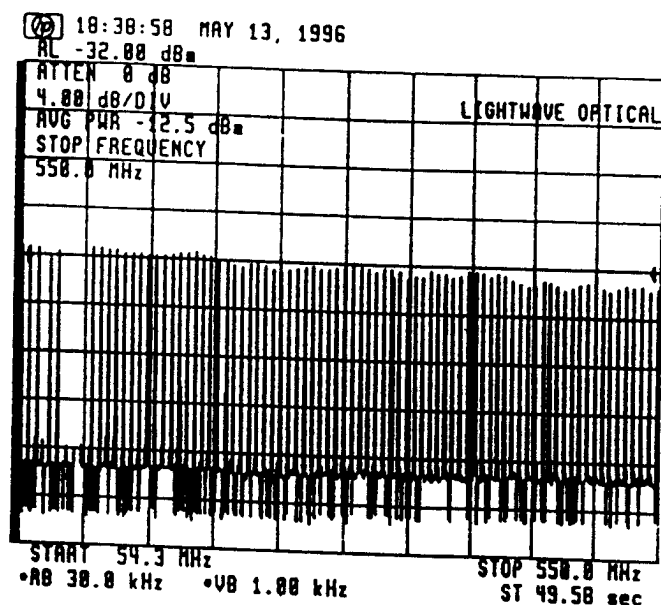

Fig. 15. Spectrum analyzer scan of 80-channel CATV signals transmitted from a PUR-DR19 E-O polymer modulator.

inserted into analog data links. A carrier-to-noise ratio of 53 dB and an 80 CATV-channel loading were obtained.

Our study on the E-O polymer modulators showed that the polymer thin film processing technology offers unique flexibility in device design and fabrication. Buried channel waveguide structures can be defined with spin-casting and reactive ion etching methods. Simple planar electrodes can be used for broad-band devices because of the small intrinsic velocity mismatch between optical and modulation waves. The device tests demonstrated that the overall performances of the E-O polymer modulators have been improved and are approaching those of crystalline materials.

Our current and future efforts will be focused on the reduction of I/O coupling loss using a better mode matching

methods and the improvement of the optical power handling capability at 1.3 μm wavelength by using a double-end crosslinked E-O polymer [31].

REFERENCES

[1] D. G. Girton, S. L. Kwiatkowski, G. F. Lipscomb, and R. S. Lytel. "20 GHz electro-optic polymer Mach–Zehnder modulator." *Appl. Phys. Lett.,* vol. 58. pp. 1730–1732. 1991.

[2] C. C. Teng. "Traveling-wave polymeric optical intensity modulator with more than 40 GHz of 3-dB electrical bandwidth." *Appl. Phys. Lett.,* vol. 60. pp. 1538–1540. 1992.

[3] R. S. Moshrefzadeh, K. M. White, C. V. Francis, M. W. Kleinschmit, S. K. Mohapatra, G. T. Boyd, R. C. Williams, K. H. Hahn, and D. W. Dolfi. "High speed optical intensity modulator in a novel polymeric material." in *Organic Thin Films for Photonic Applications.* OSA Tech. Dig. Ser.. Washington DC: Op. Soc. Amer., vol. 17. 1993. pp. 325–328.

[4] W. Wang, D. Chen, H. R. Fetterman, Y. Shi, W. H. Steier, and L. R. Dalton. "Traveling wave electro-optic modulator using crosslinked nonlinear optical polymer." *Appl. Phys. Lett.,* vol. 65. pp. 929–931. 1994.

[5] W. Wang, D. Chen, H. R. Fetterman, Y. Shi, W. H. Steier, and L. R. Dalton. "40 GHz polymer electrooptic phase modulators." *IEEE Photon. Technol. Lett.,* vol. 7. pp. 638–640. 1995.

[6] W. Wang, D. Chen, H. R. Fetterman, Y. Shi, W. H. Steier, L. R. Dalton, and P. D. Chow. "Optical heterodyne detection of 60 GHz electro-optic modulation from polymer waveguide modulators." *Appl. Phys. Lett.,* vol. 67. pp. 1806–1808. 1995.

[7] P. R. Ashley and R. J. Gulotty. "EO polymer devices for fiber optical gyroscope applications." *Polymer Preprints,* vol. 35. no. 2, pp. 215–216. 1994.

[8] Y. Shi, W. J. Swafford, J. H. Bechtel, W. H. Steier, W. Wang, D. Chen, and H. R. Fetterman. "Active polymer waveguide device for CATV and data link application: Challenges and expectations." *Polymer Preprints,* vol. 35. no. 2, p. 223. 1994.

[9] J. F. Cites, P. R. Ashley, and R. Leavitt. "Integration of nonlinear optical polymer waveguides with InGaAs p-i-n photodiodes." *Appl. Phys. Lett.,* vol. 68. pp. 1452–1454. 1996.

[10] S. Kalluri, M. Ziari, A. Chen, V. Chuyanov, W. H. Steier, D. Chen, B. Jalali, H. R. Fetterman, and L. R. Dalton. "Monolithic integration of waveguide polymer electrooptic modulators on VLSI circuitry." *IEEE Photon. Technol. Lett.,* vol. 8, pp. 644–646, 1996.

[11] K. Wong, A. K. Jen, V. P. Rao, K. J. Drost, and R. M. Mininni. "Experimental and theoretical studies of heterocyclic nonlinear optical materials." in *Proc. SPIE,* 1993, vol. 1775, pp. 74–84.

[12] V. P. Rao, K. Wong, A. K. Jen, and R. M. Mininni. "Optimization of second-order nonlinear optical properties of push-pull conjugated chromophores using heteroaromatics." in *Proc. SPIE,* 1993, vol. 2025. pp. 156–161.

[13] Y. Shuto, S. Tomaru, M. Hikita, and M. Amano. "Optical intensity modulators using diazo-substituted polymer channel waveguides." *IEEE J. Quantum Electron.,* vol. 31. pp. 1451–1460, 1995.

[14] M. Ahlheim, M. Barzoukas, P. Bedworth, M. Blanchard-Desce, A. Fort, Z. Hu, S. R. Marder, J. W. Perry, C. Runser, M. Staehelin, and B. Zesset. "Chromophores with strong heterocyclic acceptors: A poled polymer with a large electro-optic coefficient." *Science,* vol. 271. p. 335. 1996.

[15] S. Ermer, W. W. Anderson, T. E. Van Eck, D. G. Girton, J. A. Marley, A. Harwit, S. M. Lovejoy, and D. S. Leung. "Progress toward practical polymer electro-optic devices." in *Organic Thin Films for Photonic Applications.* OSA Tech. Dig. Washington DC: Opt. Soc. Amer., vol. 21. 1995. pp. 285–288.

[16] M. Chen, L. R. Dalton, L. P. Yu, Y. Shi, and W. H. Steier. "Thermosetting polyurethanes with stable and large second order optical nonlinearity." *Macromolecules,* vol. 25. pp. 4032–4035. 1992.

[17] Y. Shi, W. H. Steier, M. Chen, L. Yu, and L. R. Dalton. "Thermosetting nonlinear optical polymer: Polyurethane with Disperse Red 19 side groups." *Appl. Phys. Lett.,* vol. 60. pp. 2577–2579. 1992.

[18] R. Ulrich and H. P. Weber. "Solution-deposited thin films as passive and active light guides." *Appl. Opt.,* vol. 11. pp. 428–434. 1972.

[19] S. Kalluri, S. Garner, M. Ziari, W. H. Steier, Y. Shi, and L. R. Dalton. "Simple two slit interferometry electro-optic coefficient measurement

technique and efficient coplanar electrode poling of polymer thin films."
Appl. Phys. Lett., vol. 69, pp. 275–277, 1996.

[20] Y. Shi. Ph.D dissertation. Univ. of Southern California. Los Angeles, 1992.

[21] A. Yariv, *Introduction to Optical Electronics*. New York: Holt. Rinehart. and Winston, 1976, ch. 9.

[22] A. Chen. K. Kaviani. A. Rennple. S. Kalluri. W. H. Steier. Y. Shi. Z. Liang. and L. R. Dalton. "Optimized oxygen plasma etching of polyurethane based electro-optic polymer for low loss optical waveguide fabrication." *J. Electrochem. Soc.*, vol. 143, pp. 3648–3651, 1996.

[23] C. C. Teng. M. Mortazavi. and G. K. Boudoughian, "Origin of the poling induced optical loss in a nonlinear optical polymer waveguide." *Appl. Phys. Lett.*, vol. 66, pp. 667–669, 1995.

[24] W. H. Steier. S. Kalluri. A. Chen. S. Garner–V. Chuyanov. M. Ziari. Y. Shi, H. R. Fetterman. B. Jalali, W. Wang. D. Chen. and L. R. Dalton. "Applications of electro-optic polymers in photonics." in *MRS Symp. Proc.*, 1995, vol. 413, pp. 147–157.

[25] M. Mortazavi, K. Song. H. Yoon, and I. McCulloch. "Optical power handling of nonlinear polymers." *Polymer Preprints*, vol. 35, no. 2. pp. 198–199, 1994.

[26] Y. Shi, D. J. Olson. J. H. Bechtel. S. Kalluri. W. H. Steier. W. Wang. D. Chen, and H. R. Fetterman. "Photo excitation stability and bias stability of electro-optic polymer modulators for broadband analog transmission systems." in *Organic Thin Films for Photonic Applications*. OSA Tech. Dig. Washington DC: Opt. Soc. Amer., vol. 21, 1995, p. 325.

[27] Y. Shi, D. J. Olson, J. H. Bechtel. S. Kalluri, W. Steier, W. Wang. D. Chen, and H. R. Fetterman. "Photoinduced molecular alignment relaxation in poled electro-optic polymer thin films." *Appl. Phys. Lett.*, vol. 68, pp. 1040–1042, 1996.

[28] Y. Shi, W. Wang, and J. H. Bechtel, unpublished test results.

[29] H. Nagata and J. Ichikawa, "Progress and problems in reliability of Ti:NbO₃ optical intensity modulators." *Opt. Eng.*, vol. 34, pp. 3284–3293, 1995.

[30] L. Altwegg. "Properties of polymeric Mach–Zehnder modulators." *Opt. Eng.*, vol. 34, pp. 2651–2656, 1995.

[31] C. Xu, B. Wu, L. R. Dalton. Y. Shi. P. M. Ranon, and W. H. Steier. "Novel double-end cross-linkable chromophores for second-order nonlinear optical materials." *Macromolecules*, vol. 25, pp. 6714–6715, 1992.

James H. Bechtel received the B.S. degree in physics, magna cum laude, from Miami University, Oxford, OH, in 1967, and the M.S. and Ph.D. degrees in physics from the University of Michigan, Ann Arbor, in 1968 and 1973, respectively.

From 1973 to 1976, he was a post-doctoral Research Fellow at Harvard University, Cambridge, Massachusetts and conducted research in nonlinear optics and picosecond laser pulse technology. From 1976 to 1983, he was with General Motors Research Laboratories, Warren, MI, where he performed research in chemical and optical physics. During 1982, he was a Visiting Scientist at the Department of Electrical Engineering and Computer Science of the Massachusetts Institute of Technology, Cambridge, Massachusetts. Since 1983, he has been with TACAN Corporation where he is currently Senior Vice President and responsible for research, analog and digital engineering, optoelectronic packaging, business development, and government affairs.

Dr. Bechtel is a fellow of the Optical Society of America and a member of numerous other technical organizations.

Antao Chen received the B. Eng. and M. Eng. degrees in 1983 and 1989, respectively, both from Beijing Institute of Technology, China, M.S. degree from the University of Southern California in 1994, and is working towards the Ph.D. degree from the University of Southern California.

He was an optical system designer in State Northwestern Optical Instrument Plant from 1983 to 1986 and an engineer in the Chinese Academy of Electronics and Information Technology from 1989 to 1993.

Sean Garner (S'95) was born February 5, 1971, in Racine, WI. He received the B.E. degree in engineering physics from Stevens Institute of Technology in Hoboken, NJ, and the M.E. degree in electrical engineering from the University of Southern California in 1993 and 1994, respectively, and is currently pursuing the Ph.D. degree in electrical engineering from the University of Southern California.

Mr. Garner is a member of OSA.

Yongqiang Shi was born in Nantong, China, in 1958. He received B.S. and M.S. degrees in physics from Suzhou University and Hangzhou University, China, in 1982 and 1984, respectively, and the Ph.D. degree in electrical engineering from the University of Southern California, Los Angeles, in 1992.

He worked as an instructor in the Physics Department at Hangzhou University from 1984 to 1986. After his postdoctorial work in the Department of Electrical Engineering at USC, he joined TACAN Corporation as a Staff Scientist in charge of current nonlinear optical polymer device programs. He has broad interests in integrated optics, nonlinear optics, and optical communications. His current research includes nonlinear optical materials characterizations, device fabrication, and their applications in photonic systems.

Srinath Kalluri received the B.S.E.E. degree from the University of Massachusetts, Lowell, in 1990, the Masters degree from the University of Southern California, Los Angeles, in 1992, and is working towards the Ph.D. degree in electrical engineering from USC.

His current interests are in nonlinear optical materials and devices.

Wenshen Wang (S'93–M'95) was born in Xi'an, Shaanxi, China in 1958. He received Bachelor of Engineering and Master of Engineering degrees in radio electronics from Tsinghua University, Beijing, China, in 1983 and 1986 respectively, and Ph.D. degree in electrical engineering from the University of California at Los Angeles in 1995.

He joined TACAN Corporation at Carlsbad, California in 1995, as a Staff Scientist working on research and development of novel RF photonics technologies and their applications in optical communication systems, in particular, CATV systems. He has been engaged extensively in the research and development of state-of-the-art integrated polymer photonic devices including broadband electro-optic modulators, integrated photonic switches, and waveguide delay lines, as well as their applications in fiber-optic data links and phased array antenna feeds.

William H. Steier (S'58–M'60–SM'72–F'76) received the B.S.E.E. from the University of Evansville and the M.S.E.E. and the Ph.D. from the University of Illinois, Urbana.

He is the W. M. Hogue Professor of Electrical Engineering at the University of Southern California. From 1962 to 1968, he was a member of the Technical Staff at Bell Telephone Laboratories. He and his students have published in the areas of millimeter and submillimeter wave electronics, optical modulators, optical resonators, and optical guiding structures. In recent years, his research group has had a successful research effort in multiple quantum-well semiconductor optical switches and amplifiers and in photorefraction in semiconductors and its applications to optical computing. He has recently collaborated with the chemistry faculty to investigate polymer nonlinear optical materials and devices. He has held several administrative positions at USC including Department Chair. He is currently the Director of the USC Joint Service Electronics Program and a Co-principal Investigator for the National Center for Integrated Photonic Technology.

In 1994, he was elected a fellow of the America Optical Society.

Datong Chen (S'91) was born in Zhejiang, China, in 1967. He received the B.S. degree in physics from Fudan University, China, in 1989, and an M.S. degree in physics from Northwestern University, Evanston, IL, in 1990, and is working towards the Ph.D. degree at University of California, Los Angeles.

He has been a Research Assistant in Electrical Engineering Department at University of California, Los Angeles. His current research interests focus on developing high-speed electrooptic polymer modulators, which includes computer aided design and modeling of millimeter-wave and microwave circuit and optical waveguide, device fabrication, and high frequency characterization of the modulator.

Harold R. Fetterman (SM'81–M'90) received the B.A. in physics from Brandeis University in 1962 and the Ph.D. degree from Cornell University in 1967.

After joining Lincoln Laboratory at MIT, he began to investigate new solid-state high-frequency devices. This included FET's, HEMT's, and HBT's, quantum-well structures, and resonant tunneling structures. In 1982, he joined the UCLA Electrical Engineering Department as a Professor and first Director of the Center for High Frequency Electronics. During this period, he also became active in studying Optoelectronics and optical control of millimeter wave devices. Currently, he has programs in investigating new polymer optical modulators, millimeter wave device concepts, and novel means of testing using laser techniques. He has helped organize many new activities including the Optically Controlled Phased Array Radar Project in the National Center for Integrated Photonics.

Larry R. Dalton received the B.S. degree in 1965 from the Honors College of Michigan State University and the Ph.D. degree in chemistry from Harvard University in 1971.

He is currently the Harold and Lillian Moulton Professor of Chemistry and Professor of Materials Science and Engineering at the University of Southern California, Los Angeles. He also serves at Co-Director of the Loker Hydrocarbon Research Institute and Director of the Center for Nanoscale Materials and Processing at USC. He conducts and directs research focusing on nonlinear optical and magnetic resonance phenomena and on the intermolecular forces which control the organization of molecules over nano- and microscale dimensions. Research in the area of nonlinear optical materials includes the development of organic second-order nonlinear optical polymers appropriate for the fabrication of electrooptic modulator devices.

Luping Yu, photograph and biography not available at the time of publication.

Monolithic Integration of Waveguide Polymer Electrooptic Modulators on VLSI Circuitry

Srinath Kalluri, Mehrdad Ziari, *Member, IEEE,* Antao Chen, Vadim Chuyanov, William H. Steier, *Fellow, IEEE,* Datong Chen, Bahram Jalali, *Member, IEEE,* Harold Fetterman, *Fellow, IEEE,* and Larry R. Dalton

Abstract—We demonstrated some of the critical technology that is needed for the monolithic integration of polymer electrooptic modulators and VLSI circuitry by fabricating and testing a phase slab modulator on nonplanar VLSI circuits. We demonstrated the survival of GaAs MESFET's to the high-voltage poling and polymer modulator fabrication procedures. We also implemented an electrical interconnect scheme between the electronics and photonics layers.

POLYMER electrooptic (EO) materials have two significant and unique advantages for device applications in opto-electronic systems. First, the low dispersion in the index of refraction of polymers, from the infrared to millimeter wave region of the electromagnetic spectrum, permits traveling wave infrared modulators to operate at very high modulation frequencies ($>$100 GHz) with relatively long interaction lengths ($\sim$1 cm) [1], [2]. Second, their flexibility for device processing makes it possible to monolithically integrate EO polymer devices with semiconductor electronics to achieve robust and low cost high speed opto-electronics. For example, the spin casting method of depositing multilayer polymer thin films can be used to fabricate active EO polymer devices directly on top of pre-processed silicon or III–V signal processing and drive electronics. In contrast, monolithic integration of alternative crystalline EO materials such as $LiNbO_3$ on semiconductor electronics is very difficult. Guided-wave structures such as waveguides, bends, and couplers have been demonstrated in polymers using standard microfabrication technology [3]. In addition, polymers offer the potential advantages of molecular engineering, where the electrical and optical properties can be tailored by organic synthesis, and large EO coefficients and low drive voltages may be possible by the incorporation of molecules with large NLO effects [4].

There are several potential applications for integrated polymer-semiconductor optoelectronics. Optical communication network architectures such as deflection routing or the "hot potato" network [5], require smart switching nodes. In these systems, the address of an incoming packet is detected and recognized and the node switches the packet accordingly. The polymer-Si optoelectronics technology would enable the detection, recognition electronics, and the optical switch to be integrated on a single substrate. In addition, for emerging CATV applications where linearity and stability are critical issues, one can integrate bias point stability and signal pre-distortion electronics on the same chip as the EO modulator.

Of the many architectures possible for polymer optoelectronics [6], we have chosen a vertical integration approach. Here, the polymer device is integrated directly above the electronic devices with a thick intermediate dielectric layer for isolation and planarization. Vias etched in this planarization layer will provide the electrical interconnection pathways. One example where this approach has been used is for the integration of etalon modulators on logic circuitry [7]. Our monolithic polymer-Si integration approach is also compatible with the Si optical breadboard concept where v-groove technology is used to align the fiber inputs and outputs [8], [9]. The success of any polymer-Si integration scheme depends on several key issues. For example, the effectiveness of the planarization process is critical for vertical integration since this determines the quality of the fabricated devices. Simple schemes to implement the interconnection pathways must also be found. The effect of the active polymer device fabrication process—such as high voltage poling—on the degradation of the underlying electronics must be studied. Solutions to these issues are demonstrated in this letter. In earlier work, we reported on our progress toward the v-groove coupling of single mode fibers to the on-chip polymer devices [9].

Optical waveguides must be fabricated on smooth surfaces. This requirement places strict constraints on the quality of optical substrates. Roughness on the substrate translates to the waveguides and results in large optical scattering losses. Therefore, effective global planarization of the surface topology of the Si circuits is critical for the success of the vertical integration scheme. EO polymers, cladding polymers, photoresists, and so forth have a limited capability for large area planarization. The PC3-6000 (Futurrex) planarizing polymer works well in this application, since it is quite viscous compared to the photoresist type of polymer and achieves

S. Kalluri, A. Chen, V. Chuyanov, and W. H. Steier are with the Department of Electrical Engineering, University of Southern California, Los Angeles, CA 90089-0483 USA.

M. Ziari is with SDL, Inc., 80 Rose Orchard Way, San Jose, CA 95134 USA.

D. Chen, B. Jalali, and H. Fetterman are with the Department of Electrical Engineering. University of California, Los Angeles, CA 90024 USA.

L. R. Dalton is with the Department of Chemistry, University of Southern California, Los Angeles, CA 90089-1062 USA.
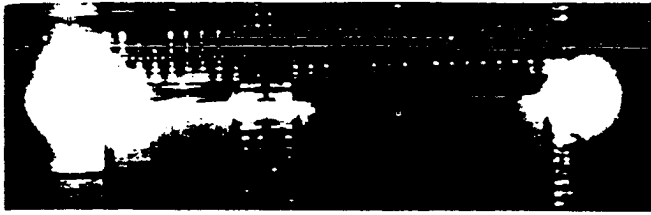Publisher Item Identifier S 1041-1135(96)03600-2.

Fig. 1. Photograph of prism incoupled (bright spot on left) and outcoupled light (bright spot on right) from slab waveguide fabricated on planarized VLSI circuits. The underlying circuits can also be seen clearly. The distance between prisms is approximately 1 cm.

some degree of planarization directly after spinning. Moreover, at elevated temperatures (200 °C), the material reflows from the peaks to the troughs and thus further smoothens out the topology. The features on the Si circuits in Fig. 1 were 1 μm to 6 μm high before planarization and less than 0.2 μm high after planarization [6]. We have successfully planarized more than 3 cm^2 areas of the substrate. A good test for the quality of the planarization for photonics applications is to make propagation loss measurements for waveguides fabricated on these "optical" substrates. A slab waveguide structure fabricated on a planarized substrate and consisting of an epoxy lower cladding and a higher index polymer guiding layer demonstrated low loss propagation (Fig. 1). The waveguide loss measured at the 1.06-μm wavelength, using prism coupling and the scattering-detection method [10] was less than 1 dB/cm, which is the resolution limit of our loss set-up. Moreover, loss measurements performed on similar waveguides fabricated on polished Si substrates yielded comparable results.

A demonstration phase modulator was fabricated and tested on the planarized circuits. The structure of the fabricated slab modulator is shown in the inset of Fig. 2. Polymer layers were spin coated and metal layers were evaporated [6]. The PUDR19 EO polymer layer, shown in the figure, was high voltage corona poled to induce the noncentrosymmetry required for $\chi^{(2)}$ properties. From previous measurements, we estimate an r_{33} of 13 pm/V (at 1.3 μm) after corona poling [11]. After poling, this layer was capped by a thin (0.2 μm) polysiloxane spin on glass (SOG) layer that acts as an etch stop during subsequent oxygen plasma etching. Since this layer is a fraction of the thicknesses of the other polymer layers (claddings are ~5 μm thick, PUDR19 is ~1 μm thick), it does not significantly affect the modulation field in the active layer. Furthermore, we suspect that our nonthermal procedure (we use an O$_2$ plasma) for curing/setting SOG [6], makes its conductivity comparable to the other polymers. The gold upper electrode was 0.5 cm long and 0.2 μm thick. The device was tested in an external Mach–Zehnder interferometer at the 1.06 μm wavelength. The ac component of the recombined light from the interferometer was measured. The upper trace in Fig. 2 shows the applied voltage signal at 1 kHz. The lower trace shows the detected intensity modulation signal. The figure shows that there was no modulation when either arm of the interferometer was blocked and a strong modulation signal was seen when light was allowed to recombine and interfere. The variation in amplitude of the modulated signal
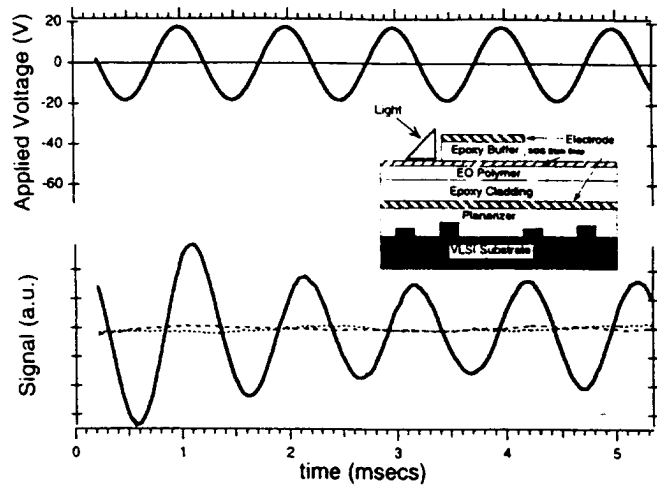

Fig. 2. Polymer slab modulator testing results. Upper curve is applied ac voltage. Lower curve (solid line) shows detected modulation intensity. Dashed curves show modulation intensity when either arm of interferometer is blocked. (Inset): Cross-section schematic of fabricated multilayer polymer slab modulator.

seen in the figure is due to the instability of the interference pattern. This experiment demonstrates that devices such as the 60 GHz channel phase modulator [1] (which used the same material systems and fabrication procedures) can be easily integrated.

To orient the molecular dipoles in the polymer matrix dc fields exceeding 200 V/μm (corona poling) are often used. Therefore, degradation of the electronics during the poling and modulator fabrication processes is a serious concern. The sensitivity of electronic circuits to these processes was tested by subjecting GaAs MESFET's to various device fabrication procedures such as, poling, planarizing and RIE etching. The circuits were planarized at 200 °C and then coated with a film of water soluble polyvinylalcohol (PVA), Cr metal and polymer. The metal layer is necessary for microstrip line electrode geometry modulators and functions both as a ground plane for subsequent poling and as a shielding layer for the underlying electronics. A corona poling profile typical for most of our device polymers, 140 °C for 45 minutes and corona needle voltage of 6 kV, was used to simulate the poling conditions. After the PVA, metal and poled polymer layers were removed in de-ionized water, the substrate was transferred to a RIE chamber where the planarizing polymer was etched off in an O$_2$ plasma. The plasma etching parameters were: 150 W RF power, 200 mTorr O$_2$ pressure and 15 minutes etch time. These parameters are more than adequate for the etching requirements of normal polymer ridge waveguide fabrication [3]. For samples where the metal ground plane was not deposited and the ground contact was made directly on the GaAs substrate, complete degradation of the MESFET devices was seen [Fig. 3(a)]. On the other hand, devices where the metal ground plane protection was used showed no degradation after the poling and fabrication processes [Fig. 3(b)].

Electrical interconnections between the electronics and the photonics (modulator) planes require vias fabricated through the various layers. These vias need to penetrate through a
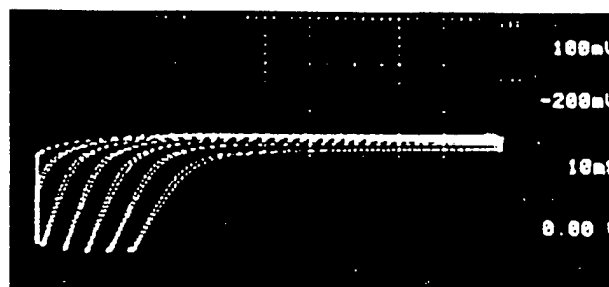
(a)
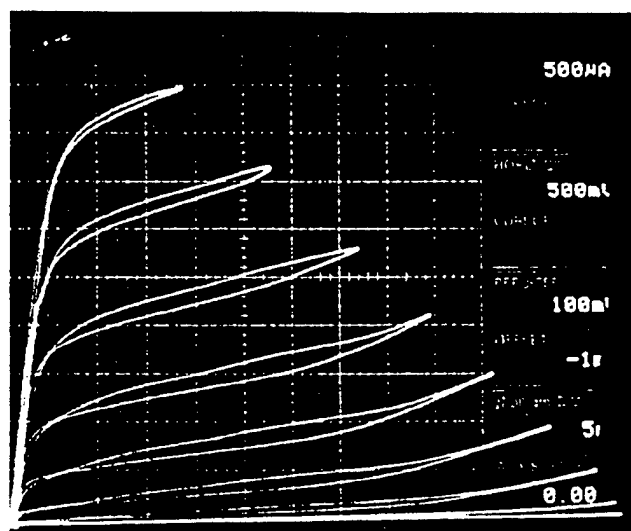
(b)

Fig. 3. Protection of GaAs MESFET's during polymer high voltage poling and device fabrication procedures. (a) I-V of device placed in poling stage without the protection of a ground plane is shown and indicates complete degradation. (b) Device whose I-V is shown was protected with a metal ground plane and shows no degradation after poling/fabrication procedure.

Fig. 4. Schematic of test structure to demonstrate one possible scheme for realizing vertical electrical interconnects.

very thick (>6 μm) layer of polymer planarizing material and since the photoresists used to lithographically define the masks for these vias are also polymers, the RIE O_2 plasma etch selectivity between these two polymer materials is very poor. Therefore, techniques for transferring patterned vias in photoresist to underlying polymer layers were investigated. One method is to use a simple trilayer processing technique. Here, a thin intermediate RIE barrier layer is used to transfer a pattern defined in a thin layer of photoresist to the thick planarizing layer. The main feature of this technique is that the intermediate layer and the photoresist/planarizer layers each etch in a different reactive ion gas plasma species. A cross-section diagram of the test structure designed to demonstrate the viability of this interconnection scheme is shown in Fig. 4. First, the metal areas A and B were defined on a glass substrate and coated with the thick planarizing polymer layer, SOG layer and photoresist. As a barrier material, SOG (Futurrex) provides the most processing flexibility. The excellent O_2 etch selectivity between this material and organic polymers is due to the high Si content of the cured SOG. An array of small rectangular holes were defined in the photoresist, and CF_4 plasma was used to etch the SOG intermediate layer with this photoresist mask. Subsequently, an O_2 plasma was
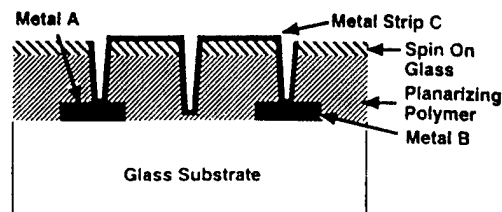
used to pattern the underlying planarizer (SOG is now the mask). Finally, metal patch C was defined by shadow masking. Continuity measurements before and after the second metal evaporation indicate that the two initially isolated metal areas A and $\overline{B}$ are now connected by metal patch C. This technique is compatible with the fabrication of practical active polymer devices since it is possible to process SOG at low temperatures [6] and since only standard resists and processing techniques were used.

In summary, we demonstrated for the first time, a polymer electrooptic waveguide modulator monolithically integrated on nonplanar VLSI circuits. We also demonstrated the survival of GaAs MESFET's to the polymer poling and device fabrication procedures. Finally, we proposed and demonstrated a trilayer processing scheme for performing interconnects between the photonics and electronics layers.

REFERENCES

[1] W. Wang, D. Chen, H. R. Fetterman, Y. Shi, J. H. Bechtel, S. Kalluri, W. H. Steier, and L. R. Dalton, "60 GHz electro-optic modulation from polymer waveguide phase modulators," presented at Organic Thin Films for Photon. Applicat. Conf., Portland, OR, 1995.

[2] Y. Shuto, S. Tomaru, M. Hikita, and M. Amano, "Optical intensity modulation using diazo-dye-substituted polymer channel waveguides," IEEE J. Quantum Electron., vol. 31, pp. 1451–1460, 1995.

[3] W. H. Steier, Y. Shi, P. M. Ranon, C. Xu, B. Wu, and L. R. Dalton, "Waveguide photonic devices made from thermally crosslinked second-order nonlinear optical polymers," presented at Nonlinear Optical Properties of Organic Mater. VI, San Diego, CA, 1993.

[4] Y. M. Cai and A. K.-Y. Jen. "Thermally stable poled polyquinoline thin film with very large electro-optic response," Appl. Phys. Lett., vol. 67, pp. 299–301, 1995.

[5] D. J. Blumenthal, P. R. Pruncal, and J. R. Sauer, "Photonic packet switches: Architectures and experimental implementations," Proc. IEEE, vol. 82, pp. 1650–1667, 1994.

[6] S. Kalluri, A. Chen, V. Chuyanov, M. Ziari, W. H. Steier, and L. R. Dalton, "Integration of polymer electrooptic devices on nonplanar silicon integrated circuits," presented at Nonlinear Optical Properties of Organic Mater. VIII, San Diego, CA, 1995.

[7] S. T. Kowel, S. Wang, A. Thomsen, W. Chan, T. M. Leslie, and N. P. Wang, "High field poling of electrooptic etalon modulators on CMOS integrated circuits," IEEE Photon. Technol. Lett., vol. 7, pp. 754–756, 1995.

[8] C. A. Armiento, A. J. Negri, M. J. Tabasky, R. A. Boudreau, M. A. Rotham, T. W. Fitzgerald, and P. O. Haugsjaa, "Gigabit transmitter array modules on silicon waferboard," IEEE Trans. Comp. Hybrids and Manuf. Technol., vol. 15, pp. 1072–1079, 1992.

[9] M. Ziari, A. Chen, S. Kalluri, W. H. Steier, Y. Shi, W. Wang, D. Chen, and H. R. Fetterman, "Polymer electrooptic waveguide fabrication," in Nonlinear Optical Polymers: From Molecules to $\chi^{(2)}$ Applications, G. A. Lindsay and K. D. Singer, Eds. (ACS Symp. Series), pp. 420–435, 1995.

[10] H. Nishihara, M. Haruna, and T. Suhara, Optical Integrated Circuits. 1st ed. New York: McGraw-Hill, 1985.

[11] Y. Shi, W. H. Steier, M. Chen, L. P. Yu, and L. R. Dalton, "Thermosetting nonlinear optical polymer: Polyurethane with disperse red 19 side groups," Appl. Phys. Lett., vol. 60, pp. 2577–2579, 1992.

Integration of Polyimide Waveguides with Traveling-Wave Phototransistors

D. P. Prakash, D. C. Scott, *Student Member, IEEE*, H. R. Fetterman, *Fellow, IEEE*,
M. Matloubian, *Member, IEEE*, Q. Du, and W. Wang

Abstract— Polymer waveguides with low optical losses are becoming increasingly important for photonic circuits. Among these, polyimide waveguides have properties which distinguish them as a versatile interconnect medium for practical optoelectronic integrated circuits. We have integrated these waveguides with traveling-wave phototransistors (TW-HPT's) in which optical power transfer occurs through leaky mode coupling of light from the waveguide along the length of the device. Independent optimization of the waveguide and phototransistor is now possible permitting superior coupling efficiency and detector bandwidth. We present proof-of-concept results for a 2-mm-long TW-HPT integrated with a 8×10-μm polyimide waveguide.

Index Terms— Heterojunction bipolar transistors, optical interconnections, phototransistors, polymide films, traveling-wave devices, waveguides.

I. INTRODUCTION

POLYMER waveguides are being developed for use as optical interconnects in photonic circuits [1]. Polyimide waveguides in particular, because of their versatile characteristics, are finding widespread use in wafer scale applications [2]. In our previous work, we have used on-wafer polyimide waveguides and have demonstrated their bandwidth up to 50 GHz [3]. Discrete optoelectronic circuits were used in these experiments with butt coupling from waveguide to the optical detector. In such hybrid optoelectronic configurations, there is an inherent tradeoff between optical coupling efficiency and the detector bandwidth [4]. Furthermore, detectors illuminated vertically also tend to saturate at low optical powers. The central concern of our current work is to explore, using integrated polyimide waveguides, a horizontal coupling scheme to overcome these problems. Polyimide waveguides have been defined directly on the base and collector mesas of a traveling-wave optical device—the traveling-wave heterojunction phototransistor (TW-HPT). The optical power in these devices is coupled through leaky modes along the length of the device. We have demonstrated the viability of the leaky mode coupling concept experimentally and present preliminary results from

prototype devices including the frequency response up to 20 GHz.

II. COMPARISON OF INTERCONNECT TECHNOLOGIES

Several interconnect technologies are currently available including all-glass [5], silicon-on-insulator [7], and InGaAsP on InP [7]. While these technologies have their merits and find specific applications, they have yet to satisfy the basic requirements needed for wafer scale integration. An ideal on-wafer interconnect: 1) has low input coupling loss when butt coupled from a fiber; 2) has low propagation losses when routing light; 3) incorporates passive single/multimode waveguiding elements for functionality: 4) integrates well with electrooptic modulators; and 5) couples efficiently into photodetectors. Polyimide waveguides have the capacity to satisfy these requirements of ideal interconnects and are also both rugged and durable.

Glass waveguides have the best input coupling losses of 0.1 dB per connection and low absorption losses of 0.05 dB/cm [5]. Although this technology is excellent for passive optical circuits, it is not suitable for integration with active devices. Rib waveguides made with silicon on insulator (SOI) are attractive because of established silicon processing techniques. However, single mode propagation is generally not easily obtainable and losses tend to be high [6]. Optical detectors at 1.3–1.55 μm are not available in silicon and therefore restrict the scope of this technology. InGaAsP quaternary waveguides can be integrated with active devices such as p-i-ns and phototransitors [7], but crystal growth techniques place a limitation on the maximum thickness of the waveguide to 0.5–0.7 μm. This again results in poor mode matching from a fiber input and therefore substantial insertion losses. Also, high-speed electrooptic modulators have yet to be demonstrated in the material systems described above. Polyimides, a class of polymers, are an outstanding alternative. Excellent input coupling between fiber and waveguide can be achieved [8]. Polyimides have very low material losses of 0.09 dB/cm [9], which is among the best reported in the literature. Passive polyimide waveguide structures such as delay elements, power splitters/combiners and repetition rate multipliers have been extensively examined [3]. Recently, polymer modulators with bandwidths in excess of 100 GHz have been demonstrated [10]. Through serial grafting techniques [11], polyimide waveguides are ideally suited for integration with such high bandwidth polymer modulators.
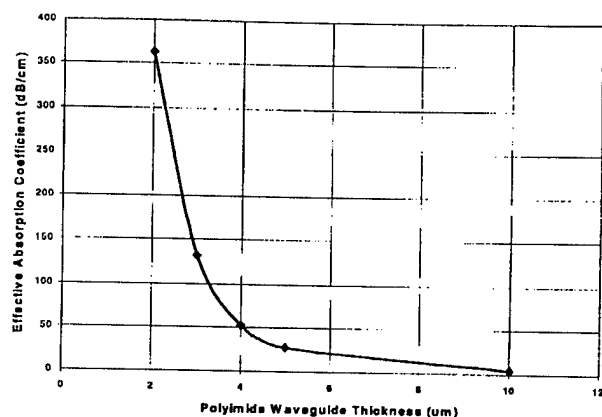
Fig. 1. Simulations of effective absorption coefficient versus polyimide waveguide thickness on InGaAs at 1.3 μm.
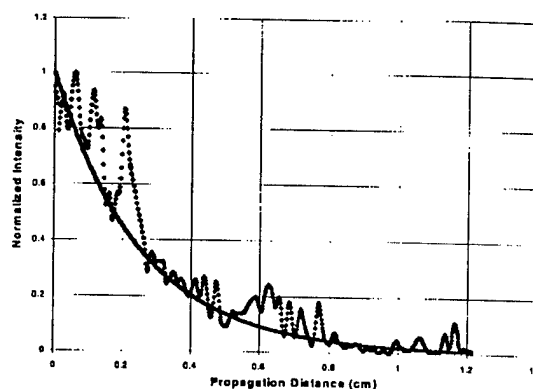

Fig. 2. Experimental verification of leaky-mode coupling using 7-μm-thick polyimide waveguide on InGaAs. Points represent actual measurement data. Solid line is an exponential fit to the data. Effective absorption coefficient measured to be 17 dB/cm.

III. INTEGRATION WITH TRAVELING-WAVE HETEROJUNCTION BIPOLAR TRANSISTORS

To investigate the potential of polyimide waveguides for efficient optical coupling to active devices, we propose to utilize the traveling-wave concepts that have been implemented so successfully in optical modulator technology [10] and extend these concepts to optical detectors. In our approach, we define a leaky-mode polyimide waveguide on top of the active region of the optical detector. Intensity modulated light is coupled into the polyimide waveguide and leaks into the detector's active region along the length of the device due to the fact that the index of refraction of the semiconductor is higher than that of the polyimide. A microwave signal is generated on the transmission line as light is absorbed by the detector. The bandwidth limitation of such a device is based on the velocity mismatch between the optical wave and the induced electrical microwave [12].

In our traveling-wave approach, the optical absorption can be optimized without degrading the bandwidth. The rate at which the light couples to the device and is absorbed can be described by an effective absorption coefficient and can be adjusted by varying the dimensions of the polyimide waveguide. Therefore, we expect superior coupling efficiency and bandwidth from a waveguide-fed TW-HPT.

To investigate this concept, we used a simulation program by Rsoft, Inc., called BeamProp which is based on the beam propagation method. We simulated structures consisting of polyimide waveguides of various thicknesses on top of $In_{0.53}Ga_{0.47}As$ to extract the effective absorption coefficient at an optical wavelength of 1.3 μm. The index of refraction of the polyimide and InGaAs was 1.52 and 3.368, respectively. The results are shown in Fig. 1 and demonstrate the large range of control over the effective absorption coefficient which leads to design flexibility for varying the length of the detector to achieve optimal optical absorption.

To verify our concept of leaky mode coupling, we coupled light of 1.06-μm wavelength into a 7-μm-thick by 5-μm-wide polyimide waveguide patterned on $In_{0.53}Ga_{0.47}As$. The effective absorption coefficient was determined by measuring the loss/cm using a CCD camera. The results are
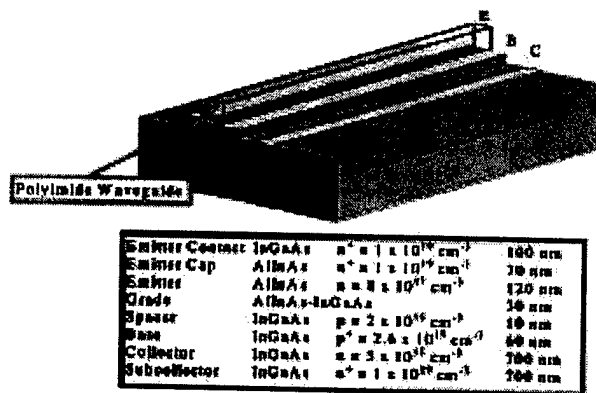

Fig. 3. Device layer structure and diagram of TW-HPT showing polyimide waveguide defined on top of the base mesa.

shown in Fig. 2 and yield an effective absorption coefficient of 17 dB/cm, which agrees well with our simulations.

IV. FABRICATION OF WAVEGUIDE-FED TW-HPT

The fabricated prototype device is shown in Fig. 3. The phototransistor was fabricated first based on an HBT layer structure and then the waveguides were patterned. The device consists of 2-mm-long coupled microstrip lines with electrode widths of 20 μm and separation between lines of 15.11 μm designed for 50-Ω characteristic impedance. On both ends of the device area, the electrodes flare out to dimensions that are compatible with 100-μm-pitch coplanar probes.

In defining polyimide waveguides, we have found it convenient to use Amoco's Ultradel 9120D photoimageable polyimide. Waveguides with smooth and vertical sidewalls were easily achieved using standard photolithography. The polyimide curing was done at a low temperature of 175 °C for 120 min to reduce the possibility of beryllium diffusion from the base to the emitter. The devices were cleaved at liquid nitrogen temperatures to achieve good optical end faces on the polyimide waveguides.
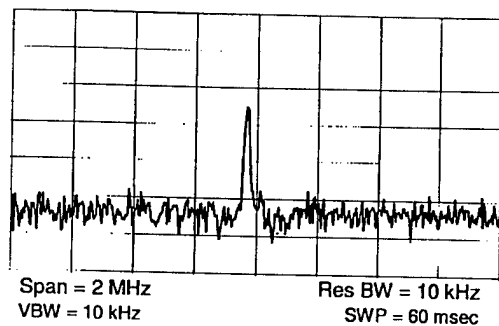
Span = 2 MHz Res BW = 10 kHz
VBW = 10 kHz SWP = 60 msec

Fig. 4. Spectrum analyzer trace of the 20-GHz optically generated signal with 25-dB SNR. Incident total laser power was 2 mW.

V. EXPERIMENTAL RESULTS AND DISCUSSION

To measure the dc-optical gain of the TW-HPT, light at 1.3-μm wavelength from a single-mode optical fiber was butt coupled to the polyimide waveguides. The response of the TW-HPT varied depending on which optical waveguide was used. When injecting into the bottom waveguide, which is defined on the subcollector, no optical gain was observed. The authors attribute this to the fact that the absorption of light in the subcollector does not effectively change the base-emitter junction potential [13]. However, when light was injected into the top waveguide, which was defined on top of the base, we measure an optical gain of 4.5. The fact that this number is greater than 1 shows the appreciable advantage that HBT based detectors can have over conventional p-i-n detectors. The optical gain can be improved in future generation devices by mode matching the optical waveguide to the input optical fiber and by optimizing the effective absorption coefficient to the device length to obtain >90% absorption. Presently, we estimate our input coupling loss to be −4.2 dB and our absorption efficiency to be 50%.

Preliminary measurements of the TW-HPT show good frequency response up to 20 GHz with a signal-to-noise ratio (SNR) of 25 dB as indicated in Fig. 4. The frequency response of the device was measured using optical heterodyning of two-tunable diode pumped YAG lasers at 1.3 μm [13]. The bandwidth is currently limited by velocity mismatch, microwave propagation loss, and poor impedance matching to the external circuit. Based on our simulations, the effective index of the microwave transmission line is $n_{mic} = 2.6$ and the effective index of the optical wave is $n_{opt} = 1.68$. Ignoring the effects of dispersion, this velocity mismatch limits the theoretical maximum frequency response of our device to 4 GHz·cm. In our case, the optical wave travels faster than the electrical wave. One method for reducing the velocity of the optical beam is by defining gratings in the polymer waveguide which can effectively slow down the k-vector of the optical wave. Optical gratings in polymer waveguides have been successfully demonstrated by B. L. Volodin et al. [14]. The full theoretical model and computer simulations of the performance of the TW-HPT will be presented in a subsequent publication.

VI. CONCLUSION

We envision widespread applications of polymer waveguide technology in future photonic and optoelectronic integrated circuits. To integrate polyimide waveguides with detectors, we have explored the concept of leaky mode coupling along the length of a suitable traveling-wave device—the TW-HPT. A prototype device was fabricated with polyimide waveguides defined on the base and collector mesas of a TW-HPT. The leaky mode coupling concept was experimentally verified and shown to be viable. Preliminary results of the waveguide-fed TW-HPT, including a frequency response up to 20 GHz, are presented and discussed. Future work includes the use of slow wave structures in the polyimide waveguide for velocity matching and the design of broad-band, low-loss, matched microwave transmission lines.

REFERENCES

[1] B. L. Booth, "Low loss channel waveguides in polymers," *J. Lightwave Technol.*, vol. 7, pp. 1445–1453, Oct. 1989.
[2] H. R. Fetterman, D. P. Prakash, D. C. Scott, and W. Wang, "Integrated optically driven microwave/millimeter wave device structures," in *IEEE MTT-S Int. Microwave Symp. Dig.*, May 1994, vol. 3, pp. 1493–1496.
[3] D. P. Prakash, D. V. Plant, D. Zhang, and H. R. Fetterman, "Optical transmission of millimeter wave signals through polyimide channel waveguides fabricated using direct laser writing," in *SPIE, Nonconducting Photopolymers and Appl.*, July 1992, vol. 1774, pp. 118–129.
[4] R. J. Deri, "Monolithic integration of optical waveguide circuitry with III–V photodetectors for advanced lightwave receivers," *J. Lightwave Technol.*, vol. 11, pp. 1293–1313, Aug. 1993.
[5] Product Literature, Photonic Integration Research Inc., Columbus, OH, 1996.
[6] A. G. Rickman, G. T. Reed, and F. Namavar, "Silicon-on-insulator optical rib waveguide loss and mode characteristics," *J. Lightwave Technol.*, vol. 12, pp. 1771–1776, Oct. 1994.
[7] P. Freeman, X. Zhang, I. Vurgaftman, J. Singh, and P. Bhattacharya, "Optical control of 14 GHz MMIC oscillators based on InAlAs/InGaAs HBT's with monolithically integrated optical waveguides," *IEEE Trans. Electron Devices*, vol. 43, pp. 373–379, Mar. 1996.
[8] A. Chen, V. Chuyanov, F. I. Marti-Carrera, S. Garner, W. H. Steir, J. Chen, S. Sun, and L. R. Dalton, "Integrated polymer waveguide mode size transformer with a vertical taper for improved fiber coupling," in *SPIE Proc.*, to be published.
[9] Ultradel 9120D Bulletin, Amoco Chemical Company, Naperville, IL.
[10] D. Chen, H. R. Fetterman, A. Chen, W. H. Steir, L. R. Dalton, W. Wang, and Y. Shi, " High-bandwidth polymer modulators," in *SPIE*, vol. 3006, pp. 314–317, Feb. 1997.
[11] T. Watnabe, M. Amano, M. Hikita, Y. Shuto, and S. Tomaru, "Novel 'serially grafted' connection between functional and passive polymer waveguides," *Appl. Phys. Lett.*, pp. 1205–1207, Sept. 1994.
[12] V. M. Hietala, G. A. Vawter, T. M. Brennan, and B. E. Hammons, "Traveling-wave photodetectors for high-power, large-bandwidth applications," *IEEE Trans. Microwave Theory Tech.*, vol. 43, pp. 2291–2297, Sept. 1993.
[13] D. C. Scott and H. R. Fetterman, "Millimeter wave generation using InP HBT phototransistors," in *InP HBTs: Growth, Processing, and Applications*, B. Jalali and S. J. Pearton, Eds. Boston, MA: Artech House, 1995, ch. 10.
[14] B. L. Volodin, B. Kippelen, K. Meerholz, N. V. Kukhtarev, H. J. Caulfield, and N. Peyghambarian, "Non-Bragg orders in dynamic self-diffraction on thick phase gratings in a photorefractive polymer," *Opt. Lett.*, vol. 21, no. 7, pp. 519–521, 1996.

High-Power High-Frequency Traveling-Wave Heterojunction Phototransistors with Integrated Polyimide Waveguide

D. C. Scott, D. P. Prakash, H. Erlig, D. Bhattacharya, M. E. Ali,
H. R. Fetterman, *Fellow, IEEE,* and M. Matloubian, *Member, IEEE*

Abstract—A high-power high-speed phototransistor has been demonstrated using a traveling-wave (TW) structure with an integrated polyimide optical waveguide. In our configuration, optical power transfer is distributed along the length of the device via leaky mode coupling of light from the polyimide waveguide to the active region of the phototransistor. The TW electrode design allows for an electrically long structure while maintaining high bandwidths. Due to the increased absorption volume, the optical power handling capabilities of the TW-heterojunction phototransistors (TW-HPT's) are improved over that of conventional lumped-element HPT detectors. The experimental results show no saturation of the fundamental at 60 GHz up to 50 mA of dc photocurrent.

I. INTRODUCTION

ONE of the major commercial incentives driving research in photonics is the microwave fiber optic link. A typical link consists of a laser source, an external modulator, the fiber optic transmission medium, and an optical detector. High-frequency optical detectors are one of the primary components that dictate the system performance of the fiber optic link. In order to reduce the radio frequency (RF) insertion loss, increase the spurious free dynamic range, and increase the signal-to-noise ratio of the link, the photodetector needs to be able to handle high optical powers [1]. Heterojunction phototransistors (HPT's) which exhibit optical gain via transistor action offer improvements in link gain over p-i-n or MSM photodiodes. Although much work has been done on high-speed phototransistors [2], a classic design conflict exists between the simultaneous optimization of high-frequency performance and optical coupling efficiency. In lumped-element HPT's, the devices need to be scaled down in size for high-speed operation. These small devices tend to saturate at low input optical power levels because of the small absorption volume.

In an attempt to overcome these problems, we propose to utilize the traveling-wave (TW) concepts that have been implemented so successfully in optical modulator technology and extend these concepts to HPT detectors. A schematic diagram of our TW heterojunction phototransistor (TW-HPT) is shown in Fig. 1. In our approach, we define a leaky-mode polyimide waveguide on top of the active region of the HPT. Intensity-modulated light is coupled to the polyimide waveguide and leaks into the HPT's active region along the length of the device due to the fact that the index of refraction of the semiconductor is higher than that of the polyimide. The metal pads of the HPT are coplanar waveguide with the center line contacting the emitter and the ground plane contacting the collector. The base is floating. A microwave signal is generated on the transmission line as light is absorbed along the length of the detector. The ultimate bandwidth limitation of such a device is based on the velocity mismatch between the optical wave and the induced electrical microwave [3]–[6].

Due to the integration of the polyimide waveguide and the HPT in the TW configuration, power saturation effects are improved because the absorption of the incident light signal is distributed along the entire length of the device. The layer structure for the TW-HPT is a typical HBT design consisting of a 600-Å base with a graded base–emitter junction [7]. The polyimide optical waveguide is defined on top of the emitter and lies in the gap between the center electrode and the ground plane. Since the core size for single mode fiber at an optical wavelength of 1.3 μm is approximately 9 μm, we chose the dimensions of the polyimide waveguide to be 10 × 10 μm. A second set of devices was also fabricated in which the center electrode shorted the emitter to the base to form a diode structure. We will refer to this device as TW-Diode. The optical absorption interaction length between the waveguide and the HPT device was varied from 20, 200, to 2000 μm.

II. EXPERIMENTAL RESULTS

The dc optical responses of the TW-HPT and TW-Diode are shown in Fig. 2(a) and (b), respectively. A bias voltage of $V_{ce} = 1.5$ V was applied to all devices. Comparing the two figures, it is evident that the transistor action of the TW-HPT dramatically increases the sensitivity of the optical response. The optical gain G is as high as 13.5 for the 2-mm-long TW-HPT as opposed to $G = 0.374$ for the diode. For a given
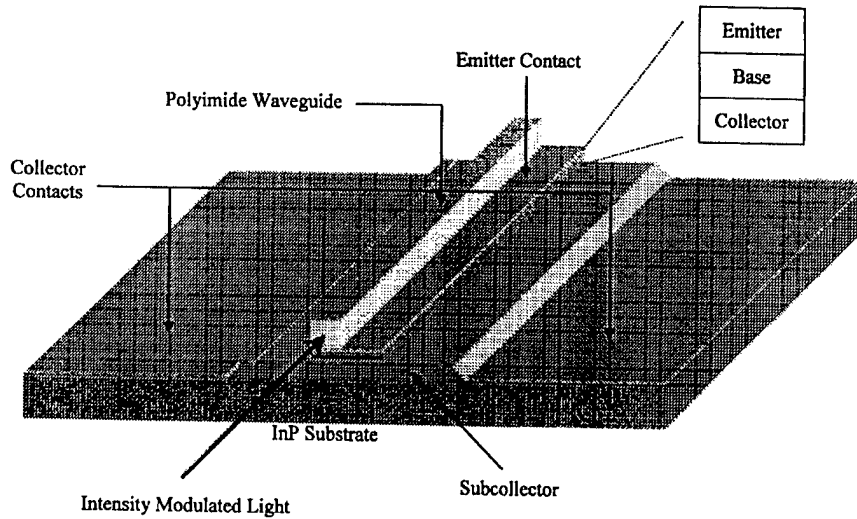
Fig. 1. Schematic diagram of the TW-HPT. Polyimide waveguide is defined on top of the active region of an HPT. The HPT's electrodes are coplanar waveguide with a characteristic impedance of 50 Ω.
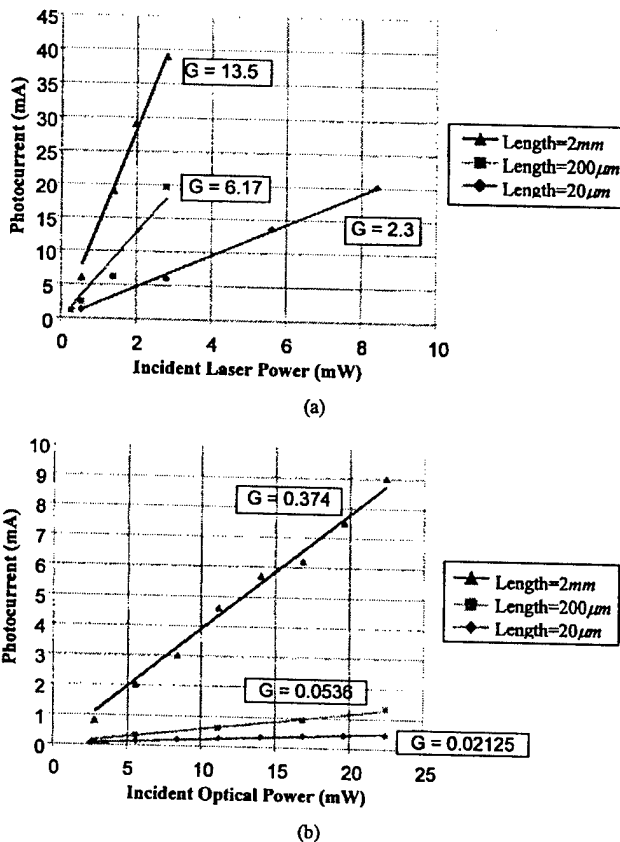

(a)

(b)

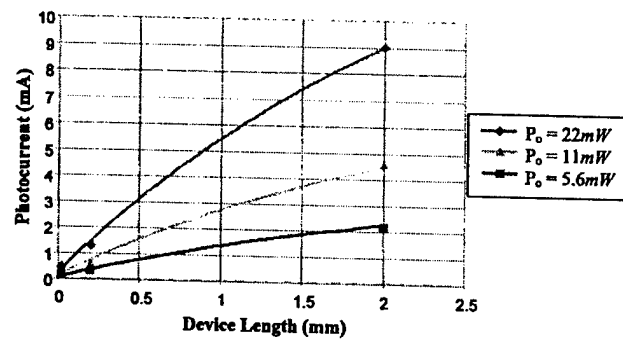Fig. 2. DC optical response of the (a) TW-HPT and (b) TW-Diode.

Fig. 3. Photocurrent as a function of TW-Diode device length for three different incident optical powers. The solid lines are the theoretical fit to the data.

optical power of 2.8 mW, the 2-mm-long diode photocurrent is 0.8 mA, but the corresponding transistor photocurrent is 40 mA, which is 50 times larger. In all cases the induced photocurrent increases linearly with increasing optical power indicating that the devices are not saturating.

By measuring the photocurrent as a function of device length for a given optical power, we can estimate the input

optical coupling efficiency. This is most easily accomplished with the diode since the transistor gain can vary from device to device. The results for the TW-Diode are shown in Fig. 3 for three different input optical powers. The solid lines are a theoretical fit to the measured data based on the equation

$$I_{ph} = \frac{q\eta}{h\nu} P_o. \tag{1}$$

I_{ph} is the optically generated portion of the output current, P_o is the incident optical power, q is the electronic charge, $h\nu$ is the energy of the incident photons, and η is the external quantum efficiency. The external quantum efficiency can be broken up into separate factors that describe the different mechanisms for light loss and light absorption:

$$\eta = \eta_{coupling} \cdot \eta_{propagation} \cdot \eta_{leaky} \tag{2}$$

where $\eta_{coupling}$ is the input coupling loss between the optical fiber and the polyimide waveguide, $\eta_{propagation}$ is the propagation loss from the optical input of the device to the active region, and η_{leaky} is the amount of light absorption that occurs in the active region via the leaky mode coupling mechanism. $\eta_{propagation}$ is difficult to estimate so we will
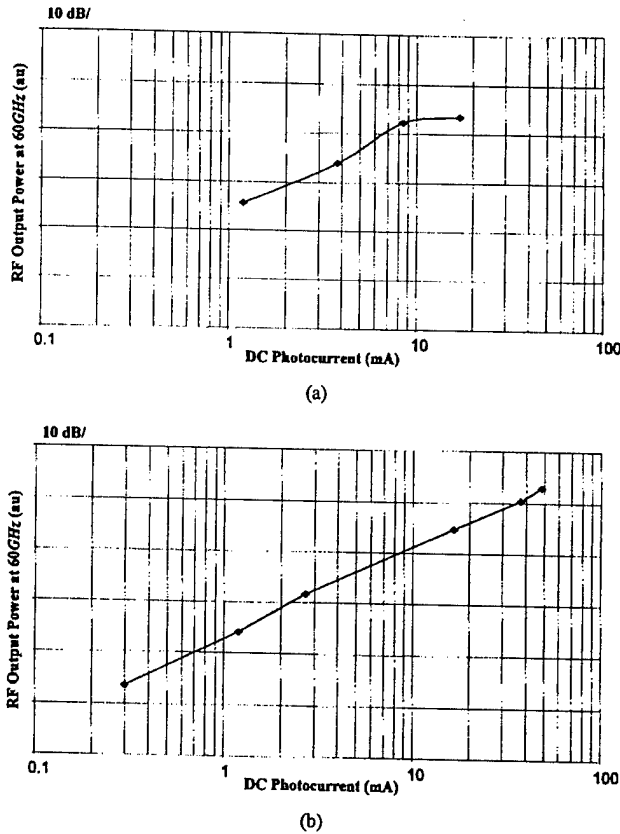
Fig. 4. Optical power saturation at 60 GHz for (a) lumped-element HPT and (b) 200-μm-long TW-HPT.

The optical power saturation measurements for the TW-HPT's were made at 60 GHz using two diode-pumped Nd:YAG lasers in an optical mixing configuration at a wavelength of 1.3 μm. The results are presented for the 200-μm-long device since this seemed to exhibit the best trade-off between device length and performance. The results for the TW-HPT were compared to a lumped-element HPT that was fabricated with a similar layer structure and had an emitter area of 8 × 8 μm. The displayed data in Fig. 4 shows that the lumped-element HPT output signal begins to saturate at a dc photocurrent of 8 mA whereas the 200-μm-long TW-HPT shows no signs of saturation up to 50 mA. The power-handling ability of the TW-HPT is superior to that of the lumped-element HPT due to the distributed nature of the optical absorption via the leaky mode configuration.

III. CONCLUSION

We experimentally measured the optical response of the TW-HPT and demonstrated high optical gains with input optical coupling efficiencies of 70%. A 200-μm-long TW-HPT exhibited no output power saturation up to 50 mA of dc photocurrent at an operating frequency of 60 GHz. We envision widespread applications of the high-power high-frequency TW-HPT in future photonic and optoelectronic integrated circuits.

combine $\eta_{\text{propagation}}$ with η_{coupling} and define this as the total input coupling loss prior to the active region of the device. η_{leaky} can be written mathematically as

$$\eta_{\text{leaky}} = 1 - e^{-\alpha_{op}l} \tag{3}$$

where α_{op} is the effective absorption coefficient which is determined by the thickness of the polyimide waveguide and l is the length of the active region. Plugging in (2) and (3) into (1) we obtain

$$(I_{ph} = \frac{qP_o}{h\nu} \eta_{\text{coupling}}(1 - e^{-\alpha_{op}l}). \tag{4}$$

Given that our polyimide waveguide thickness was measured to be 7.5 μm, the effective optical absorption coefficient given by our previously published simulations is taken to be $\alpha_{op} = 4$ cm^{-1} [7]. We can now fit (4) to the measured data of the 20-μm-, 200-μm-, and 2-mm-long TW-Diodes as shown in Fig. 3 and determine our input coupling efficiency to be $\eta_{\text{coupling}} = 70\%$.

REFERENCES

[1] L. Lembo, F. Alvarez, D. Lo, C. Tu, P. Wisseman, C. Zmudzinski, and J. Brock, "Optical electroabsorption modulators for wideband, linear, low-insertion loss photonic links," in *Proc. SPIE*, vol. 2481, 1996, pp. 185–196.

[2] S. Chandrasekhar, M. K. Hoppe, A. G. Dentai, C. H. Joyner, and G. J. Qua, "Demonstration of enhanced performance of an InP/InGaAs heterojunction phototransistor with a base terminal," *IEEE Electron Device Lett.*, vol. 12, Oct. 1991.

[3] L. Y. Lin, M. C. Wu, T. Itoh, T. A. Vang, R. E. Muller, D. L. Sivco, and A. Y. Cho, "High-power high-speed photodetectors—Design, analysis, and experimental demonstration," *IEEE Trans. Microwave Theory Tech.*, vol. 45, pp. 1320–1331, Aug. 1997.

[4] H. F. Taylor, O. Eknoyan, C. S. Park, K. N. Choi, and K. Chang, "Traveling wave photodetectors," in *Proc. SPIE, Optoelectronic Signal Processing for Phased-Array Antennas II*, 1990, vol. 1217, pp. 59–63.

[5] V. M. Hietala, A. Vawter, T. M. Brennan, and B. E. Hammons, "Traveling-wave photodetectors for high-power, large-bandwidth applications," *IEEE Trans. Microwave Theory Tech.*, vol. 43, pp. 2291–2297, Sept. 1995.

[6] K. S. Giboney, R. L. Nagarajan, T. E. Reynolds, S. T. Allen, R. P. Mirin, M. J. W. Rodwell, and J. E. Bowers, "Travelling-wave photodetectors with 172-GHz bandwidth and 76-GHz bandwidth-efficiency product," *IEEE Photon. Technol. Lett.*, vol. 7, pp. 412–414, Apr. 1995.

[7] D. P. Prakash, D. C. Scott, and H. R. Fetterman, "Integration of polyimide waveguides with traveling wave phototransistors," *IEEE Photon. Technol. Lett.*, vol. 9, pp. 800–802, June 1997.

The Optical Response of Epitaxial Lift-Off HEMT's to 140 GHz

Daipayan Bhattacharya, Hernan Erlig, Mohammed E. Ali, Shamino Wang, Harold R. Fetterman, *Fellow, IEEE,* Richard Lai, and Dwight C. Streit, *Senior Member, IEEE*

Abstract—We present measurements on the optical frequency response of epitaxial lift-off (ELO) 1.0-μm InP high-electron mobility transistors (HEMT's) to 140 GHz using electrooptic sampling and heterodyne techniques. Our picosecond sampling measurements established that the lift-off devices exhibited substantial optical response to 140 GHz. Heterodyne measurements made at 60 and 94 GHz later confirmed these findings. A novel three wave mixing technique was used to extend the heterodyne bandwidth to 130 GHz. In these experiments, millimeter waves were generated in our optically driven HEMT's and launched into waveguides. These lift-off devices can be major additions to future millimeter wave integrated optoelectronic systems either as high frequency optical detectors or as optically driven tunable millimeter wave sources.

Index Terms— Electrooptic measurements, epitaxial lift-off, integrated optoelectronics, millimeter wave generation, MODFET's, optical mixing, picosecond sampling.

I. INTRODUCTION

OF ALL THE techniques that have been studied to integrate electrical and optical circuits, including flip-chip bonding, wafer bonding, and heteroepitaxy, epitaxial lift-off (ELO) has shown itself to be particularly versatile. Devices from different material systems can be combined by releasing the epitaxially grown layers from their original substrate and grafting them to virtually any other suitable substrate. In the past, researchers have shown the effectiveness of this technique with numerous material systems, including semiconductor to semiconductor [1], semiconductor to glass [2], semiconductor to sapphire, and semiconductor to diamond [3], among others.

One class of devices which are important elements in all optoelectronic systems, namely semiconductor photodetectors, stand to benefit greatly from ELO technology. Prior research has shown that little degradation occurs in the optical [4] or electrical response [5] of devices after lift-off at microwave frequencies. Recently, largely because of WDM communication applications, there has been a push to develop optical systems that can work at millimeter wave frequencies. The ef-

fect of the grafting process on the millimeter wave response of high-frequency photodetectors, investigated here, is therefore a critical area of research for future integrated devices.

A continuous challenge to researchers in the field of ultrafast optoelectronic devices has been the ability to accurately measure their response. Two techniques that have been widely used are optical heterodyne and picosecond electrooptic sampling. Picosecond electrooptic sampling offers excellent linearity, the ability to characterize a calibrated high-frequency response, and minimal intrusion on the circuit which is being measured. Optical heterodyne, on the other hand, has the advantages of being highly sensitive and has the capability of examining important device applications.

In this paper, we measure the optical response of 1-μm InP ELO PHEMT's on quartz substrates to 140 GHz using both picosecond electrooptic sampling and optical heterodyne characterizations. In our picosecond measurements, a novel technique is used, whereby we sample directly from commercial coplanar probes. This makes it unnecessary to wire bond or connect coplanar lines to the device for minimally invasive probing. Our sampling results establish that the lift-off process does not adversely affect the high-frequency optical response of the high-electron mobility transistor (HEMT) photodetectors to 140 GHz. Optical heterodyne experiments at 60, 94, and 130 GHz provide further confirmation of this. The extension of our heterodyne experiments to 130 GHz utilizes a three-wave mixing technique. To our knowledge, this is the highest frequency optical mixing to date and confirms the use of lift-off HEMT's as high-frequency optical detectors. These devices can be readily integrated into millimeter wave optoelectronic systems by using ELO configurations.

II. DEVICE PARAMETERS AND FABRICATION

A cross section of the layer structure of our 1-μm gate HEMT's is shown in Fig. 1. The layers of the device were grown on an InP substrate using molecular beam epitaxy (MBE). The 20-nm InGaAs capping layer was heavily doped to allow for good low-resistance ohmic contacts to the source and drain and to protect the donor layer from surface oxidation. The 20-nm InAlAs donor layer was planar doped with Si at a level of 3.66×10^{12} cm^{-3}. A small 2-nm undoped InAlAs layer was included to further separate the 2DEG channel electrons from coulombic interactions with the ionized dopant atoms in the donor layer. A 15-nm undoped In$_{0.7}$Ga$_{0.3}$As pseudomorphic layer was used as the 2DEG channel. Hall mobility measurements on the samples yielded channel mobilities of
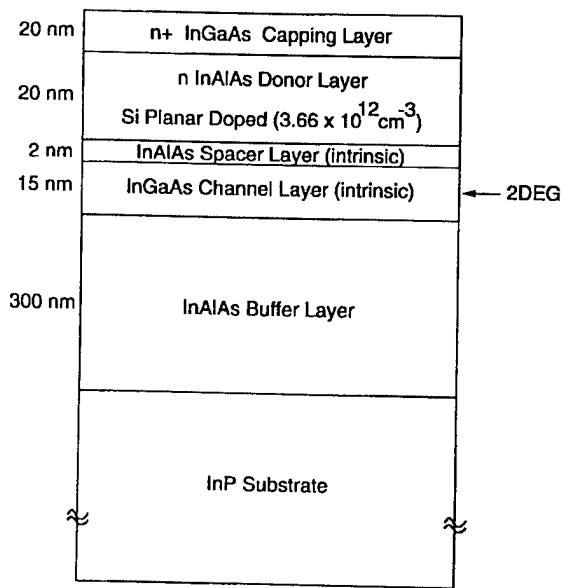
Fig. 1. Cross section of pseudomorphic expitaxial lift-off high-electron mobility transistor, detailing layer structure.

10 860 cm^2/V·s at 300 K. Finally, a 300-nm InAlAs buffer layer was included to serve as an etch stop in the epitaxial lift-off process.

The process of preparing the ELO films involved two distinct steps. The removal of the processed device film from its original substrate and the subsequent attachment of the thin film onto a host substrate. For devices fabricated on the InP material system, the etch selectivity of hydrochloric acid (HCl) for InP versus InAlAs was exploited. In this method, the entire backside of the substrate can be etched away. The InAlAs buffer layer acts as an etch stop, preventing damage to the active device layers. Our device wafers were mechanically thinned and polished to 50 μm prior to etching. This allowed for better control of the use of the etch stop by using dilute concentrations of HCl while still maintaining reasonable etch times. The sample was then covered with Apiezon W wax (black wax) which was dissolved in tricholoroethylene (TCE). By dissolving the wax in TCE, the proper consistency was achieved to allow the wax to flow to the edges of the sample. The main functions of the black wax were to protect the top layers of the device from the etchant and to give the thin film mechanical stability during the time it was removed from the substrate till it was attached to the host substrate. Immersion of the sample in HCl for about 6 min sufficed to etch away the 50-μm substrate.

For our measurements, we chose quartz as a host substrate since it is transparent and has low microwave loss. For the optical heterodyne experiments, the thin film devices were attached to the quartz using Van der Waals' forces. In this process, the device, supported by the black wax, is allowed to dry under weight for about 24 h. Attractive forces between the substrate and the semiconductor squeeze out the water until short-range Van der Waals' forces hold the two together [6]. Van der Waals bonding is a very versatile technique in that any semiconductor material can be attached to almost any
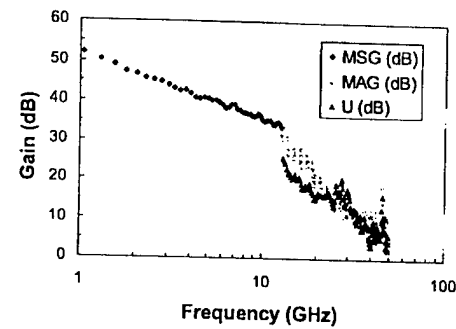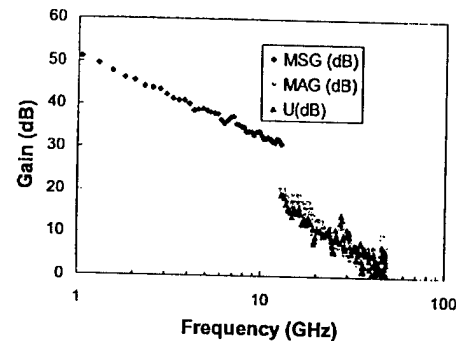
Fig. 2. Electrical gain response [maximum available gain (MAG), maximum stable gain (MSG) and unilateral power gain (U)] of (a) bulk HEMT photodetectors and (b) lift-off HEMT photodetectors were measured on a HP8510C vector network analyzer. By extrapolation of the U data, the f_{max} of the bulk and lift-off devices are found to be 60 and 50 GHz, respectively.

host, given conditions of planarity and cleanliness. However, for our devices, yields of only about 10% were achieved using this Van der Waals bonding approach. Therefore, an alternative attachment method was used for devices used in the electrooptic sampling experiments and the electrical RF measurements. Here an ultraviolet curable optical adhesive was used to attach the film to the substrate. Using this approach, the yield of the grafted film devices improved dramatically. DC electrical measurements showed no difference for the films attached using Van der Waals bonding and optical adhesive bonding.

III. ELECTRICAL CHARACTERIZATION

The electrical response of our devices were characterized by measurements of the peak transconductance and S-parameters on an extended HP8510C vector network analyzer (45 MHz–50 GHz) for both bulk and lift-off devices. The devices were contacted using on-wafer air coplanar probes (Picoprobe Model 67A by GGB Industries Incorporated). For the bulk devices, the maximum extrinsic transconductance g_m was measured to be 29.0 mS at a gate voltage of −0.1 V. For the lift-off devices, the peak g_m was 21.0 mS at a gate voltage of −0.48 V. The S-parameter measurements yielded the gain profiles of the devices, as shown in Fig. 2(a) for the bulk devices and Fig. 2(b) for the lift-off devices. The bulk devices and the lift-off devices had f_{max}'s of 50 and 60 GHz, respectively. Both the bulk and the lift-off devices had f_Ts
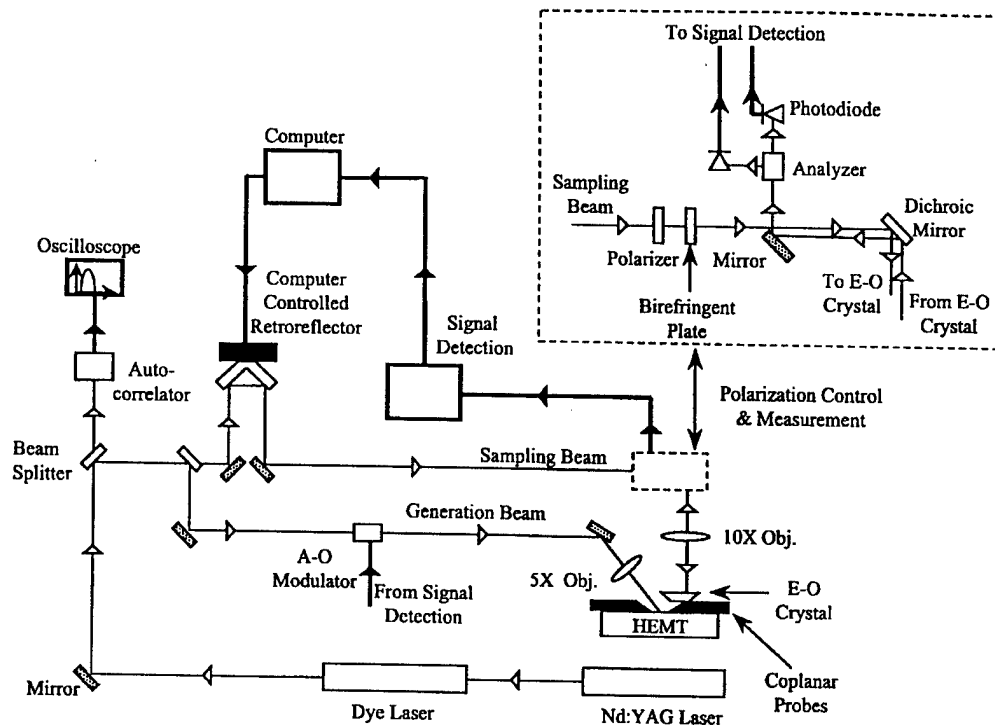
Fig. 3. Electrooptic sampling system schematic. Details of the electrooptic intensity modulator are shown.

of 40 GHz. The electrical response of the lift-off devices are only slightly degraded when compared to the bulk devices.

IV. ELECTROOPTIC SAMPLING TECHNIQUE

A. Experimental Setup and Calibration

To measure the photoresponse of the lift-off HEMT's, an external electrooptic sampling scheme was used, similar to that presented in [7]. A simplified schematic of the pump-probe setup is shown in Fig. 3. The laser system was comprised of a synchronously mode-locked dye laser pumped by the frequency-doubled output of an actively mode-locked Nd:YAG laser. The dye gain medium was Rhodamine 6G and further pulse narrowing was achieved by using a DODCI saturable absorber. The 608-nm output of the dye laser consisted of a pulse train of 1.4-ps full width at half maximum (FWHM) pulses, measured with an autocorrelator, with a repetition rate of 76 MHz and an average power of 115–125 mW. The sampling beam was routed through a corner cube reflector mounted on a computer-controlled translation stage. In this fashion, the timing between the sampling and generation pulses could be controlled. At the input of the electrooptic intensity modulator, the sampling beam average power was maintained at approximately 3.2 mW. After transmission through the acoustooptic modulator, the average generation beam power was 3.4 mW. The intensity of the sampling and generation beams were controlled by attenuators not shown in Fig. 3. At the end of the generation arm, the beam was focused onto the active area of the HEMT using a 5× objective lens.

The use of the electrooptic intensity modulator in this sampling application is found in [7] and [8]. A commercial 20-μm-thick LiTaO$_3$ crystal (Terametrics Model 200C-TIR) was used to perform the electrooptic modulation. This crystal thickness has been shown to minimize the distortion of the measured signal when compared to thicker crystals [9]. The crystal is in the shape of an inverted truncated pyramid, the faces of which are cut at 60 deg. The angled faces of the crystal make it possible to use total internal reflection to collect the sampling beam for analysis. Both the bulk and lift-off HEMT's were contacted via air coplanar probes (Picoprobe Model 67A). The probes have a 100-μm pitch and exhibit nearly a 50-Ω impedance from dc to 67 GHz. The photoresponse of the HEMT was sampled by bringing the LiTaO$_3$ crystal into close proximity of the coplanar probe on the drain side. A schematic representation of this is shown in Fig. 4. The optic axis of the crystal was oriented perpendicular to the center line of the coplanar probe and parallel to the base of the crystal.

Typical half wave voltages, V_π, for the intensity modulators used in electrooptic sampling are on the order of kilovolts [10]. Therefore, in order to detect millivolt-level signals, careful attention has to be paid to minimizing noise, which in this case, is largely laser RIN noise. To this end, the mixing approach developed by Chwalek in [11] was used. In this scheme, the relatively small electrooptic intensity modulation is detected differentially. However, if an imbalance exists in the detection system, the amplitude noise of the laser can severely degrade the signal-to-noise ratio (SNR). By modulating the generation beam at high frequencies where the laser amplitude noise is low, the effect of the system imbalance can be minimized (see the Appendix for mathematical derivations). A two-channel RF
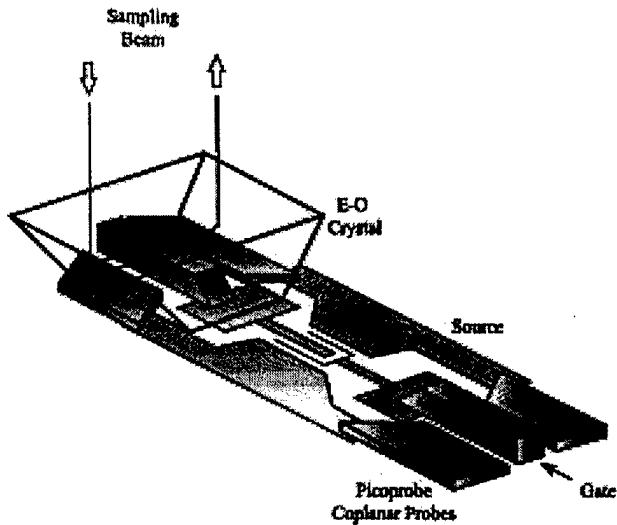
Fig. 4. Schematic of sampling from coplanar probes. The LiTaO$_3$ crystal is situated over the drain of the device and total internal reflection is used to retrieve the sampling beam.

mixer system (Terametrics Model 100-RF) which employed a square wave at 3.000 MHz and a sine wave at 2.998 MHz was used.

To obtain a first-order estimate of the electrooptic signal strength and the SNR, a 6-mm-long coplanar waveguide was contacted at the ends by the coplanar probes and the LiTaO$_3$ crystal was situated over one of the probes. The 55-Ω coplanar waveguide had a center transmission line width of 50-μm and a center transmission line to ground plane separation of 50-μm. A sinusoidal waveform at 3.000 MHz was applied to one of the coplanar probes and monitored on an oscilloscope. For a sampling beam average power of 3.2 mW and a voltage sinusoid amplitude of 481 mV, the rms voltage detected by the lock-in amplifier (LIA) was 12.75 μV. The equivalent noise voltage was measured to be 223.6 nV/$\sqrt{\text{Hz}}$. For sampling purposes, the lock-in filter bandwidth was chosen to be 1 s and every point was measured 25 times for averaging. These factors considered, the minimum detectable voltage was 1.88 mV.

Because of spatial considerations, the sampling function took place near the end of the crystal. Therefore the electrical transient had to propagate approximately 100 μm through the crystal before reaching the sampling site. Propagation through the crystal causes degradation of the transient being sampled. Furthermore, the high-frequency behavior (beyond 67 GHz) of the coplanar probes was not known. In order to have an estimate of the influence of these effects on the frequency response of the sampling system, a simple comparative test was performed. This involved the fabrication of low-temperature GaAs (LT-GaAs) photoconductive switches imbedded into coplanar waveguide. The coplanar waveguide geometry was identical to that described above. The photoconductive switch gap was 50 μm long and 20 μm wide. The switch was biased at 40 V. The response from the switches was measured under two different sampling conditions. First, the LiTaO$_3$ crystal was contacted to the coplanar waveguide approximately
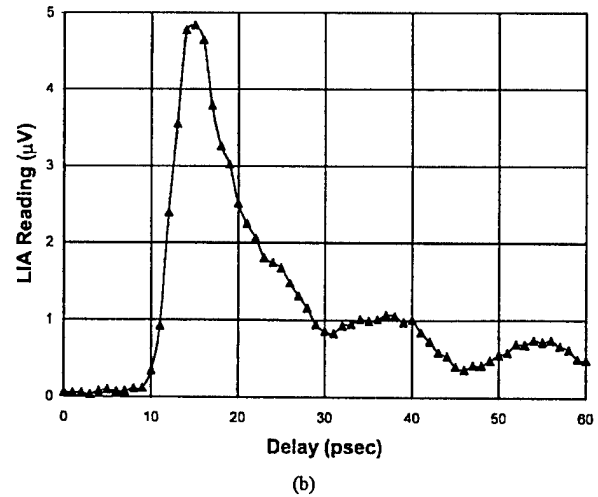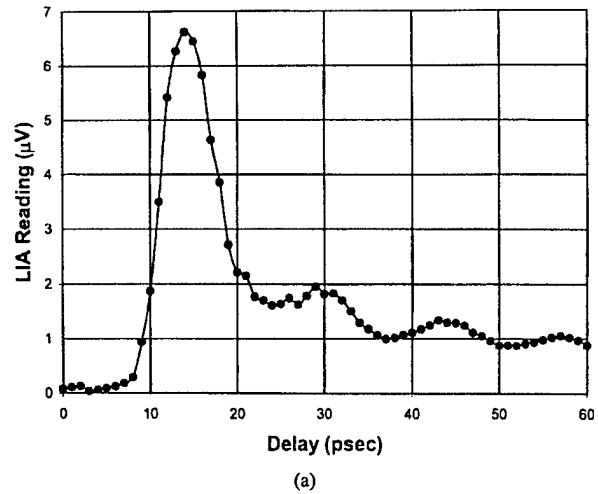

(a)

(b)

Fig. 5. Time-domain photoresponse of (a) lift-off HEMT and (b) bulk HEMT. Both responses exhibit a short initial pulse followed by a slowly decaying tail. The pulses have a FWHM of 7.8 and 8.3 ps for the lift-off and bulk HEMT's, respectively. The ripples in the tail are attributed to electromagnetic radiation emitted by the device.

1 mm from the generation site. The sampling site within the crystal was near the entrance face, where the electrical transient entered. The photoresponse in the frequency domain for this sampling condition was $Y_1(\omega)$. Whenever referring to functions or calculations in the frequency domain, it is to be understood that only the amplitude spectra is being used. Second, a coplanar probe was used to contact the coplanar waveguide at approximately 1 mm from the generation site. The LiTaO$_3$ crystal was situated over the coplanar probe and the sampling site was moved to the end of the crystal. The measured photoresponse in the frequency domain was $Y_2(\omega)$. The electrical transient just before 1 mm from the generation site is assumed to be similar for both sampling conditions. Therefore, any difference in the measured switch response must be due to the two different sampling geometries.

The frequency response comparison estimate can be quantified from the theory of linear systems

$$\frac{Y_2(\omega)}{Y_1(\omega)} = \frac{H_2(\omega)X(\omega)}{H_1(\omega)X(\omega)} = \zeta(\omega) \qquad (1)$$
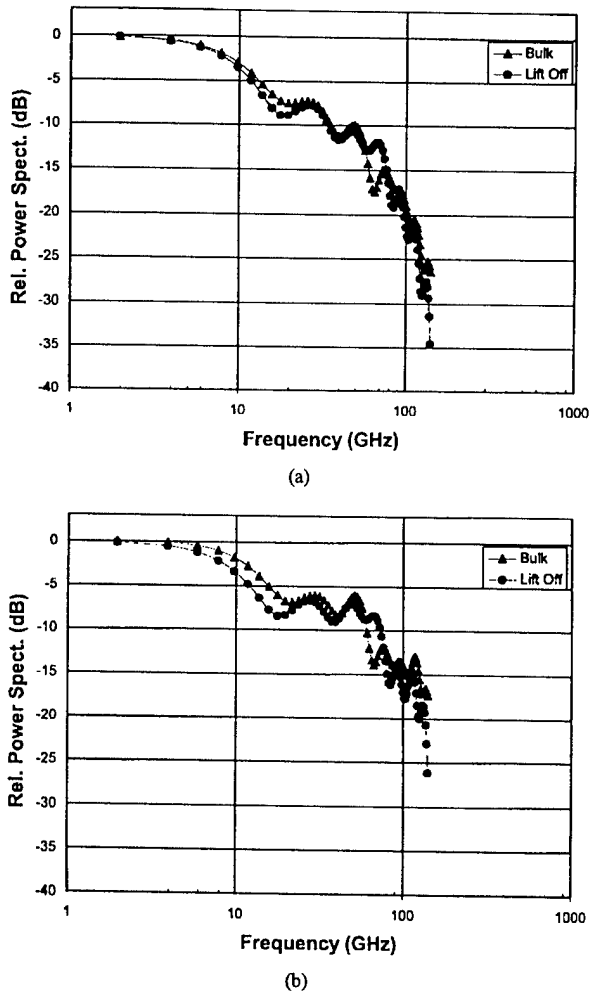
(a)

(b)

Fig. 6. (a) Lift-off and bulk HEMT relative power spectrum to 140 GHz obtained from time-domain data and (b) calibrated lift-off and bulk HEMT relative power spectrum to 140 GHz using (3) and the calibrating function, $\zeta(\omega)$. Beyond 30 GHz, the calibrated response shows an improvement over the uncalibrated data. At 140 GHz, the improvement is approximately 10 dB. The ripple in the response is attributed to the tails present in the time-domain response.

where $H_1(\omega)$ is the sampling system frequency response for sampling condition one, $H_2(\omega)$ is the system frequency response for sampling condition two, and $X(\omega)$ is the Fourier transform of the electrical transient just before 1 mm from the generation site. The function $\zeta(\omega)$, the system frequency response ratio, was calculated to 140 GHz. Beyond 80 GHz, $\zeta(\omega)$ shows a sharp roll off and at 140 GHz its value is 0.375 of that at dc.

B. HEMT Optical Frequency Response Measurements

For the optical response measurements, the drain to source bias on the lift-off and bulk devices was 2.0 V. Typically, a moderate negative bias must be applied on the gate in order to obtain a fast photoresponse from HEMT's. As the negative bias on the gate increases, such that the transconductance approaches zero, the photoresponse speed increases [12]. Our dc measurements show the transconductance for both the lift-off and bulk devices approaches 0 S at approximately −1.0

V gate to source. Therefore, for the measurements presented here the gate to source bias for both lift-off and bulk HEMT's was set to −4.0 V.

For the specified bias conditions, the photoresponse in the time domain is shown in Fig. 5(a) and 5(b) for the lift-off and bulk HEMT's, respectively. Qualitatively the photoresponse from the lift-off and bulk device are similar. Both exhibit an initial short pulse followed by a slowly decaying tail, these results are in agreement with those found in [13]. The tail is attributed to the collection of slow moving photogenerated holes. The magnitude of the tail and therefore its influence on the photoresponse is a strong function of the gate bias. This trend was experimentally observed in a set of preliminary measurements, where the tail amplitude decreased as the negative bias on the gate increased. For the lift-off HEMT's the photoresponse pulse exhibits a FWHM of 7.8 ps; while for the bulk devices the pulse exhibits a 8.3-ps FWHM.

Due to the probing geometry, part of the LiTaO$_3$ crystal protrudes beyond the coplanar probes and was situated above the device. The reflected light from the device active area partially struck the over hanging crystal. This, combined with the fact that the gate (Schottky diode) was illuminated, led us to believe that the disturbance of the photoresponse was caused by electromagnetic radiation emitted by the HEMT [14], [15]. To validate our hypothesis, the coplanar probe was removed from the drain and the vicinity of the device, while the crystal was maintained at its sampling position. A signal was detected with the drain floating and the gate biased relative to the source. Our measurements showed an increase in signal strength with increasing negative bias on the gate, in agreement with the findings of [14]. It was also discovered that by moving the location of the generation beam the signal strength was altered. This can be understood by realizing that the reflected beam struck the crystal at different positions as the generation beam was moved. These preliminary results support our electromagnetic radiation hypothesis. The ripple in the time-domain photoresponse tail is attributed to this phenomenon.

From the time-domain measurements, the relative power spectrum for both the lift-off and bulk devices was calculated. Given that the Fourier transform of the HEMT photoresponse is $Y_{\text{HEMT}}(\omega)$, the relative power spectrum is given by

$$P_{R,\text{HEMT}}(\omega) = 20 \log \left[\frac{Y_{\text{HEMT}}(\omega)}{Y_{\text{HEMT}}(0)} \right] \qquad (2)$$

and is measured in decibels. $P_{R,\text{HEMT}}(\omega)$ is graphed in Fig. 6(a) up to 140 GHz for both sets of devices. The ripple in the relative power spectrum can be accounted for by the tail present in the time-domain photoresponse.

It is possible to roughly de-embed the effects of sampling condition 2 by using the calculated function $\zeta(\omega)$. The measured photoresponse is $Y_{\text{HEMT}}(\omega) = H_2(\omega)Q(\omega)$, where $Q(\omega)$ is the HEMT photoresponse at the contact pads. The adjusted response is

$$Y'_{\text{HEMT}}(\omega) = \frac{Y_{\text{HEMT}}(\omega)}{\zeta(\omega)} = H_1(\omega)Q(\omega). \qquad (3)$$

In Fig. 6(b), the adjusted relative power spectrum is displayed.

The devices exhibit moderate frequency response up to 140 GHz. These results provided the motivation to optically heterodyne to 130 GHz. From Fig. 6(a) and (b), it is apparent that there is no significant degradation in the device photoresponse for the lift-off devices compared to the bulk devices. This is an encouraging result that provides validation for the integration of photonic and nonphotonic materials by the epitaxial lift-off process.

V. OPTICAL HETERODYNE TECHNIQUE

A. Theory of Optical Heterodyne

Optical heterodyne detection has been investigated by others to characterize the high-speed performance of photodetectors and optical receivers [16], [17]. This technique has the special advantages of being very broad-band and sensitive. The process involves the superposition and mixing of two laser beams in the device under test. Most simply, the interfering beams can be represented by two plane electromagnetic waves of frequency ω_1 and ω_2. Assuming that they are collinear and have the same polarization, the resultant electric field of the two beams can be written as

$$E_t = E_1 \cos \omega_1 t + E_2 \cos \omega_2 t \tag{4}$$

where E_1 and E_2 are the electric field amplitudes of the incident beams. The device responds to the intensity of the incident light which is proportional to the square of the total electric field given by

$$E_t^2 = \frac{E_1^2}{2} + \frac{E_2^2}{2} + E_1 E_2 \cos(\omega_1 - \omega_2)t. \tag{5}$$

In deriving (5), the high-frequency term (sum) has been neglected. The total field generates photocurrents in our device which have both dc and ac components

$$
\begin{aligned}
i_{\text{total}} &= i_{\text{dc}} + i_{\text{ac}} \\
&= R_{\text{dc}} \left[\frac{E_1^2}{2} + \frac{E_2^2}{2} + F(\omega_b) \cdot E_1 E_2 \cos \omega_b t \right]
\end{aligned}
\tag{6}
$$

where R_{dc} is the dc responsivity of the device and $\omega_b = \omega_1 - \omega_2$ is the frequency of the beat signal. $F(\omega_b)$ is the frequency response of the device at ω_b and can be measured from dc to several hundreds of gigahertz by sweeping ω_b over the corresponding bandwidth. Such a sweep can be realized by using a frequency-tunable laser as a source for either of the two interfering optical signals. The quantum efficiency, η, is related to the change in dc photocurrent, i_{dc}, and the incident power, P_{inc}, by

$$\eta = \frac{h\nu}{q} \cdot \frac{i_{\text{dc}}}{P_{\text{inc}}} = \frac{h\nu}{q} \cdot R_{\text{dc}} \tag{7}$$

where h is Planck's constant, ν is the frequency of the incident radiation, and q is the electron charge.
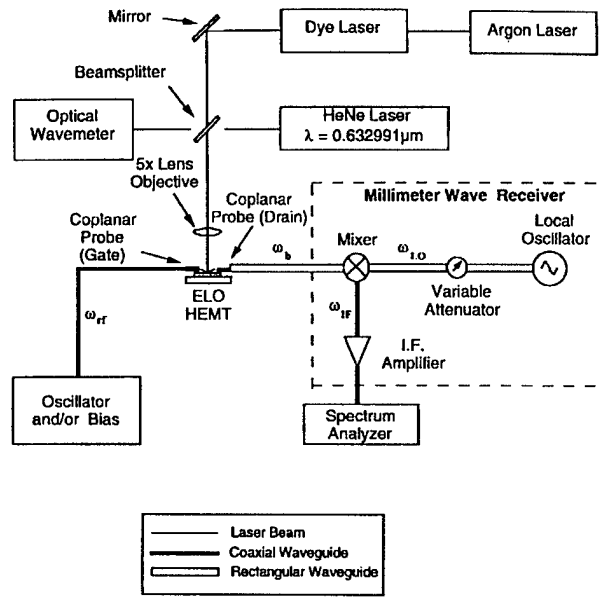

Fig. 7. Experimental setup of optical heterodyne measurements.

B. Optical Heterodyne Measurements

The experimental setup of our optical heterodyne measurements is shown in Fig. 7. A temperature-stabilized single-mode He–Ne laser (0.5 mW) with a linewidth of less than 1 MHz was employed as the source for the fixed frequency optical signal. A CW ring dye laser (Coherent CR 699-21, 300 mW) optically pumped by an argon laser was used as a tunable source for the local oscillator signal. A variable attenuator was used to reduce the dye power incident on the device. The dye laser was actively stabilized and servo-locked to an oven-stabilized Fabry–Perot interferometer by an external feedback mechanism. This ensured highly stable, mode-hop-free single-mode laser operation with a linewidth less than 0.5 MHz and a long-term frequency drift of less than 50 MHz/h. The dye laser was continuously tunable over the whole dye spectrum and could be linearly scanned over tens of gigahertz in its locked mode of operation. Kiton Red (600–640 nm) was used as the dye gain medium, ensuring hundreds of gigahertz of tunability around the HeNe wavelength (632.991 nm). Because of the very narrow linewidths and stability of the lasers, extremely sensitive optical heterodyne measurements on high-speed devices could be performed.

The two laser beams were combined and made collinear by a beam splitter. The combined beam was focused on the device under test by a 5× objective lens. A fraction of the dye laser beam was fed to a wavemeter (Burleigh) for continuous monitoring of the dye wavelength. The wavemeter, which has a resolution of 0.001 nm, allowed us to set the dye wavelength to an accuracy of less than 1 GHz for a given frequency offset from the HeNe. This gave us a rough estimate of the difference frequency generated by our mixing.

High-frequency coplanar probes and bias tees were used to make contact and dc bias the HEMT devices. The probes also acted as broad-band well-matched antennas. The millimeter wave signals generated in our devices were radiated and

TABLE I
OPTICAL HETERODYNE SNR OF THE LIFT-OFF
AND BULK HEMT'S AT 60, 94, AND 130 GHz

Frequency (GHz)	SNR for Lift-off HEMT (dB)	SNR for Bulk HEMT (dB)
60	19.3	21.4
94	14.0	14.2
130	8.2	10.7

ATTEN 0 dB   MKR -62.20 dBm
RL -59.3 dBm   2 dB/   1.5152 GHz

CENTER 1.5295 GHz   SPAN 100.0 MHz
RBW 300 kHz   VBW 1.0 kHz   SWP 200 ms

(a)

ATTEN 0 dB   MKR -72.47 dBm
RL -64.1 dBm   2 dB/   1.49933 GHz

CENTER 1.49250 GHz   SPAN 50.00 MHz
RBW 300 KHz   VBW 3.0 KHz   SWP 100 ms

(b)

Fig. 8. Optical heterodyne signal of the lift-off HEMT after downconversion of the (a) 94-GHz and (b) 130-GHz signals as seen on a spectrum analyzer. This data is also tabulated in Table I.

launched into waveguides through the probes. This is equivalent to radiating the signal by an integrated antenna structure and receiving the signal with a collecting horn. This opens up the possibility of using these devices as compact optically driven millimeter wave sources. Our experiments used a heterodyne detection scheme to downconvert the optically generated millimeter wave signals. The signal from the device was combined with a local oscillator using a directional coupler and then fed to a commercial mixer. The IF signal from the mixer was amplified and then displayed on a spectrum analyzer.

The lift-off devices showed dc responsivities of 4.2 A/W and a quantum efficiency of 825% when illuminated with the HeNe. Our optical heterodyne measurements were done at 60, 94, and 130 GHz on the HEMT's before and after lift-off. The results of these measurements are outlined in Table I. The spectrum analyzer traces of the 94-GHz and 130-GHz downconverted beat signals are shown in Fig. 8(a) and (b), respectively. As can be seen, both lift-off and bulk HEMT's have comparable performance within experimental errors. The process of lift-off has not produced any observable degradation in the optical response characteristics. In Table I, the appropriate bias was used to maximize the SNR for each frequency point.

It should be noted that in this table the data between frequency points is not calibrated. This is due to the fact that differences existed between the probing setup and the millimeter wave detection scheme for each frequency point. In the 60-GHz experiment, two 67-GHz coplanar probes (Picoprobe Model 67A) with V-connector outputs were employed at the drain and gate terminals. The drain output was fed into the mixer via a coaxial to a waveguide transition. The local oscillator was a tunable 60-GHz GUNN oscillator. In the 94-GHz experiment, a different coplanar probe (Picoprobe Model 120) was employed at the drain side. This probe has a built-in coplanar to W-band waveguide transition which enabled us to couple the optically generated signal directly into the mixer. A 94-GHz tunable reflex klystron was used for the local oscillator.

The detection of radiation with frequencies extending beyond the bandwidth of the coplanar probes (120 GHz) could
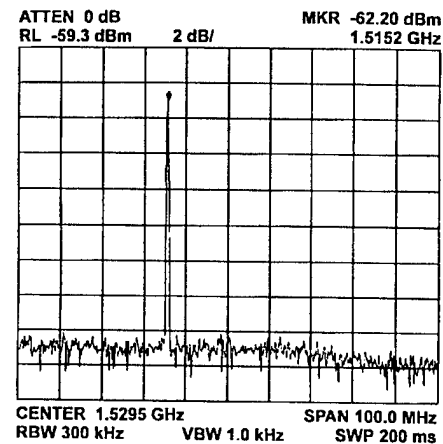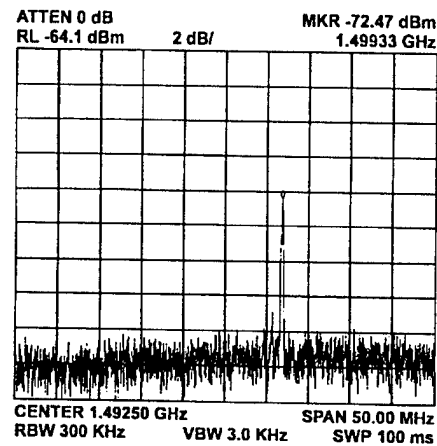
not be achieved with heterodyne detection as described above. This led us to devise a different detection scheme involving three-wave mixing for the 130-GHz measurements. In this scheme, a microwave or millimeter wave signal of frequency ω_{rf} was applied to the gate of the HEMT while it was illuminated with the two optical beams. The mixing of these three signals took place in the device. This process took advantage of the nonlinearity of the HEMT current–voltage characteristics to generate mixing products between the optically generated current at the difference frequency (ω_b) and the current component injected at the gate (ω_{rf}). One of the mixing products generated has a frequency $\omega_b - \omega_{rf}$ ($= \omega_1 - \omega_2 - \omega_{rf}$). By using an appropriate ω_{rf}, the frequency of the mixing product can be adjusted to a frequency (within the bandwidth of the probes) that could be radiated into the heterodyne receiver system.

The use of three-wave mixing to detect optical heterodyne signals in photoconductors was demonstrated in [17]. There the measurements involved frequencies less than a gigahertz, although the possibility of using this method beyond 100 GHz with a similar device made from a high-speed material was mentioned. The viability of this approach and the ability

of the HEMT to act as a high-speed three-wave mixer was demonstrated. Using this technique, high-frequency signals ranging up to 240 GHz can be detected with more readily available low-frequency sources.

In our experiments, a 130-GHz signal was optically generated in the HEMT and mixed with a 35-GHz signal applied to the gate. A klystron was used as a source for this gate signal. The 94-GHz output signal was launched into a waveguide and subsequently heterodyne detected in our millimeter wave detector. The local oscillator used for the final downconversion was a tunable 95-GHz GUNN oscillator. It is interesting to note that we also were able to observe the sum frequency of the mixing between the optically generated current and the injected gate current at 94 GHz ($\omega_b + \omega_{rf}$) by simply tuning the optical difference frequency from 130 to 60 GHz. This signal was approximately 5 dB larger than our 130-GHz signal.

Sensitive optical response measurements to 130 GHz on ELO HEMT's using heterodyne techniques has been demonstrated. Although measurements were conducted at only three discrete frequencies, it is possible to sweep the frequency in order to obtain a complete spectrum of the HEMT photoresponse. Our measurements confirm the ability to optically generate high-frequency signals in three terminal devices. This lends itself to the possibility of making compact millimeter wave sources using optically driven ELO HEMT's and semiconductor lasers.

VI. CONCLUSION

We have successfully measured the optical response of 1-μm ELO HEMT photodetectors to modulation frequencies of 140 GHz using both electrooptic sampling and optical heterodyne techniques. Our picosecond results demonstrate that lift-off devices can be used at millimeter wave frequencies with no degradation in response. Optical heterodyne experiments at 60, 94, and 130 GHz provided further confirmation of this. These results indicate the enormous potential of the epitaxial lift-off process in the integration of millimeter wave optoelectronic integrated systems. Current efforts in this area include testing at 1.3 μm for applications in communication systems, performing a fully calibrated optical heterodyne response to 150 GHz, and characterizing the effect of the illumination level on the millimeter wave response of high-frequency devices. These latest efforts will focus on 0.1-μm and 50-nm gate HEMT photodetectors which have f_T's of 170 and 340 GHz, respectively.

APPENDIX

For millivolt-level electrical transients under typical sampling conditions, the electrooptic signal is weak. A differential

detection method can be employed to enhance the SNR. Operationally, in matching the detection system there will be a small imbalance, ψ, caused by variations in photodiode load, responsivity, and illumination ($0 < \psi < 1$). Due to this imbalance, laser amplitude noise and Shot and/or Johnson noise will contribute to the degradation of the SNR. When the generation beam is amplitude modulated for signal detection purposes, modulated laser amplitude noise will also cause a degradation in SNR.

For the detection system used in this paper, the SNR is defined in (A1), shown at the bottom of the page, where V_o is the peak–peak voltage drop across the crystal, V_{avg} is the voltage drop across a photodiode load due to the sampling beam average power, $|V_n(f)|^2$ is the power spectral density arising from Shot and/or Johnson noise, $|N(f)|^2$ is the spectral density of the laser amplitude noise, f_m is the frequency at which the generation beam is modulated, and Δf is the bandwidth of the detection system (limited by the LIA). In deriving (A1), it was assumed that $|N(f)|^2$ does not vary significantly across the detection bandwidth [8]. In the denominator of (A1), the first two terms correspond to the laser amplitude noise power and the Shot and/or Johnson noise power, respectively, while the third term represents the modulated laser amplitude noise power.

Assuming small $|V_n(f)|^2$, $\psi \gg 2V_o/V_\pi$, and in the limit of low modulation frequencies such that $|N(f)|^2 \approx |N(f - f_m)|^2$, the SNR is dominated by the laser amplitude noise and can be simplified to

$$\text{SNR} \approx \frac{V_o^2}{\left(\dfrac{\psi V_\pi}{2}\right)^2 |N(f)|^2 \Delta f}. \tag{A2}$$

According to (A2), the SNR can be improved by increasing the modulation frequency provided there is an imbalance in the detection system. However, this trend cannot be maintained indefinitely. When the modulation frequency is such that $(|N(f_m)|/|N(0)|)^2 = (2V_o/\psi V_\pi)^2$, the modulated laser amplitude noise contributes the same amount of power as the laser amplitude noise. Beyond this point, the efficacy of increasing the modulation frequency begins to decrease.

The effect of the modulation frequency on the SNR can be judged from the ratio of the modulated laser amplitude noise power to the power of the other noise sources which we call ϑ. Experimentally this ratio can be determined by first measuring the noise power level with a voltage applied to the coplanar probe and subsequently with no voltage applied. We define this ratio as γ^2 and is related to ϑ by (A3), shown at the top of the next page. With a 481-mV signal applied to the coplanar probe and for our sampling conditons, $\gamma = 1.979$. In this case,

$$\text{SNR} \simeq \frac{2\left(\dfrac{V_{avg}}{V_\pi}\right)^2 V_o^2}{\left(\dfrac{(\psi V_{avg})^2}{2} |N(f)|^2 + 2|V_n(f)|^2 + 2\left(\dfrac{V_{avg}}{V_\pi}\right)^2 V_o^2 |N(f - f_m)|^2\right)\Delta f} \tag{A1}$$

$$\gamma^2 = \frac{\frac{(\psi V_{avg})^2}{2}|N(f)|^2 + 2|V_n(f)|^2 + 2\left(\frac{V_{avg}}{V_\pi}\right)^2 V_o^2|N(f - f_m)|^2}{\frac{(\psi V_{avg})^2}{2}|N(f)|^2 + 2|V_n(f)|^2} = \vartheta + 1 \tag{A3}$$

the modulated laser amplitude noise power is approximately three times larger than the laser amplitude and Shot and/or Johnson noise power combined.

REFERENCES

[1] D. M Shah, W. K. Chan, T. J. Gmitter, L. T. Florez, H. Schumacher, and B. P. Van der Gaag, "DC and RF performance of GaAs MESFET fabricated on silicon substrate using Epitaxial lift-off technique," *Electron. Lett.*, vol. 26, no. 22, pp. 1865–1866, Oct. 1990.
[2] F. Kobayashi and Y. Sekiguchi, "GaAs Schottky photodiode fabricated on glass substrate using epitaxial lift-off technique," *Jpn. J. Appl. Phys.*, vol. 31, no. 7A, pp. L850–L852, July 1992.
[3] V. Arbet-Engels, W. Chang, E. Yablonovich, G. J. Sullivan, M. K. Swed, and M. F. Chang, "Flexible, thin-film, GaAs hetero-junction bipolar transistors mounted on natural diamond substrates," *Solid State Electron,*, vol. 38, no. 11, pp. 1972–1974, 1995.
[4] D. Bhattacharya, P. S. Bal, H. R. Fetterman, and D. Streit, "Optical mixing in epitaxial lift-off pseudomorphic HEMT's," *IEEE Photon. Technol. Lett.*, vol. 7, pp. 1171–1173, 1995.
[5] P. G. Young, S. A. Alterovitz, R. A. Mena, and E. D. Smith, "RF properties of epitaxial lift-off HEMT devices," *IEEE Trans. Electron Devices*, vol. 40, pp. 1905–1909, Nov. 1993.
[6] E. Yablonovich, D. M. Hwang, T. J. Gmitter, L. T. Florez, and J. P. Harbison, "Van der Waals bonding of GaAs epitaxial films onto arbitrary substrates," *Appl. Phys. Lett.*, vol. 56, pp. 2419–2421, June 1990.
[7] J. A. Valdmanis, "1 THz-Bandwidth prober for high-speed devices and integrated circuits," *Electron. Lett.*, vol. 23, no. 24, pp. 1308–1310, 1987.
[8] B. H. Kolner, "Picosecond electro-optic sampling in Gallium Arsenide," Ph.D. dissertation, Stanford University, Stanford, CA, 1985.
[9] M. Y. Frankel, J. F. Whitaker, G. A. Mourou, and J. A. Valdmanis, "Experimental characterization of external electrooptic probes," *IEEE Microwave Guided Wave Lett.*, vol. 1, pp. 60–62, 1991.
[10] T. Nagatsuma, T. Shibata, E. Sano, and A. Iwata, "Subpicosecond sampling using a noncontact electro-optic probe," *J. Appl. Phys.*, vol. 66, no. 9, pp. 4001–4009, 1989.
[11] J. M. Chwalek and D. R. Dykaar, "A mixer based electro-optic sampling system for submillivolt signal detection," *Rev. Sci. Instrum.*, vol. 61, no. 4, pp. 1273–1276, 1990.
[12] M. Z. Martin, F. K. Oshita, M. Matloubian, H. R. Fetterman, L. Shaw, and K. L. Tan, "High-speed optical response of pseudomorphic InGaAs high electron mobility transistors," *IEEE Photon. Technol. Lett.*, vol. 4, pp. 1012–1014, 1992.
[13] F. K. Oshita, "Picosecond optoelectronic characterization of ballistic electron transistors," Ph.D. dissertation, Univ. California at Los Angeles, 1992.
[14] L. Xu, X. C. Zhang, D. H. Auston, and B. Jalali "Terahertz radiation from large aperture Si p-i-n diodes," *Appl. Phys. Lett.*, vol. 59, no. 26, pp. 3357–3359, 1991.
[15] X. C. Zhang, B. B. Hu, J. T. Darrow, and D. H. Auston, "Generation of femtosecond electromagnetic pulses from semiconductor surfaces," *Appl. Phys. Lett.*, vol. 56, no. 11, pp. 1011–1013, 1990.
[16] R. T. Hawkins, II, M. D. Jones, S. H. Pepper, and J. H. Goll, "Comparison of fast photodetector response measurements by optical heterodyne and pulse response techniques," *J. Lightwave Technol.*, vol. 9, pp. 1289–1294, 1991.
[17] J. K. A. Everard, "Novel coplanar three wave mixer for coherent and heterodyne detection of optical signals," *Electron. Lett.*, vol. 24, no. 14, pp. 883–885, 1988.
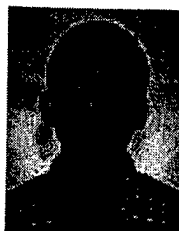
Daipayan Bhattacharya was born in Chandernagore, India, in November 1969. He received the B.S. and M.S. degrees in electrical engineering from the University of California, Los Angeles (UCLA), in 1990 and 1994, respectively. He is currenty pursuing the Ph.D. degree in electrical engineering at UCLA.

From 1990 to 1994, he was a Member of the Technical Staff in the Radar Laboratory at Hughes Missile Systems Group, Canoga Park, CA. His research interests include optical-millimeter wave interactions in solid-state devices and integration techniques for optoelectronic circuits and devices.
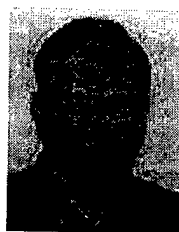

Hernan Erlig was born in Buenos Aires, Argentina, in 1969. He received the B.S. and M.S. degrees in electrical engineering from the University of California, Los Angeles (UCLA), in 1992 and 1996, respectively. He is currently pursuing the Ph.D. degree in electrical engineering.

His research interests include high-frequency characterization techniques for devices, ultrafast phenomena, device physics, and high-temperature superconductivity.

Mohammed E. Ali was born in Lalmonirhat, Bangladesh, in December 1967. He received the B.Sc. degree in electrical and electronic engineering from Bangladesh University of Engineering and Technology (BUET) in 1992 and the M.S. degree in electrical engineering from the University of California, Los Angeles (UCLA), in 1997. His thesis involved high-frequency optical mixing in three-terminal devices. He is currently pursuing the Ph.D. degree at UCLA.

From 1992 to 1994, he was a Lecturer with the Department of Electrical and Electronic Engineering, BUET. His research interests include generation of millimeter waves and characterization of high-speed devices using optical techniques.
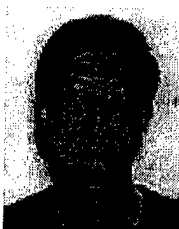
Shamino Wang was born in Taiwan in 1969. He received the B.S. degree in physics from the National Tsing Hua University, Taiwan, in 1992 and the M.S. degree in physics from the University of California, Los Angeles (UCLA), in 1994. He is currently pursuing the Ph.D. degree in physics at UCLA.
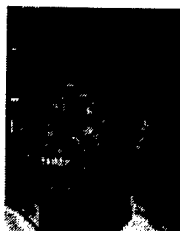
His research interests include CDMA optical fiber communication networks and microwave generation from common-ring cavity Brillouin lasers in optical fibers.

Richard Lai was born in Evanston, IL, in 1964. He received the B.S.E.E. degree from the University of Illinois Urbana-Champaign in 1986 and the M.S.E.E. and Ph.D. degrees from the University of Michigan, Ann Arbor, in 1988 and 1991, respectively.

He joined TRW's Advanced Microelectronics Laboratory, TRW Electronic Systems and Technology Division, Redondo, Beach, CA, in 1991 as a Product Engineer, where he has been involved in the research, development, and insertion of advanced GaAs-based and InP-based HEMT device and MMIC technologies into various military and commercial MMW applications. In 1994, he became the Principal Investigator for an advanced HEMT research and development project at TRW and has been heavily involved in supporting advanced HEMT MMIC production on TRW's flexible manufacturing line. He has authored and co-authored over 40 papers and conference presentations in the area of advanced GaAs and InP-based device and circuit technology.

Harold R. Fetterman (SM'81–F'90) received the B.A. degree in physics from Brandeis University, Waltham, MA, in 1962 and the Ph.D. degree from Cornell University, Ithaca, NY, in 1967.

After joining Lincoln Laboratory, Massachusetts Institute of Technology, Cambridge, he began to investigate new solid-state high-frequency devices. This included FET's, HEMT's, HBT's, quantum-well structures, and resonant tunneling structures. In 1982, he joined the University of California, Los Angeles (UCLA) Electrical Engineering Department as a Professor and First Director of the Center for High Frequency Electronics. During this period, he also became active in studying optoelectronics and optical control of millimeter wave devices. Currently, he has programs in investigating new polymer optical modulators, millimeter wave device concepts, and novel means of testing using laser techniques. He has helped organized many new activities including the Optically Controlled Phased Array Radar Project in the National Center for Integrated Photonics.

Dwight C. Streit (S'85–M'86–SM'92) received the Ph.D. degree in electrical engineering from the University of California, Los Angeles, in 1986.

He has since been with TRW's Electronic Systems and Technology Division, Redondo Beach, CA, where he is currently Assistant Manager of the Micro Electronics Product and Technology Development Department. He is a TRW Technical Fellow and Principal Investigator for several research and development projects related to III–V materials, monolithic HEMT–HBT integrated circuits, and quantum effect devices.

Optical mixing to 211 GHz using 50 nm gate pseudomorphic high electron mobility transistors

M. E. Ali, D. Bhattacharya, and H. R. Fetterman
Department of Electrical Engineering, University of California, Los Angeles, California 90095

M. Matloubian
Hughes Research Laboratories, Malibu, California 90265

We report optical mixing with difference frequencies to 211 GHz in 50 nm gate pseudomorphic InP-based high electron mobility transistors (HEMTs). To our knowledge, this is the highest frequency optical mixing signal obtained in three terminal devices. To detect the signals at these frequencies, a novel three-wave-mixing configuration was employed. To demonstrate the wide tunability of this setup, a sweep of frequencies from 160 to 190 GHz was performed. The optically generated millimeter wave signals were downconverted to 97 GHz and radiated. For the radiation experiments, tunable baseband signals were also added by injection into the gate terminal of our HEMTs, thereby providing a method to transmit information. © *1998 American Institute of Physics.* [S0003-6951(98)02404-8]

Optical mixing is a promising technique to generate continuously tunable millimeter wave frequencies. The generated signals are of high quality in terms of stability, noise, and spectral purity. Combined with optical fiber technology, this technique has applications in many important areas including phased array radar, remote sensing, spectroscopy and communications where optical fibers can serve as efficient, low loss transport, and distribution media. For photodetector applications, two-terminal devices have been mostly used, although three-terminal devices such as high electron mobility transistors (HEMTs)[1,2] and heterojunction bipolar transistors[3,4] are becoming increasingly competitive, due to their inherent gain. The presence of a third terminal also adds a degree of freedom in controlling the mixing process. In particular, the gate can be employed to introduce a baseband information signal for upconversion to a millimeter wave carrier, which is optically generated in the same device.

Recently, we have demonstrated optical mixing with difference frequencies to 130 GHz in 1 μm gate-length epitaxial liftoff HEMTs.[5] In this letter, we report the extension of this mixing to a record high of 211 GHz using 50 nm gate pseudomorphic AlInAs/GaInAs/InP HEMTs. The high frequency optically generated signals are detected using a broadband three-wave mixing technique. A sweep over the frequency range of 160–190 GHz was performed to demonstrate the tunability of our heterodyne system.

In our second set of experiments, 97 GHz optically generated signals were radiated into free space by way of a coplanar-to-waveguide transition and a radiating horn. The 210 GHz mixed signals were also radiated after downconversion to 97 GHz. This demonstration validated the concept that by using suitable antenna structures integrated with the device, these high frequencies could be directly radiated. Further integration with semiconductor lasers can be a cost effective way of making compact optoelectronic millimeter wave sources. Enabling integration techniques, such as epitaxial liftoff and integrated slot antennas, are being investigated for such applications.[6] Finally, using the gate terminal, tunable electrical sidebands were superimposed on the 97

GHz optically generated signal and then radiated into free space to demonstrate transmission of information using fiber-millimeter wave links.

The devices used in our experiments were 50 nm gate-length delta-doped pseudomorphic AlInAs/GaInAs/InP HEMTs.[7,8] The structure had a sheet-charge density of approximately 2.7×10^{12} cm^{-2} and a channel mobility of approximately 13 000 cm^2/V s at 300 K. On wafer electrical characterization of the devices was performed on a HP8510C vector network analyzer from 0 to 50 GHz. A millimeter wave extension kit utilizing frequency multipliers and external harmonic mixers was also used to further extend the *s*-parameter measurements to *W* band (75–110 GHz). The short circuit current gain and unilateral power gain for our HEMTs are shown in Fig. 1. The device was biased at $V_{DS}=0.7$ V and $V_{GS}=0.0$ V. The devices showed excellent gain response characteristics. A cutoff frequency, f_T of 228 GHz and a maximum oscillation frequency, f_{max} of 124 GHz were obtained from extrapolation of the measured gain characteristics.

The dc responsivity and quantum efficiency for our devices were measured to be 74 A/W and 145, respectively. The overall responsivity was 2 A/W when external coupling losses were included. The coupling efficiency was estimated to be 2.7%. Quantum efficiencies greater than 100% can be achieved, since in HEMTs the photogenerated holes participate in a current gain mechanism that results in an injection of additional electrons in the channel layer.

In our optical mixing experiments, the HEMT was illuminated with two collinear optical beams with a desired frequency offset. The mixing current at the difference frequency, ω_b is

$$i_{ac}(t)=2F(\omega_b)\sqrt{P_1 P_2}\cos(\omega_b t),\qquad(1)$$

where $F(\omega_b)$ is the ac responsivity of the device, P_1 and P_2 are incident optical powers. The high frequency limit of the mixing process is set by the dynamic photoresponse, $F(\omega_b)$ of the device.
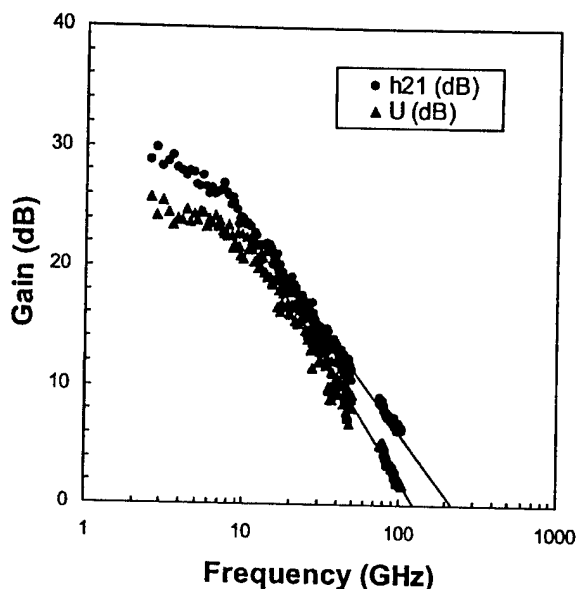
FIG. 1. Electrical gain measurements (unilateral power gain, U, and short-circuit current gain, h_{21}) for the HEMTs were performed on an extended 8510C vector network analyzer from 0 to 50 GHz and 75–110 GHz. From extrapolation of the data, f_{max} is found to be 124 GHz and f_T is found to be 228 GHz.

The signal and local oscillator fields used in our optical mixing experiments were obtained from a temperature stabilized single frequency HeNe laser and an Argon pumped continuous wave ring dye laser, respectively. The dye laser was operated with Kiton Red 620 dye (600–640 nm) and had the capability to tune mechanically hundreds of GHz, and electronically 30 GHz around the wavelength of HeNe (632.991 nm). The optical power incident on the device from the HeNe was 0.5 mW. A variable attenuator was used in the dye laser path to limit the incident dye laser power on the device to a few milliwatts. The incident dye laser power was kept low to avoid saturation of the device and to obtain good modulation depth. A 5X objective lens was used to focus the optical radiation on the device in this free space implementation. Fiber optic connections have also been demonstrated and will be used in our next extension to submillimeter wave frequencies.

To contact our devices, we used high frequency commercial coplanar probes and bias tees. The probes, which were coupled to waveguides, acted as well matched antennas for our devices throughout W band. To overcome the bandwidth limitations imposed by use of the probes, a three-wave mixing technique was employed. For this configuration, a millimeter wave signal of frequency ω_g was injected into the gate of the device. The interaction between the modulation induced by this signal and the optically generated signal produced a down-converted signal of frequency $\omega_{rf} = \omega_b - \omega_g$, as well as other mixing products. The frequency of the gate signal was chosen such that ω_{rf} fell within the detection bandwidth of our external receiver system. A backward wave oscillator (BWO) tunable over the entire band was used as a millimeter wave source for the gate signal.

The three-wave mixing technique took advantage of the multifunction capability of the HEMTs. The interaction of two optical waves and an electrical signal injected into the
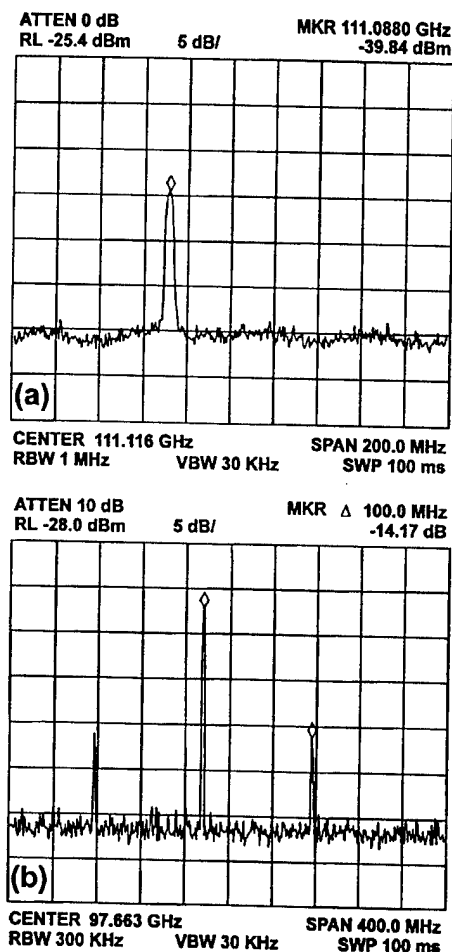

FIG. 2. (a) Spectrum analyzer trace of the 211 GHz optically generated signal which has been downconverted to 97 GHz in the HEMTs and heterodyne detected in our millimeter wave receiver. (b) Baseband information signals imposed on a 97 GHz optically generated carrier by injection into the gate terminal of our device.

gate can be considered as a hybrid of two different processes, optical mixing, and electrical down-conversion. The first process makes use of the quadratic response of the device to coherent optical fields, as described in Eq. (1). The optically generated current is then modulated by the injected electrical gate signal, producing a sum and difference frequency component:

$$i(t) = 2F(\omega_b)\sqrt{P_1 P_2}\cos(\omega_b t)A\cos(\omega_g t)$$
$$= AF(\omega_b)\sqrt{P_1 P_2}[\cos(\omega_b + \omega_g)t + \cos(\omega_b - \omega_g)t].$$

(2)

Our millimeter wave receiver filters the sum component and detects the difference frequency for display on a spectrum analyzer.

Both mixing processes were observed to be strongly dependent on the operating bias point. The strength of the optical mixed signal depends upon the photocurrents present in the active layer. This mixing photocurrent was usually optimized by operating the device at a higher drain voltage and at a gate voltage close to zero. On the other hand, efficient down-conversion is obtained when the device nonlinearity is more pronounced. This usually happens when the device is
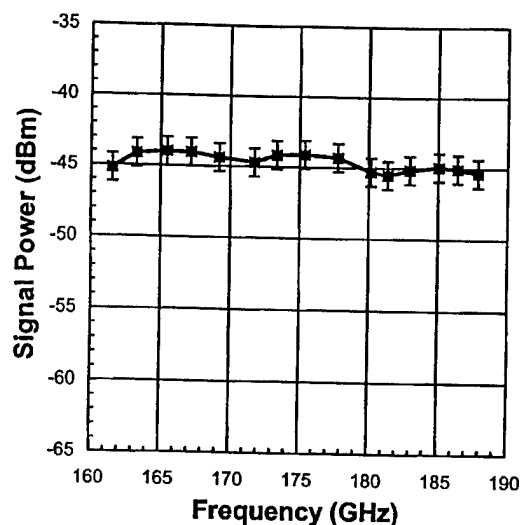
FIG. 3. Swept frequency optical heterodyne measurements on the HEMTs from 160 to 190 GHz, demonstrating the wide tunability of our system.

biased at drain voltage just before the onset of saturation. Therefore a compromise has to be made in choosing the bias point when the two processes are occurring simultaneously.

In our first set of measurements, we detected an optical mixed signal at 211 GHz in our HEMTs with the BWO frequency set to 114 GHz. The down-converted 97 GHz signal was radiated and launched into the waveguide input of the external receiver system using the coplanar probes as antenna elements, as described above. A spectrum analyzer trace of the signal is shown in Fig. 2 (a). A 16 dB signal-to-noise ratio was achieved with the device's bias optimized at $V_{DS}=0.6$ V and $V_{GS}=0.1$ V.

To demonstrate the wide tunability of our optical mixing signal, we performed a sweep from 160 to 190 GHz. In order to minimize the effect of the external receiver system on our measurements, the frequency of the down-converted signal in the device was kept constant at 76 GHz throughout the sweep by simultaneously tuning the dye laser frequency and the BWO frequency. The BWO power applied to the gate and the incident optical power were also kept constant while tuning. The device was biased at $V_{DS}=0.7$ V and $V_{GS}=-0.2$ V. The response of the device is shown in Fig. 3. The excellent response suggests that these devices can be used to generate frequencies much higher than 211 GHz by optical mixing.

Having demonstrated high frequency optical mixing we then examined the radiation and propagation of the optically generated signals in free space. In this set of measurements, the optically generated millimeter waves were fed to a radiating horn antenna via the coplanar probes. The free space radiation was then collected using a horn antenna and de-tected in our millimeter wave receiver system. Initially, an optical beat signal of 97 GHz was generated in the device and radiated. The signal-to-noise ratio of the detected signal was 24 dB. The 211 GHz optical mixed signal was also generated, downconverted to 97 GHz, and then radiated. In this case, a signal-to-noise ratio of 12 dB was achieved. This validates the use of these devices as compact optically controlled millimeter wave sources. Future integration with on wafer antennas using epitaxial liftoff technology is currently being pursued to radiate the 211 GHz signals directly.

Lastly, to demonstrate the viability of transferring information using our heterodyne system in an optical-millimeter wave link, a 100 MHz rf signal was imposed on a 97 GHz optically generated carrier. To impress the information signal on the carrier it was injected into the gate of the HEMT. This highlights a unique advantage of using three-terminal devices over two-terminal devices for optical-millimeter wave applications. The modulated millimeter wave signal was then radiated into free space as described above and collected in our heterodyne receiver. The detected signal is shown in Fig. 2(b). The sidebands were 14.2 dB down from the carrier for a rf signal power of 0 dBm. The rf signal frequency was swept over a few hundred MHz and no appreciable change in sideband strength was observed.

In conclusion, we have demonstrated the mixing of two continuous wave laser beams in 50 nm gate pseudomorphic HEMTs to generate continuously tunable mixed signals to 211 GHz. A sweep performed over the frequency range from 160 to 190 GHz indicated that these devices have excellent optical response characteristics. Optically generated signals, both continuous wave and modulated, were radiated into free space at 97 GHz using a horn.

[1] D. Bhattacharya, M. E. Ali, H. R. Fetterman, and D. Streit, Conference Proceedings of the 9th Annual Meeting of the IEEE Lasers and Electro-Optics Society (1996), Vol. 2, p. 326.
[2] M. A. Romero, M. A. G. Martinez, and P. R. Herczfeld, IEEE Trans. Microwave Theory Tech. 44, 2279 (1996).
[3] D. C. Scott, D. V. Plant, and H. R. Fetterman, Appl. Phys. Lett. 61, 1 (1992).
[4] L. E. M. de Barros, A. Paolella, P. R. Herczfeld, and A. A. A. de Salles, IEEE MTT-S International Microwave Symposium Digest 3, 1445 (1996).
[5] D. Bhattacharya, H. Erlig, M. E. Ali, S. Wang, H. R. Fetterman, R. Lai, and D. Streit, IEEE J. Quantum Electron. 33, 1507 (1997).
[6] D. Bhattacharya, P. S. Bal, H. R. Fetterman, and D. Streit, IEEE Photonics Technol. Lett. 7, 1171 (1995).
[7] L. D. Nguyen, A. S. Brown, M. A. Thompson, and L. M. Jelloian, IEEE Trans. Electron Devices 39, 2007 (1992).
[8] S. E. Rosenbaum, B. K. Kormanyos, L. M. Jelloian, M. Matloubian, A. S. Brown, L. E. Larson, L. D. Nguyen, M. A. Thompson, L. P. B. Katehi, and G. M. Rebeiz, IEEE Trans. Microwave Theory Tech. 43, 927 (1995).

Ali *et al.*

3 PIEPER W., WEICH. K., LUDWIG. R., PATZAK. E., and WEBER. H.G.: 'All-optical polarization and wavelength independent 3R signal regenerator'. Tech. Dig. (Post-Deadline) OFC'96. 1996. Paper PD35. p. 35-1 (part B)

4 BIGO S., LECLERC O., BRINDEL. P., VENDROME. G., and DESURVIRE. E.: '20Gbit s all optical regenerator'. Tech. Dig. (Post-Deadline) OFC'97. 1997. Paper PD22. p. 22-1

5 JEPSEN K.S., CLAUSEN. A.T., MIKKELSEN. B., POULSEN. H.N., and STUBKJAER. K.E.: 'All-optical network interface for bit synchronisation and regeneration'. Proc. (Post-Deadline) ECOC'97. 1997. Paper Th3C8. Vol. 5. p. 89

6 JOERGENSEN. C., DANIELSEN. S.L., HANSEN. P.B., STUBKJAER. K.E., SCHILLING. M., DAUB K., LACH. E., LAUBE. G., IDLER. W., and WUNSTEL. K.: 'All-optical 40Gbit s compact integrated interferometric wavelength converter'. Tech. Dig. OFC'97. 1997. Paper TuO1. p. 72

7 MIKKELSEN. B., DANIELSEN. S.L., JOERGENSEN. C., PEDERSEN. R.J.S., POULSEN. H.N., and STUBKJAER. K.E.: 'All-optical noise reduction capability of interferometric wavelength converters'. Electron. Lett.. 1996. 32. (6). pp. 566-567

150Gsample/s wavelength division sampler with time-stretched output

A.S. Bhushan, F. Coppinger, B. Jalali, S. Wang and H.F. Fetterman

A new technique for optical sampling and time stretching of an analogue signal is presented. The signal is 'wavelength stamped' by a chirped optical pulse. An arrayed waveguide grating provides parallel time-interleaved samples as well as a time-stretched serial sampled waveform.

High-speed analogue-to-digital conversion systems require sampling techniques that have high temporal resolution and fast sampling rates. Also of great importance is a mechanism for demultiplexing or slowing the samples in time as they approach the electronic quantiser. If time could be mapped onto wavelength, then the problem of demultiplexing in time could be translated into a problem of demultiplexing in wavelength. The latter can be resolved easily by using just passive optical filters. Time-to-wavelength mapping by mixing a chirped pulse with a digital data stream has been used to demultiplex digital serial data [1]. Chirping a broadband transform-limited pulse separates different spectral components of the pulse in time. When the chirped pulse enters the mixer, different wavelength components arrive sequentially. Thus, time is mapped into the optical wavelength. This technique has also been applied to transmission of WDM data [2] and to sample analogue signals [3, 4]. In this Letter, we demonstrate a novel sampling architecture based on two complimentary concepts. The first is the chirped-pulse time-to-wavelength transformation. The second is the use of discrete dispersion, obtainable with an arrayed waveguide grating (AWG) [5], to slow down the sampled waveform.
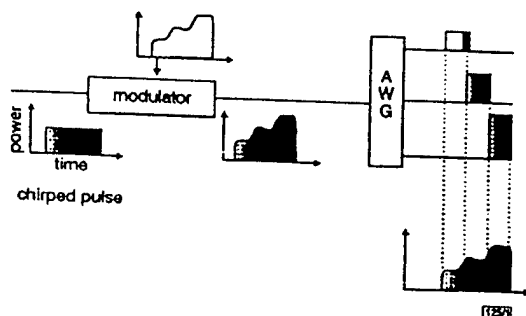

Fig. 1 *Wavelength division sampling*

Different shades of grey represent different wavelengths

The chirped pulse sampling is shown in Fig. 1. To generate chirped pulses, we use a passively modelocked erbium-doped fibre

laser (EDFL) with 160fs FWHM 25MHz pulses followed by dispersion in a singlemode fibre (SMF, $D = 17$ps/nm.km). Sampling is performed by a silica AWG with a channel spacing of 0.8nm and a passband of 0.3nm. The electrical signal and the chirped pulse interact in the optical modulator to produce a 'wavelength stamped' intensity-modulated optical signal. The AWG samples the optical spectrum and thus samples the time evolution of the electrical transient. In Fig. 2, we report the timing measurements for a chirp of 120ps/nm (7km of SMF). Outputs from individual AWG ports are photodetected and displayed using a digital-sampling oscilloscope. The pulse-to-pulse spacing of 100ps in Fig. 2 corresponds well to the channel spacing of 0.8nm for the AWG.
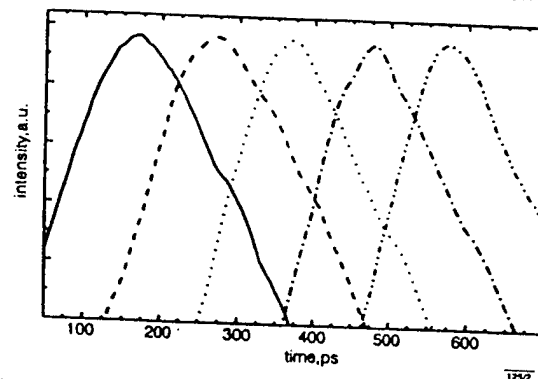

Fig. 2 *Timing measurements at 10Gsample/s*
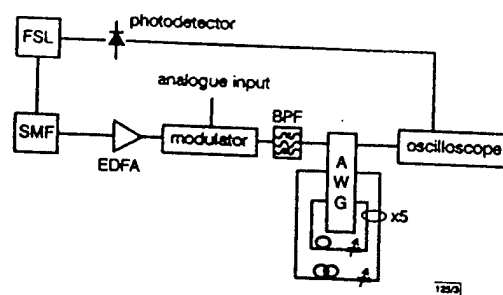
Each trace is a different output of the AWG

Fig. 3 *Experimental setup*

FSL denotes femtosecond laser

The setup for the 150Gsample/s experiment is shown in Fig. 3. The transform-limited pulse from the EDFL was dispersed through a Corning SMF to produce a chirped pulse. A portion of the femto-second laser output is fed to a photodetector to provide the synchronising clock for the entire system. The chirped pulse is modulated and then fed to an 8-channel silica AWG. A 5nm bandpass filter precedes the AWG so that the serialised output contains only one free spectral range of the AWG. The outputs of the AWG are fed back to the corresponding inputs with incremental delays of around 1.3ns. This feedback architecture provides discrete dispersion and separates samples in time. In an analogue-to-digital (A/D) converter system, a single slow electronic quantiser can then be used to digitise a fast electrical transient. The feedback paths include variable attenuators to provide spectral equalisation. Spectral equalisation can also be attained by using a dispersion-decreasing super-continuum fibre [6] or by a feed forward architecture [2]. The sampling rate is given by $f_s = 1/\Delta\lambda. D$, where $\Delta\lambda$ is the AWG channel spacing and D is the total dispersion. We use a 500m spool of fibre for dispersion corresponding to a chirp rate of 8.5ps/nm at the modulator input. The pulse separation (in time) at the output of each AWG channel is 6.8ps, corresponding to a sampling rate of 147Gsample/s. The response time of the photodetector (30ps) and the jitter noise in the measuring electronics (1.3ps) make measuring the actual pulse-to-pulse separation difficult. However, the separation between the first and the last channel outputs (before feedback) was measured to be 32ps, which corresponds to an average pulse separation of 6.4ps. Fig. 4 shows the time-stretched serialised output. The output rate is reduced from 147GHz to 770MHz by 1.3ns incremental delays in

474

the feedback path. Since the modulator bandwidth is limited to 10GHz, we demonstrate the sampling by keeping the modulator at different DC biases (1V top trace, 8V bottom trace). The signal-to-noise ratio (SNR) reflected in the nonuniformity in the sample stream is 14dB. In general, the SNR has a contribution from the spectral nonuniformity (from laser and AWG) as well as crosstalk within the AWG. Since the measured AWG optical crosstalk is 27dB, we conclude that the measured SNR is limited by the incomplete spectral equalisation, which can be improved with higher quality attenuators.
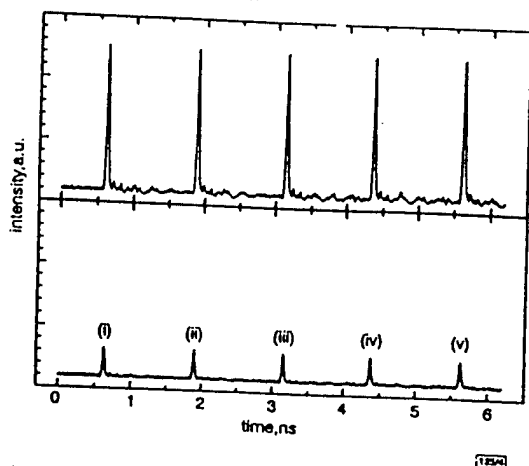

Fig. 4 *Time stretched and serialised output for 147Gsample/s sampling*

Modulator voltage = 1V (top trace) and 8V (bottom trace)
$V\pi = 10V$
(i) $\lambda = 1565.4$nm
(ii) $\lambda = 1566.2$nm
(iii) $\lambda = 1567$nm
(iv) $\lambda = 1567.8$nm
(v) $\lambda = 1568.6$nm

In summary, we have demonstrated a novel optical sampling method. The chirped pulse technique provides time-interleaved samples compatible with interleaved A/D architecture. Using an AWG in a recirculating configuration, a stream of samples can be stretched in time and serialised, allowing an ultra-fast electrical transient to be digitised with a single slow A/D.

References

1 MORIOKA, T., KAWANISHI, S., TAKARA, H., and SARUWATARI, M.: 'Multiple-output, 100Gbit/s all-optical demultiplexer based on multichannel four-wave mixing pumped by a linearly-chirped square pulse', *Electron. Lett.*, 1994, 30, (23), pp. 1959–1960
2 CUNDIFF, S.T., KNOX, W.H., and NUSS, M.C.: 'Active feed-forward channel equalisation for chirped pulse wavelength division multiplexing', *Electron. Lett.*, 1997, 33, (1), pp. 10–11
3 VLADMANIS, J.A.: 'Real time picosecond optical oscilloscope' *in* FLEMING, G.R., and SIEGMAN, A.E. (Eds.): 'Ultrafast Phenomena V' (Springer-Verlag, Berlin, 1986)
4 FRANKEL, M.Y., KANG, J.U., and ESMAN, R.D.: 'High-performance hybrid analog-digital converter based on time-wavelength mapping'. LEOS 1997, postdeadline paper
5 YEGNANARAYANAN, S., TRINH, P.D., and JALALI, B.: 'Recirculating photonic filter: a wavelength-selective time delay for phased-array antennas and wavelength code-division multiple access', *Opt. Lett.*, 1996, 21, (10), pp. 740–742
6 MORI, K., TAKARA, H., KAWANISHI, S., SARUWATARI, M., *et al.*: 'Flatly broadened supercontinuum spectrum generated in a dispersion decreasing fibre with convex dispersion profile'. *Electron. Lett.*, 1997, 33, (21), pp. 1806–1808

160Gbit/s (8 × 20Gbit/s) soliton WDM transmission experiments using dispersion flattened fibre and periodic dispersion compensation

M. Suzuki, I. Morita, K. Tanaka, N. Edagawa, S. Yamamoto and S. Akiba

160Gbit/s (8 × 20 Gbit/s) soliton WDM signals were successfully transmitted over 4000km with a BER of < 10⁻⁹, by using periodically dispersion-compensated dispersion-flattened fibre with an average dispersion slope of 0.0005ps/km/nm².

Soliton-WDM transmission is attractive for large-capacity long-haul optical transmission systems because soliton-based systems have the potential to carry higher bit rate signals than NRZ systems. The key technological issues in soliton WDM transmission are the reduction of collision-induced timing jitter, four-wave mixing [1] and the dispersion slope of the transmission fibre [2]. The first two requirements can be achieved using dispersion tapered fibre spans with soliton control techniques [3, 4]. To overcome the impact of the dispersion slope, the use of dispersion-flattened fibre seems quite attractive and practical compared with a channel-by-channel dispersion compensation scheme [2, 4]. So far, we have made a preliminary report on the effectiveness of the soliton WDM systems using dispersion-flattened transmission fibre and 80Gbit/s (4 × 20Gbit/s) signals [5]. In this Letter, we show the experimental results on 160Gbit/s (8 × 20 Gbit/s) soliton WDM transmission over 4000km using dispersion-flattened fibre with periodic dispersion compensation with a wavelength bandwidth of 11.2nm.
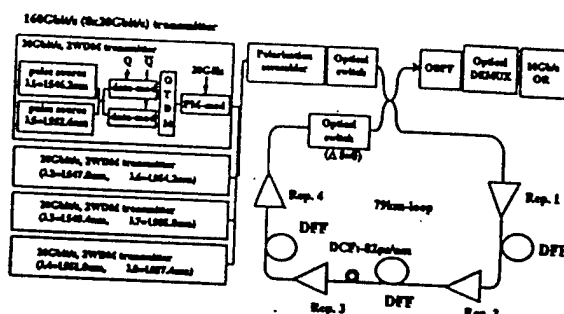

Fig. 1 *Experimental setup of 160Gbit/s (8 × 20Gbit/s) soliton WDM transmission*

Fig. 1 shows a schematic diagram of the experimental setup for eight-channel 20Gbit/s soliton WDM transmission. We used four 2WDM×20 Gbit/s transmitters as a 160Gbit/s transmitter. The wavelengths of eight channels, ranging from 1546 to 1558nm, were equally spaced by 1.6nm. Each 2WDM transmitter consists of two EA-modulator-based soliton pulse generators with different wavelengths. A 20Gbit/s optical soliton data stream was produced by using two LiNbO₃ intensity modulators operated at 10Gbit/s by a 2¹¹ − 1 pseudorandom binary sequence and optical time division multiplexing. The pulse width obtained was from 10 to 15ps. In addition, each 20Gbit/s signal was modulated at 20GHz by an LiNbO₃ phase modulator to improve the transmission performance [6, 7]. After combining eight 20Gbit/s signals so that the adjacent channels were orthogonally polarised, a polarisation scrambler was used to suppress the PHB of the EDFA repeaters. The transmission line comprises three spans of ~27km long dispersion-flattened fibre (DFF) and dispersion-compensation fibre (DCF). The loss of the DFF spans, including the splicing loss, was still large and the average span loss was ~9dB. The average dispersion slope of the DFF was 0.0005ps/km/nm² and the average chromatic dispersion of the DFF at 1555nm was 1.1ps/km/nm. The accumulated chromatic dispersion of the loop was compensated for by the DCF with −82ps/nm and the residual dispersion in the loop was 0.02ps/km/nm. As a frequency guiding filter, an FP-etalon filter (*FSR* = 1.6nm) was placed in the loop to stabilise the transmission performance. In the receiver, the desired channel was selected by optical bandpass filters and the transmitted 20Gbit/s signals were optically time-division-demultiplexed to a 10Gbit/s

Optically Controlled Serially Fed Phased Array Sensor

David A. Cohen, Yian Chang, A. F. J. Levi, Harold R. Fetterman, *Fellow, IEEE*, and Irwin L. Newberg, *Member, IEEE*

Abstract—A new type of RF-photonic sensor design which uses an optical serially fed phased array is proposed for applications in radar and communication systems. This sensor has the advantages of true time delay and yet only requires one tunable laser and one fiber optic grating delay for beam steering. In addition to discussing the system operation in transmit and receive modes, we also present initial experiments establishing the viability of the basic serial-feed design approach.

I. INTRODUCTION

WE propose a new photonic system suitable for RF phased array sensors. This system uses a serial-feed concept that represents a major simplification in both optical and microwave components compared with conventional parallel systems [1]–[6]. Our system provides both phase delay and true-time delay (TTD) for beam steering and requires only a single tunable laser, optical modulator, and time-delay element [7]. In this paper, we present descriptions of transmit (XMIT) and receive modes as well as initial experimental data establishing the viability of this approach. In our design, the use of fiber-optic techniques, such as long and low-loss delay lines, is intrinsic to the operation of the system. It is predicated upon using the pulsed nature of most microwave sensors in a manner similar to clocked systems used in digital configurations. Precise timing control of photonic signals is used to distribute RF pulses with time/phase delay information to each element in a radiating/receiving array.

II. TRANSMIT MODE

To describe the proposed mechanism of operation, we divide the XMIT function into two parts: the timing unit and the tapped optical delay line feed. The timing unit is shown in Fig. 1(a). The most technologically intensive component, the fast and broad-band tunable laser shown on the left, can rapidly change its wavelength by at least 20 nm using proper current adjustment [8]. A typical laser of this type can be electronically tuned in less than a nanosecond. Using an optical modulator,

D. A. Cohen and A. F. J. Levi are with the Department of Electrical Engineering, University of Southern California, Los Angeles, CA 90089-1111 USA.

Y. Chang and H. R. Fetterman are with the Department of Electrical Engineering, University of California at Los Angeles, Los Angeles, CA 90095 USA.

I. L. Newberg is with Radar and Communication Systems, Hughes Aircraft Company, Los Angeles, CA 90009-2426 USA.
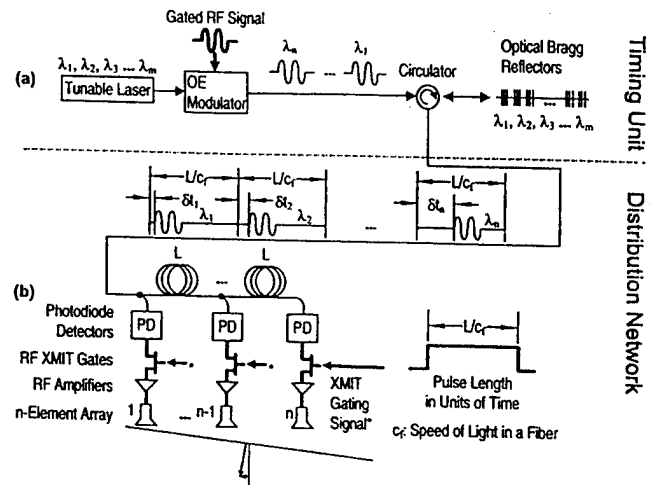
Fig. 1. Basic XMIT mode implementation for array of n elements. (a) The timing unit uses only one laser, one optical modulator, and one delay element. (b) Tapped optical delay line used as the distribution network to demultiplex serial pulses into parallel ones.

light from the laser is amplitude modulated at the desired microwave operating frequency and is gated at the radiated pulse width. After leaving the modulator, lasing light passes through an optical circulator and then into a fiber grating. Reflected light from the grating returns to the circulator and is directed onto a tapped optical delay line as shown in Fig. 1(b).

The timing information is obtained via the fiber grating which yields a wavelength-selective propagation delay for each gated pulse. Although our initial efforts use a grating with discrete wavelength selectivity, the system may alternately incorporate a continuously chirped grating or multiple gratings in parallel to enhance the time resolution. A laser which can be tuned continuously over a 20-nm range and fiber grating reflectors with a 0.3-nm FWHM linewidth (corresponding to a 53-GHz bandwidth) allow access to at least 60 different time delays with time-delay accuracy around 1 ps. Each serially fed optical pulse has a unique time delay relative to the RF pulse gate timing. It is these TTD's that control the pointing direction of our phased array. The number of pulses in the fully loaded line corresponds to the number of radiating elements in the array (or subarray). The wavelength stability needed in the system can be readily achieved by maintaining the temperature fluctuations to within 1 °C [5]. Note that this task is much easier in our system than in others because fewer active elements and passive delay elements are used.

The tapped delay line consists of a fiber having equally spaced taps; each tap is connected to an optical detector. The

optical propagation time between these taps corresponds to the length of the longest radiated pulse. It is important to note that the inter-tap delay time in this approach must equal to (or an integral multiple of) the RF pulse gate period. From the circulator, each gated pulse will arrive, with the additional delay for beam steering imposed by the fiber grating, simultaneously at the intended tap on the delay line. Essentially, the delay line "stores" the pulses until it is fully loaded with the correct pulse adjacent to each tap. At this moment, the microwave signal from the optical detector, located at each tap in the fiber manifold feed, is switched to the antenna element and all pulses on the line are radiated simultaneously. Each antenna element's microwave pulse has the correct time delay, as set by the fiber's Bragg grating reflector, to form a radiating beam in a desired direction. There is complete freedom in choosing this direction constrained only by the number of available laser wavelengths and associated Bragg grating reflectors. After the signal is radiated, the detector outputs are simultaneously switched away from the antenna elements and the fiber manifold feed can be reloaded. Due to the power splitting along the tapped delay line, each photodetector receives $1/n$ of the useful optical power, where n is the number of radiating elements. This corresponds to a $-10 \, \text{Log} n$ dB of optical power loss for each element. For a practical size ($n \approx 100$) of subarray or array, this loss can be compensated by a single optical amplifier ($+20$ dB or more) if necessary. For quasi-CW transmit or receive mode systems, a modification of the basic system permits each optical pulse to be accessed in turn by each element and each element takes $1/n$ of the optical power. No optical power is lost in these cases.

III. EXPERIMENTAL DATA

Instead of using a tunable laser, it is possible to use arrays of lasers, including VCSEL's, that are switched on and off to obtain a large set of precise optical wavelengths [9]–[10]. To evaluate the basic concept of wavelength controlled time delays in our serially fed system, we have performed a prototype experiment using two 1.3-μm DFB lasers and a ten-grating reflector fiber. These lasers are tuned to different grating reflectors on a single-mode fiber separated by 1.7 mm corresponding to 17.5 ps round-trip delay. The lasers are alternately switched on and off as shown in Fig. 2(a). In this example, pulse widths are approximately 6 ns with the complete switching time occupying less than 1 ns. There is no fundamental limit to the length of the pulses used in this experiment; 6 ns was only chosen for convenience. In Fig. 2(b), we show the time-averaged optical spectrum after 10-GHz microwave modulation and reflection from the grating. The typical -35-dB side-mode suppression in the DFB laser is enhanced by a few decibels after passing through the fiber grating. This is due to the fact that the reflection wavelength of the neighboring line does not overlap with the DFB's natural subsidiary maxima. Therefore, we obtain about -40 dB (-80 dB electrical) optical purity which can contribute to the signal-to-noise performance of the system. No other significant reflections have been noted from the terminated fiber grating.
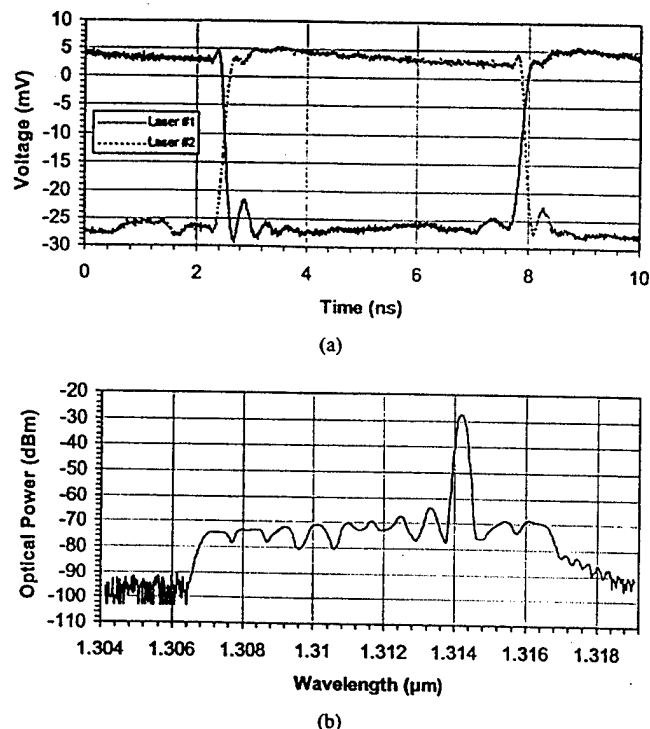

Fig. 2. (a) Laser #1 (solid line) with emission wavelength λ_1 and Laser #2 (dotted line) with emission wavelength λ_2 are alternately switched on and off with pulse widths about 6 ns and switching time less than 1 ns. (b) The optical spectrum of λ_1 after reflection from the fiber grating for the case of 10-GHz modulation. This shows the spontaneous emission background level resulting from reflection of the other grating reflectors is 40 dB below the desired signal.

Measurements have been made at 3, 10, and 18 GHz to examine the precision and switching dynamics of the fiber-optic TTD timing unit. Fig. 3(a) shows the output of a digital sampling oscilloscope with a 3-GHz RF signal which was analyzed, by best-fitting sine functions, to have a TTD of 17.5 ps. The figure shows that the system can be effectively switched in less than 1 ns. The oscilloscope is triggered with the same synthesizer driving the modulator. The results at 10 GHz [Fig. 3(b)] have a TTD = 17.5 ps. This experiment was also repeated at 18 GHz and yielded a phase shift of 110° as shown in Fig. 3(c). Finally, by switching to another grating reflector on the fiber corresponding to a TTD = 54.9 ps, a phase shift of 200° at 10 GHz was obtained as shown in Fig. 3(d).

These measurements demonstrate that wavelength switching speeds and the reproducibility required for the laser can be obtained using commercially available components. These results also establish that existing fiber grating delay lines offer sufficiently high contrast ratios to limit the background scattered light level in the system. Note that an electrical phase noise ratio of better than 80 dB is outstanding for such a system.

IV. RECEIVE MODE

In the receive mode, only the RF phase is required at each antenna element for a given direction of observation, there is no optical or microwave pulse gating. Using the same timing unit and tapped delay line as in XMIT mode, local oscillator
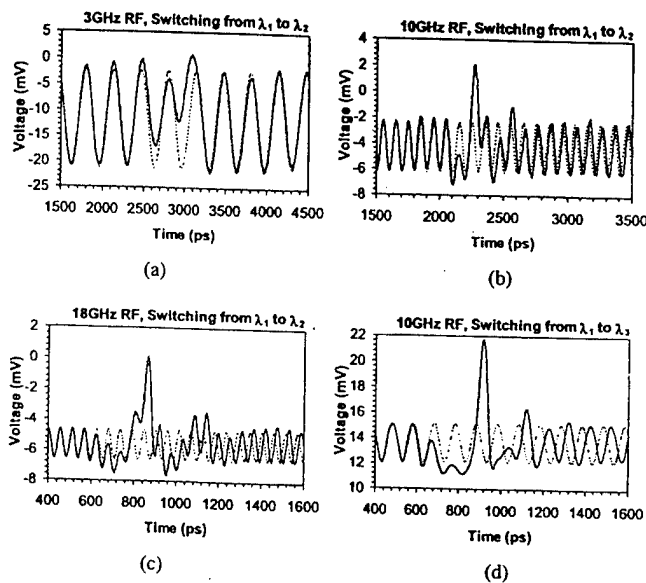
Fig. 3. Solid lines: Detected signals showing wavelength switching. Dotted lines: Sine-fit to the λ_1 RF signals: (a) 3-GHz RF signal with switched true-time delay (TTD) equal to 17.5 ps, obtained by best-fitting of sine functions on a smaller time scale setting. This TTD corresponds to an 18° phase change at 3 GHz. Switching time is less than 1 ns. The signal is inverted due to the RF amplifier. (b) 10-GHz RF signal with switched TTD = 17.5 ps. This TTD corresponds to a 63° phase change at 10 GHz. (c) 18-GHz RF signal with switched TTD = 17.5 ps. This TTD corresponds to a 110° phase change at 18 GHz. (d) 10-GHz RF signal with switched TTD = 54.9 ps. This TTD corresponds to a 200° phase change at 10 GHz.

(LO) signals, in exact reverse phase as used to transmit the beam, are supplied to mixers located at each antenna element. The received signal at each antenna is the other input to each mixer.

Essentially, the receiver we propose utilizes the conjugate phase delays to yield the equivalent of a configurable matched filter. Thus, in our system, the signals from the XMIT photodiodes are fed to a mixer which homodynes this optically generated microwave LO signal with the received microwave signal. The signals, mixed to baseband, from each antenna element are then added coherently in a simple summed signal processor to form the received antenna beam signal. For a combined XMIT and receive system, an electronic switch could be used between XMIT and receive functions to allow the same timing unit and optical feed to be used to generate RF signals with steering phases for XMIT and receive. A laser may also be used to transmit the composite summed baseband signal to a remote site for further processing and display.

It is important to note that these delayed RF signals, generated by laser tuning and grating delay, have a RF phase characteristic of a true-time delay system. This yields a wide tuning frequency bandwidth capability for constant pointing.

The technique is relatively simple and capable of steering the receive beam through all angles as in the XMIT mode. The proposed system can meet the RF performance specifications of a large subset of potential users. By using two parallel delay lines the duty cycle can be increased to essentially 100% as in the XMIT mode.

V. CONCLUSION

A novel serially fed TTD system has been proposed and the basic concept has been experimentally verified. The system we have presented is a RF sensor implementation based upon a serial-feed. It uses only one tunable laser, modulator, and delay element to achieve completely addressable beam steering. The system is scaleable and additional lasers and fibers can be used in a parallel configuration to increase the number of available bits and time resolution. The system is also versatile and can be used to control both one- and two-dimensional arrays as well as multibeam systems. Because the amplitude and time delay for each radiating element is completely programmable, arbitrary beam forming is possible. Thus, by using the natural timing of pulsed RF systems, we are able to greatly simplify, to reduce the cost, and to increase the flexibility of optically controlled radar, communication, and electronic warfare applications.

REFERENCES

[1] D. Dolfi, P. Joffre, J. Antoine, J.-P. Huignard, et al., "Photonics for phased array radars," Proc. SPIE—Int. Soc. Opt. Eng., vol. 2560, pp. 158–165, 1995.

[2] H. R. Fetterman, Y. Chang, D. C. Scott, S. R. Forrest et al., "Optically controlled phased array radar receiver using SLM switched real time delays," IEEE Microwave Guided Wave Lett., vol. 5, pp. 414–416, 1995.

[3] L. Xu, R. Taylor, and S. R. Forrest, "True time-delay phased-array antenna feed system based on optical heterodyne techniques," IEEE Photon. Technol. Lett., vol. 8, pp. 160–162, 1996.

[4] R. D. Esman, M. Y. Frankel, J. L. Dexter, L. Goldberg et al., "Fiber-optic prism true time-delay antenna feed," IEEE Photon. Technol. Lett., vol. 5, pp. 1347–1349, 1993.

[5] L. J. Lembo, T. Holcomb, M. Wickham, P. Wisseman, and J. C. Brock, "Low-loss fiber optic time-delay element for phased-array antennas," Proc. SPIE—Int. Soc. Opt. Eng., vol. 2155, pp. 13–23, 1994.

[6] A. Molony, C. Edge, and I. Bennion, "Fiber grating time delay element for phased array antennas," Electron. Lett., vol. 31, no. 17, pp. 1485–1486, 1995.

[7] G. A. Ball, W. H. Glenn, and W. W. Morey, "Programmable fiber optic delay line," IEEE Photon. Technol. Lett., vol. 6, pp. 741–743, 1994.

[8] M. Schilling, W. Idler, E. Kuhn, G. Laube et al., "Integrated interferometric injection laser: Novel fast and broad-band tunable monolithic light source," IEEE J. Quantum Electron., vol. 27, pp. 1616–1624, 1991.

[9] G. P. Li, T. Makino, and C. M. Wu, "Multi-lambda ridge waveguide gain-coupled DFB laser array," J. Lightwave Technol., vol. 13, pp. 196–199, 1995.

[10] I. Ogura, K. Kurihara, S. Kawai, M. Kajita et al., "A multiple wavelength vertical-cavity surface-emitting laser (VCSEL) array for optical interconnection," IEICE Trans. on Elect., vol. E78-C, no. 1, pp. 22–27, 1995.

Optically Controlled Serially Fed Phased-Array Transmitter

Yian Chang, Boris Tsap, Harold R. Fetterman, *Fellow, IEEE,*
David A. Cohen, A. F. J. Levi, and Irwin L. Newberg, *Member, IEEE*

Abstract— A new optically controlled phased-array system has been developed that has all the advantages of true time delay (TTD), yet only requires one tunable laser, one optical modulator, and one fiber-optic grating unit. In this letter, a two-element serial-feed transmitter has been assembled and tested to demonstrate the feasibility of this novel concept. Experimental results include TTD operation from 6–12 GHz using both 10- and 1-ns pulses transmitted to five different directions.

Index Terms—Optical control, phased array, serial feed, true time delay.

I. INTRODUCTION

WE HAVE developed a new optically controlled system, suitable for phased array radar, microwave imaging, directional data communication, and related applications [1], [2]. This system uses a serial-feed concept that represents a departure from the conventional approach to these applications. Our concept yields a major simplification in both optical and microwave components. Unlike many of the parallel systems [3]–[8] currently under investigation, our system requires a single wavelength tunable laser, modulator, and time delay element [9] to provide the necessary phase and true time delays. In our design the use of fiber-optic techniques, such as long and low-loss delay lines, is intrinsic to operation of the system. Precise timing control is used to distribute RF pulses with phase and time delay information to each element in an operating antenna array. In this letter we report a demonstration of this concept using a two-element transmitter with five pointing directions. We also exhibit true time delay (TTD) operation from 6–12 GHz.

II. SERIAL-FEED CONFIGURATION

The transmit function can be described in terms of a serial timing unit and a serial to parallel distribution network as shown in Fig. 1. The desired delays for a given RF beam direction are generated sequentially by the timing unit and then transformed into parallel signals by the distribution network.

Y. Chang, B. Tsap, and H. R. Fetterman are with the Department of Electrical Engineering, University of California, Los Angeles, CA 90095 USA.
D. A. Cohen and A. F. J. Levi are with the Department of Electrical Engineering, University of Southern California, Los Angeles, CA 90089-1111 USA.
I. L. Newberg is with Hughes Aircraft Co., Los Angeles, CA 90009-2426 USA.
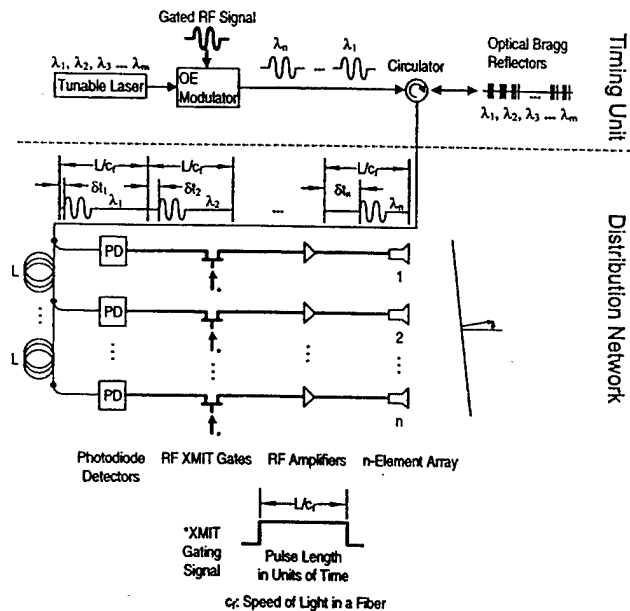
Fig. 1. Basic serial-feed transmit mode implementation for array of n elements. An optical Bragg grating unit in conjunction with a tunable laser provides steering delays.

This network then feeds the parallel delays to the antenna arrays.

In our design, the timing portion uses an electrically tuned DBR laser [10], [11]. The laser light output is both amplitude modulated at the desired microwave frequencies and gated at the RF transmission signal pulse length using an optical modulator. After passing through the modulator, the laser light is directed through an optical circulator to a series of fiber-optic Bragg reflectors. The incident optical wavelength determines the position in the fiber at which light is reflected back. Thus, a wavelength-selective delay can be imposed onto each RF modulated optical pulse. In the basic system discussed here, each serially fed optical pulse has a unique wavelength and therefore a unique time delay relative to the gating signal. The desired pointing direction determines which wavelengths should be chosen. The number of pulses in the fully loaded tapped delay line corresponds to the number of radiating elements in the antenna array or subarray. Specifically, the first pulse is intended for the nth element and the nth pulse is intended for the first element. The RF amplitude and phase of each element can be controlled independently, thus allowing multibeam patterns to be formed using the same hardware configuration.

Returned light from the third port of the circulator enters the distribution network formed by the tapped delay line. It is important to note that this tapped line is used to transform serial signals into parallel ones and does not generate the delays for beam steering. Once the series of optical pulses arrive at the correct delay line taps for each antenna element, the microwave modulation is extracted using photodetectors. When the tapped delay line is fully loaded, the microwave signals from these detectors are simultaneously gated on with microwave switches (Xmit gates). Each element's microwave pulse has the correct time delay set by the timing unit to form a radiating beam in the desired direction. After the signal is radiated the switches are turned off and the line is reloaded. The number of radiating directions is limited only by the number of available laser wavelengths and Bragg reflectors. Although our initial efforts used a two laser switched system and a fiber grating unit with discrete wavelength selectivity, the system will ultimately use a tunable DBR laser with a linearly chirped grating to provide continuous scanning.
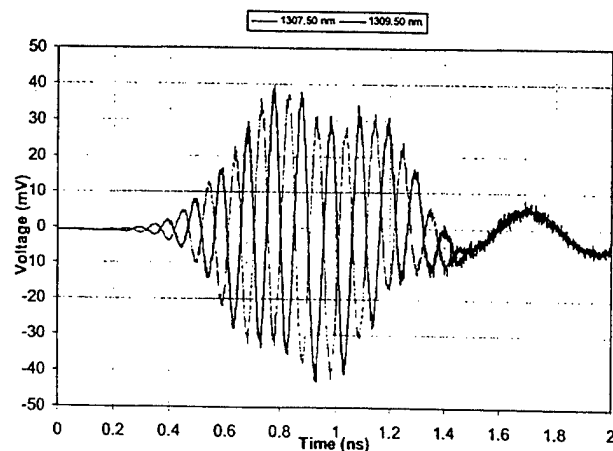

Fig. 2. Ten-GHz 1-ns pulses carried by 1307.50- and 1309.50-nm optical carriers monitored on the CH1 of the DSO. The 1307.50-nm pulse leads the 1309.50-nm pulse by 40 ps.

III. EXPERIMENT

To establish the viability of this serial-feed approach, we have assembled a two-element transmitter with five optical wavelengths yielding five discrete pointing directions. One external cavity tunable laser (wavelength $= \lambda_t$) and one fixed wavelength laser (wavelength $= \lambda_f$) are used in conjunction with two optical modulators to generate the desired wavelengths. By alternately pulse gating and RF modulating the CW λ_t and λ_f signals, a fast tunable laser switching between two wavelengths (λ_t and λ_f) is effectively simulated. In our initial experiments the repetition rate of wavelength switching was 25 MHz, corresponding to the tapped fiber delay length $L \approx 4$ m. The five values of λ_t varied from 1307.50 nm through 1311.50 nm, with a 1-nm separation between wavelengths, and λ_f was set at 1309.50 nm. These wavelengths were selected based on the Bragg wavelengths of the fiber reflectors. The relative time delays between the λ_t pulses and the λ_f pulse were measured to be -40 ps, -20 ps, 0 ps, 20 ps, and 40 ps, with an uncertainty of ± 2 ps.

The time-delayed RF signals feeding the two-element antenna array were monitored on a digital sampling oscilloscope's (DSO's) channel 1 and 2 (CH1 and 2). By correctly gating the RF signals exiting the photodetectors, CH1 received the λ_t pulse (variable delay) and CH2 received the λ_f pulse (delay reference). Two representative pulse widths have been tested: 10 and 1 ns. The 10-ns pulses offer a flat middle portion suitable for time-delay measurements using our DSO with best-fit sine functions. The time delays measured using the two channels of the DSO agree with the designed grating delays at RF frequencies from 6–12 GHz. The 1-ns pulses, with a 10-GHz center frequency, contained frequency components from 8–12 GHz and were suitable for demonstrating the wide instantaneous bandwidth of the system. Fig. 2 shows 10-GHz, 1-ns pulses, with two of the five possible time delays.

Because this experimental transmitter only has two elements, its radiating beam width is very broad ($\sim 60°$). Therefore, in order to demonstrate squint-free operation with ac-
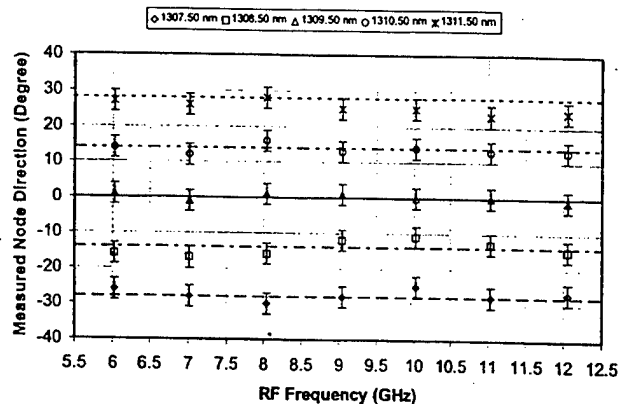
Fig. 3. Measured node direction versus RF frequency at different λ_t with λ_f fixed. The straight lines show the theoretical values. This shows the TTD nature of the system.

ceptable resolution, the radiation node was used instead of the antinode. The two optical modulators were biased at different modulation slopes to provide an extra π phase shift between the two elements. The radiation node direction was measured by moving the receiving horn to minimize the detected signal, while maintaining the same distance from the two-element array. Using an antenna separation of 2.54 cm, the theoretical node directions are $-28°, -14°, 0°, 14°$, and $28°$. Fig. 3 shows the measured node direction versus RF frequency at different optical wavelengths using 10-ns-long pulses. It shows good agreement with the anticipated pointing directions and effectively illustrates squint-free operation with some fluctuations. The observed deviations are attributed to the fact that only two elements were used in this transmitter. This resulted in a large uncertainty in locating the minimum of the received signal. By using more antenna elements, direct measurements on the antinode directions will provide exceptional resolution with suppressed fluctuations.

To demonstrate the wide instantaneous bandwidth of the transmitter, 10-GHz, 1-ns pulses with 25-MHz system repetition rate were radiated. The radiation node directions were measured to be the same as those in Fig. 3. The spectra of the
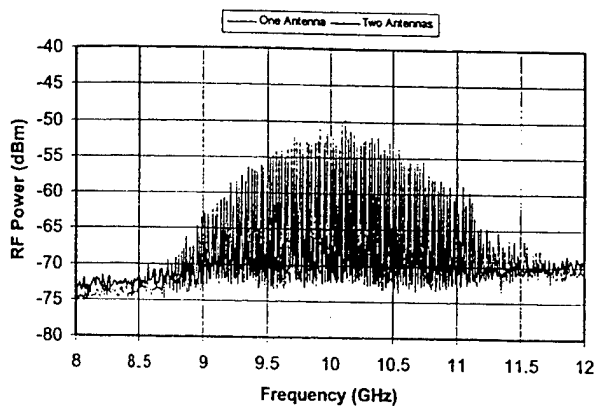
Fig. 4. The spectra of the detected 1-ns pulses centered at 10 GHz. The fine structure was caused by the system repetition rate of 25 MHz. The receiving horn was located at the node ($-28°$). The gray curve is the signal from only one antenna. The black curve shows that the signals from the two antennas cancel each other as expected for a node.

received signals at a node are shown in Fig. 4. The black curve was obtained when both antennas were radiating. Because of the TTD in our system, the node position is independent of frequency. The power spectrum of the node is shown to be minimized over the bandwidth defined by the pulse (8–12 GHz). To further demonstrate the two antenna signals indeed cancel out, one antenna was disconnected from the system and the spectrum of the other antenna measured. The result is shown as the gray curve in Fig. 4.

IV. CONCLUSION

A new serially fed true time delay transmit system has been presented and the basic concept has been experimentally verified. It uses only one tunable laser, one optical modulator and one delay element to achieve beam steering thereby greatly simplifying and increasing the flexibility of optically controlled systems. For large two-dimensional arrays ($>10^3$ elements), the problem of obtaining sufficient delays can be solved by cascading two timing units: one for horizontal control and one for vertical control. In such a system, consisting of two lasers, optical modulators, and delay elements, the RF modulated optical output of the vertical timing unit is detected and then fed to the RF input of the optical modulator of the horizontal timing unit. The number of delays obtainable

from this configuration will go as the square of the number of wavelengths obtainable from each laser. Furthermore, a natural extension of this technology can be used both for the receive mode and for passive imaging [1].

The two-element, five-delay transmit system we have presented is a basic unit that demonstrates the concept of a serial-feed. It is possible to enhance this system in several ways and to extend it to multiple frequencies and beams. Finally, this system represents a major departure from traditional parallel connected configurations. Because of its simplicity, we foresee its implementation in many new application areas.

ACKNOWLEDGMENT

REFERENCES

[1] D. A. Cohen, Y. Chang, A. F. J. Levi, H. R. Fetterman, and I. L. Newberg, "Optically controlled serially fed phased array sensor," *IEEE Photon. Technol. Lett.*, vol. 8, no. 12, pp. 1683–1685, 1996.
[2] D. A. Cohen, Y. Chang, A. F. J. Levi, H. R. Fetterman, and I. L. Newberg, "Video broadcast using an optically-controlled serially-fed phased-array antenna," to be published.
[3] D. Dolfi *et al.*, "Photonics for phased array radars," *Proc. SPIE*, vol. 2560, pp. 158–165, 1995.
[4] H. R. Fetterman *et al.*, "Optically controlled phased array radar receiver using SLM switched real time delays," *IEEE Microwave Guided Wave Lett.*, vol. 5, no. 11, pp. 414–416, 1995.
[5] L. Xu, R. Taylor, and S. R. Forrest, "True time-delay phased-array antenna feed system based on optical heterodyne techniques," *IEEE Photon. Technol. Lett.*, vol. 8, no. 1, pp. 160–162, 1996.
[6] R. D. Esman *et al.*, "Fiber-optic prism true time-delay antenna feed," *IEEE Photon. Technol. Lett.*, vol. 5, no. 11, pp. 1347–1349, 1993.
[7] L. J. Lembo, T. Holcomb, M. Wickham, P. Wisseman, and J. C. Brock, "Low-loss fiber optic time-delay element for phased-array antennas," *Proc. SPIE*, vol. 2155, pp. 13–23, 1994.
[8] A. Molony, C. Edge, and I. Bennion, "Fiber grating time delay element for phased array antennas," *Electron. Lett.*, vol. 31, no. 17, pp. 1485–1486, 1995.
[9] G. A. Ball, W. H. Glenn, and W. W. Morey, "Programmable fiber optic delay line," *IEEE Photon. Technol. Lett.*, vol. 6, no. 6, pp. 741–743, 1994.
[10] M. Schilling *et al.*, "Integrated interferometric injection laser: Novel fast and broad-band tunable monolithic light source," *IEEE J. Quantum Electron.*, vol. 27, no. 6, pp. 1616–1624, 1991.
[11] M. Öberg *et al.*, "Complete single mode wavelength coverage over 40 nm with a super structure grating DBR laser," *J. Lightwave Technol.*, vol. 13, no. 10, pp. 1892–1898, 1995.

Phased-Array Optically Controlled Receiver Using a Serial Feed

Boris Tsap, Yian Chang, Harold R. Fetterman, *Fellow, IEEE*, A. F. J. Levi,
David A. Cohen, and Irwin Newberg, *Member, IEEE*

Abstract—Extension of a new optically controlled serially fed phased-array system to the receive mode of operation has been demonstrated. Our system uses the pulsed nature of microwave radars in a manner similar to clocked systems used in digital configurations. This novel approach requires only the use of one tunable laser, one optical modulator, and one chirped fiber grating unit. In this letter, we present an experimental demonstration of a two-element serially fed wide frequency range receiver that validates the feasibility of this novel concept. Our system can be readily expanded with multiple elements and transmit/receive modules for a complete phased array system.

Index Terms—Directional communications, fiber gratings, optical control, optical fiber delay line, phased-array radar.

I. INTRODUCTION

WE HAVE recently reported the development of a novel optically controlled phase array transmit configuration, suitable for numerous applications, including phased array radar and directional data communications [1]–[3]. The serial-feed concept used in these systems represented a departure from conventional parallel-feed approaches, which are very laser intensive [4]–[14]. Our system's use of a single wavelength tunable laser, one modulator, and one fiber grating time delay element provided a major simplification in the number of required optical components. In this letter, we report the demonstration of the receive portion of this concept using a two-element receiver with observation directions ranging from +30° to −30°. The dependence on one time delay unit to provide time/phase shifts for all of the antenna elements distinguishes this serially-fed system from previously implemented receive systems [13], [15]. Our introduction of a chirped fiber grating to the system enhances its capability by making its directional operation continuously variable. Combined with our transmit capability [1], and with the use of a T/R switch, this new design can now be extended to a complete transmit/receive radar system.
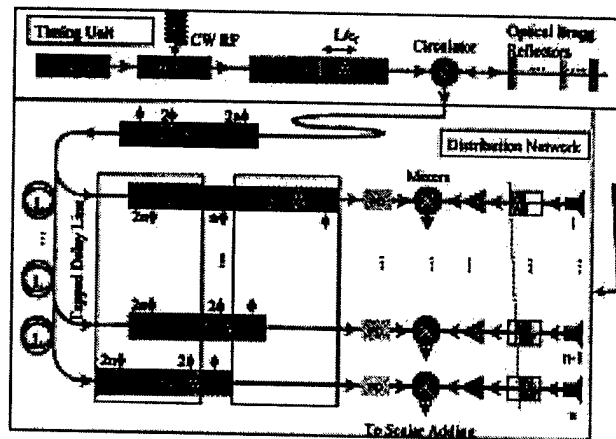
Fig. 1. Basic serially fed receive mode configuration for an array of n elements. A chirped fiber grating in conjunction with a tunable laser provides the necessary phased delays for virtually continuous directional operation. A second tapped delay line in parallel can be added to achieve almost continuous temporal operation.

II. SERIALLY FED RECEIVER CONFIGURATION

The serially fed receiver consists of a timing unit and a serial to parallel conversion distribution network as shown in Fig. 1. The timing unit sequentially generates delays designated for a given direction of observation. The distribution network then transforms these delays into parallel signals and feeds them to the antenna elements.

In the basic receive configuration (Fig. 1), the train of (L/c_f)-long laser light pulses, where L is the tapped fiber delay length and c_f is speed of light in fiber, is modulated at the desired microwave frequency, and directed through an optical circulator to a fiber grating. By reflecting from a particular point on the fiber grating a wavelength-selected phase shift is imposed onto each modulated optical pulse. The returned light from the third port of the circulator enters the distribution network which supplies each mixer with the local oscillator (LO) signal for mixing with the received microwave signal. Assume that the tapped delay line is loaded sequentially with $2n$ pulses from a tunable laser each carrying the LO signals that are phase shifted by $\phi, 2\phi, \cdots, 2n\phi$, respectively, to the mixers. The tunable laser must switch wavelengths on the order of a ns and therefore has little effect on typical radar signals which have durations of hundreds, and even thousands, of nanoseconds. At the beginning of the receive mode of operation, the first pulse supplies the last mixer and the nth pulse supplies the first mixer. After an interval L/c_f in
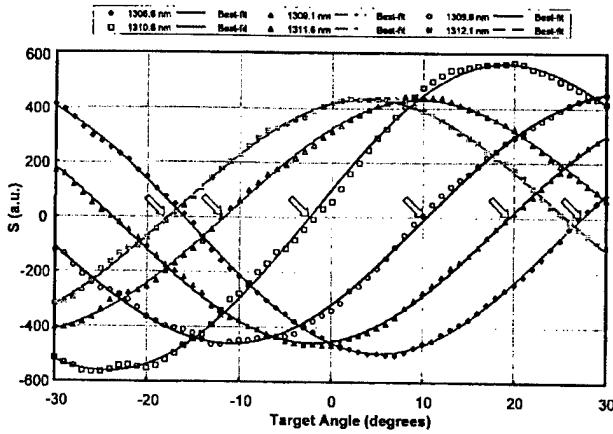
Fig. 2. Target scanning with the receiver pointed to six different "listening" directions, defined by the tunable laser wavelength λ_t. In this demonstration, experimentally determined "listening" directions correspond to the angles where $S = 0$ and $S' > 0$.

time, the second pulse will reach the nth mixer and become its LO signal carrier. At the same time, the $(n + 1)$th pulse will be supplying the first mixer and the cycle continued. Note that the receiver continues to "listen" in the same direction after each wavelength progression because only the relative phases between mixers (differential phase ϕ) are important. This wavelength progression repeats until the last loaded pulse reaches the first mixer.

At this point, there would be a loss of duty cycle for the simplest configuration while the line is reloaded. However, in order to achieve almost continuous operation, our design can incorporate the option of a second tapped delay line with an extra nL delay length which can be switched to feed each mixer the appropriate phase. Although, as in our initial transmit experiment a two-laser switch system was used, we have utilized a linearly chirped grating, which along with a tunable DBR laser will provide almost continuous scanning for the ultimate system.

III. EXPERIMENT

In an experimental demonstration with a two-element array, we used two external cavity wavelength tunable lasers in conjunction with two optical modulators to simulate a single fast tunable laser. The wavelength of the first laser was fixed at λ_f and the wavelength λ_t of the second laser was tuned to different values to control the "listening" direction of the receiver. A continuously chirped fiber grating centered at 1310 nm with a 10-nm bandwidth (>97% reflectivity) was used as the wavelength sensitive element. Phase delayed signals corresponding to the reflections of λ_f and λ_t were generated by the basic true time delay (TTD) timing unit used in the transmit configuration and, therefore, yielded squint-free operation. An RF signal was simultaneously fed to a transmitting horn placed on a rotating stage to simulate the signal returned from a target. The RF signal picked up by each of the receiving antenna elements was fed to the RF port of a mixer. The LO input of the mixer at each element was provided with the phase delayed signal from the timing unit and photodiode. Because the target distance was

considered unknown, quadrature mixers were used to provide homodyne IF signals in two quadrants. The two outputs of the mixer associated with the first antenna element contain dc components given by

$$V_{\sin}^{\mathrm{I}} = A_{\mathrm{I}} B_{\mathrm{I}} \sin(\phi - \Phi_1) \quad V_{\cos}^{\mathrm{I}} = A_{\mathrm{I}} B_{\mathrm{I}} \cos(\phi - \Phi_1).$$

For the outputs of the mixer associated with the second antenna element, we have

$$V_{\sin}^{\mathrm{II}} = A_{\mathrm{II}} B_{\mathrm{II}} \sin(\Delta - \Phi_1) \quad V_{\cos}^{\mathrm{II}} = A_{\mathrm{II}} B_{\mathrm{II}} \cos(\Delta - \Phi_1)$$

where A_{I} and A_{II} are proportional to the LO amplitudes sent to the mixers, B_{I} and B_{II} are proportional to the received RF amplitudes, Φ_1 is an unknown phase in the received RF signals due to the unknown target distance, ϕ is the phase difference between the LO signals (from the timing unit), $\Delta = (d\omega \sin\theta)/c$ is the phase difference between the received RF signals due to the different path lengths from the target, θ is the target angle, and d is the spacing between the antenna elements. The four outputs of the mixers were fed to a computer for processing. The computer calculated the final result in the form

$$S = V_{\cos}^{\mathrm{I}} \cdot V_{\sin}^{\mathrm{II}} - V_{\sin}^{\mathrm{I}} \cdot V_{\cos}^{\mathrm{II}} = A_{\mathrm{I}} A_{\mathrm{II}} B_{\mathrm{I}} B_{\mathrm{II}} (\Delta - \phi). \quad (1)$$

The phase difference between the LO signals is set in the timing unit by the fiber grating for each wavelength pair $\lambda_f - \lambda_t$ and is described by

$$\phi = k(\lambda_t - \lambda_f)\omega$$

where k is a parameter involving the chirp of the fiber grating. For a given target direction, θ can be extracted by plotting $S[\phi(\lambda_t)]$ for different λ_t. The calculated function S in (1) is zeroed, with a positive slope, when $(d\sin\theta)/c = k(\lambda_t - \lambda_f)$. Therefore, the target angle can be written as

$$\theta = \sin^{-1}[ck(\lambda_t - \lambda_f)/d]. \quad (2)$$

In this feasibility demonstration, the receiver had only two elements and to increase the resolution of the system, we had chosen to use the function S in (1) to determine the target angle because of its sensitivity near $(d\sin\theta)/c = k(\lambda_t - \lambda_f)$.

To demonstrate the ability of the system as a phased array radar receiver, we chose six different wavelength pairs to deliver the LO signals; effectively, the receiver was used to "listen" to six different directions. For a selected direction (wavelength pair), the target angle was changed from $-30°$ to $30°$ with a step size of $1°$. As shown above at the right "listening" direction the S function is zero with a positive slope. In these experiments, the RF frequency was set to 8 GHz, λ_f was kept at 1310.6 nm and λ_t was tuned to six different wavelengths. Fig. 2 shows the corresponding S function versus the target angle for each wavelength pair. The least square best-fit functions were calculated and used to determine the target directions with higher accuracy. The measured target angles (corresponding to the angles where $S = 0$ and $S' > 0$ in Fig. 2) are $-17.7°$, $-11.6°$, $-2.4°$, $10.4°$, $19.4°$, and $27.4°$. The theoretically calculated six "listening" directions, using (2), are $-19.3°$, $-12.8°$, $0°$, $12.8°$, $19.3°$, and $26.2°$. The measured values are well within the expected $3°$ of the two antenna element theoretical values.